National Technical University of Athens
School of Mechanical Engineering
Fluids Department
Parallel CFD & Optimization Unit

Eddy Viscosity Adaptation Using the Continuous Adjoint Method with Application in Aerodynamic Shape Optimization

Diploma Thesis

Charalampos Tsolakos

Supervisor: Kyriakos C. Giannakoglou, Professor NTUA

Industrial Supervisor: Antoine Delacroix, Manager TME

Athens, 2026

Acknowledgements

I would like to begin by thanking my professor, Kyriakos C. Giannakoglou, for giving me the opportunity to work on an exciting research topic. His constant guidance and support have been essential to completing this thesis.

I would like to thank Antoine Delacroix, my manager at TME, for the trust he placed in me by giving me the opportunity to work with his team and contribute to such an engaging project. I am also deeply grateful to George Smyrlis, my mentor and colleague, for his constant support and guidance throughout my time there. I would also like to thank Maria Isabel da Silva and Andre Pinto, my colleagues, for their willingness to assist me and share their expertise whenever I needed it.

Lastly, I would like to express my heartfelt gratitude to all the members of TME with whom I had the privilege to collaborate during my internship. Their guidance played a crucial role in my personal and professional growth, allowing me to see how the knowledge I gained during my studies is applied in a real world industry setting.

I would like to thank all members of the Parallel CFD Optimization Unit for their support and collaboration. I am especially grateful to Dr. Nikolaos Galanos for his time, continuous support, and valuable guidance, as well as to Dr. Evangelos Papoutsis-Kiachagias for his constant advice whenever needed.

Θα ήθελα να εκφράσω τη βαθιά μου ευγνωμοσύνη στους ανθρώπους μου για τη στήριξη και την αγάπη τους όλα αυτά τα χρόνια. Θέλω να ευχαριστήσω ιδιαίτερα τους υπέροχους γονείς μου, τον μικρό μου αδελφό και τη Δέσποινα (τον άνθρωπο της ζωής μου), όλοι τους ήταν πάντα δίπλα μου, όχι μόνο κατά τη διάρκεια των σπουδών μου, αλλά και σε κάθε δυσκολία που αντιμετώπισα. Επίσης, θα ήθελα να ευχαριστήσω τους παιδικούς όσο και όλους τους φίλους που είχα την τύχη να γνωρίσω κατά τη διάρκεια των σπουδών μου, για τις όμορφες στιγμές και τις αναμνήσεις που μοιραστήκαμε, και ιδιαίτερα τον Γιάννη για τη συνεχή βοήθειά του. Τέλος, θα ήθελα να ευχαριστήσω τον παππού και τη γιαγιά μου, που μου έμαθαν να ονειρεύομαι και να κυνηγάω τα όνειρά μου.

National Technical University of Athens
School of Mechanical Engineering
Fluids Department
Parallel CFD & Optimization Unit

Eddy Viscosity Adaptation Using the Continuous Adjoint Method with Application in Aerodynamic Shape Optimization

Diploma Thesis
Charalampos Tsolakos
Academic Supervisor: Kyriakos C. Giannakoglou, Professor NTUA
Industrial Supervisor: Antoine Delacroix, Manager TME
Athens, February 2026

Abstract

This diploma thesis focuses on the implementation and development of an adjoint–based flow solver within the OpenFOAM environment, employing a data–driven approach for turbulence closure, as well as on investigating how this method can be exploited in aerodynamic shape optimization. First, a comparison is made between the RANS and DES models, both based on Spalart–Allmaras (SA) model, aiming to enhance the predictive accuracy of a steady simulation by using the latter as higher fidelity reference data which comes with a significantly higher computational cost (unsteady run). The proposed method and the developed software tools are applied to three cases: a U–Bend duct, the NACA0012 airfoil, and the geometry of the passenger vehicle Toyota Aygo X.

A surrogate to the RANS (SA) turbulence model is created by minimizing the deviation between the velocity field produced by the model and time-averaged DES results. The turbulent viscosity field ν_t constitutes the optimization variables. This is why this method will be referred to as "Eddy–Viscosity Adaptation" or EVA. For this minimization problem, an adjoint problem is formulated and solved, in OpenFOAM. The correctness of the adjoint derivatives is verified through comparisons with finite differences.

The surrogate turbulent eddy viscosity fields are subsequently utilized in a shape optimization loop, with the goal of producing aerodynamic shapes with a lower drag coefficient, using parsimonious steady runs while maintaining DES-level accuracy. During the optimization, the eddy viscosity field computed a priori by the EVA step remains fixed; this is why, this optimization is referred to as a "Frozen Eddy Viscosity" or FEV one and the adjoint method used for this has accordingly been adapted. In this way, the work aims to replace the use of an unsteady flow simulation (and the corresponding unsteady adjoint) within the shape optimization loop, and get "similar" results at much lower computational cost.

A great part of this diploma thesis was carried out at the facilities of Toyota Motor Europe (TME) in Brussels, during a six month internship, under the supervision of Mr. Antoine Delacroix from the industry side.

Εθνικό Μετσόβιο Πολυτεχνείο
Σχολή Μηχανολόγων Μηχανικών
Τομέας Ρευστών
Μονάδα Παράλληλης Υπολογιστικής Ρευστοδυναμικής &
Βελτιστοποίησης

Προσαρμογή Τυρβώδους συνεκτικότητας με τη Συνεχή Συζυγή Μέθοδο με Εφαρμογή στην Αεροδυναμική Βελτιστοποίηση Μορφής

Διπλωματική Εργασία
Χαράλαμπος Τσολάκος
Ακαδημαϊκός Επιβλέπων: Κυριάκος Χ. Γιαννακόγλου, Καθηγητής ΕΜΠ
Βιομηχανικός Επιβλέπων: Antoine Delacroix, Manager TME
Αθήνα, Φεβρουάριος 2026

Περίληψη

Αντικείμενο της διπλωματικής εργασίας είναι η ανάπτυξη και εφαρμογή μιας συζυγούς μεθόδου στο περιβάλλον του OpenFOAM, για την υποκατάσταση μοντέλων τύρβης με τη χρήση δεδομένων, καθώς και η διερεύνηση του τρόπου με τον οποίο η μέθοδος αυτή μπορεί να αξιοποιηθεί στην αεροδυναμική βελτιστοποίηση μορφής. Αρχικά, πραγματοποιείται σύγκριση μεταξύ των μοντέλων RANS και DES, τα οποία βασίζονται και τα δύο στο μοντέλο Spalart–Allmaras (SA), όπου επιδιώκεται να βρεθεί ένα υποκατάστατο του πρώτου, χρησιμοποιώντας το δεύτερο ως αναφορά υψηλότερης πιστότητας, η οποία όμως έχει υψηλότερο υπολογιστικό κόστος. Η ανάλυση εφαρμόζεται σε τρία προβλήματα ροής σε/γύρω από: έναν αγωγό τύπου U, την αεροτομή NACA0012 και τη γεωμετρία του επιβατικού οχήματος Toyota Aygo X.

Δημιουργείται ενα υποκατάστατο του μοντέλου RANS (SA) μέσω ελαχιστοποίησης της απόκλισης μεταξύ του πεδίου ταχυτήτων που παράγει το μοντέλο και των χρονικά μέσων αποτελεσμάτων DES. Ως μεταβλητή βελτιστοποίησης επιλέγεται, σε κάθε κελί, το πεδίο της τυρβώδους συνεκτικότητας ν_t· για τον λόγον αυτό, η μέθοδος θα αναφέρεται ως Eddy–Viscosity Adaptation ή EVA. Για την επίλυση του προβλήματος ελαχιστοποίησης διατυπώνεται και επιλύεται ένα συζυγές πρόβλημα στο OpenFOAM. Η ορθότητα των συζυγών παραγώγων επαληθεύεται μέσω σύγκρισης με τη μέθοδο των πεπερασμένων διαφορών.

Τα υποκατάστατα πεδία τυρβώδους συνεκτικότητας χρησιμοποιούνται στη συνέχεια σε έναν βρόχο βελτιστοποίησης μορφής, με στόχο την παραγωγή αεροδυναμικών γεωμετριών με μειωμένο συντελεστή οπισθέλκουσας, διατηρώντας παράλληλα ακρίβεια επιπέδου DES, αν και η επίλυση γίνεται με χρονικά μόνιμο κώδικα, χωρίς καν το μοντέλο τύρβης. Κατά τη διάρκεια της βελτιστοποίησης, το πεδίο τυρβώδους συνεκτικότητας που υπολογίζεται στο στάδιο EVA παραμένει σταθερό· γι' αυτό η διαδικασία αναφέρεται ως Fixed Eddy Viscosity ή FEV και η αντίστοιχη συζυγής διατύπωση προσαρμόζεται αναλόγως. Με αυτόν τον τρόπο, η εργασία στοχεύει να αντικαταστήσει έναν βρόχο βελτιστοποίησης που βασίζεται

σε μη-μόνιμη προσομοίωση ροής (και στο αντίστοιχο μη-μόνιμο συζυγές πρόβλημα), επιτυγχάνοντας συγκρίσιμα αποτελέσματα με σημαντικά μικρότερο υπολογιστικό κόστος.

Το μεγαλύτερο μέρος της διπλωματικής εργασίας πραγματοποιήθηκε στις εγκαταστάσεις της Toyota Motor Europe (TME) στις Βρυξέλλες, κατά τη διάρκεια εξάμηνης πρακτικής άσκησης, υπό την επίβλεψη του κ. Antoine Delacroix από την πλευρά της βιομηχανίας.

Acronyms

ATC	Adjoint Transpose Convection
CFD	Computational Fluid Dynamics
DDES	Delayed Detached Eddy Simulation
DES	Detached Eddy Simulation
DSR	Deep Symbolic Regression
EVA	Eddy Turbulence Viscosity
FEV	Frozen Eddy Viscosity
IDDES	Improved Delayed Detached Eddy Simulation
MOO	Multi Objective Optimization
NN	Neural Network
NTUA	National Technical University of Athens
OpenFOAM	Open Field Operation And Manipulation
PCOpt	Parallel CFD & Optimization Unit of NTUA
PDE	Partial Differential Equation
RANS	Reynolds Averaged Navier Stokes
SA	Spalart–Allmaras
ShpO	Shape Optimization
SOO	Single Objective Optimization
TMA	Turbulence Model Adaptation
TME	Toyota Motor Europe
WLTP	Worldwide Harmonized Vehicle Test Procedure
WT	Wind Tunnel

Contents

Chapter 1

Introduction

1.1 Industrial Motivation and Regulatory Framework

Over recent decades, against the backdrop of climate change, increasingly stringent measures have been introduced to limit carbon dioxide emissions, with a decisive impact on industry and, in particular, the automotive sector. The steady rise of electric and hybrid vehicles confirms that the market is now shifting toward low or zero emission solutions, while, at the same time, the European Union has established a framework of restrictions on fuel consumption and CO_2 emissions, accelerating this transition and placing pressure on manufacturers to deliver measurable reductions in the environmental footprint of their vehicles [1].

Since vehicle design is directly linked both to CO_2 emissions and to driving range (especially in electric vehicles), reliable prediction of aerodynamic performance becomes essential. Experimental testing remains the most reliable means of validation, but it is particularly time consuming and costly. In this context, the WLTP (Worldwide Harmonized Light Vehicle Testing Procedure) has contributed to a stricter and more complex evaluation process, as it aims to reflect fuel consumption and emissions in everyday use more realistically. Consequently, the development of a new model requires systematic assessment of multiple variants so that its performance can be documented with confidence. For this reason, CFD simulations have taken on a central role in the design process and, when it can be demonstrated that they fall within a specific accuracy range, they can be used as a reliable evaluation tool and to support the certification process, within the framework of standards such as WLTP [2, 3].

Achieving the level of accuracy dictated by modern regulations translates into increased computational demands, adding to both development time and resources. In this context, product design remains, in essence, an iterative process, where successive alternatives are examined with the aim of optimizing both aesthetic features and the targets set by engineers in terms of strength and performance. Although numerical simulations have advanced significantly in recent years, there remains a strong need for methods that combine lower computational cost with more reliable predictions. This work aims to study and develop a turbulence model adaptation methodology, with the goal of bridging the gap between computational cost and accuracy, providing results that meet industrial requirements.

1.2 Impact of Turbulence Model on CFD Predictions

The accuracy of CFD simulation results depends strongly on the choice of turbulence model, the set of equations used to approximate the effect of turbulence on the flow. Since turbulence is inherently complex and chaotic, different modeling assumptions lead to different levels of fidelity in the predicted flow field and, consequently, in the resulting quantities of interest. The influence of the turbulence model in a simulation is highlighted in Fig. 1.1, which shows the flow around a sphere and highlights how the predicted wake and turbulent structures vary across turbulence modeling approaches.

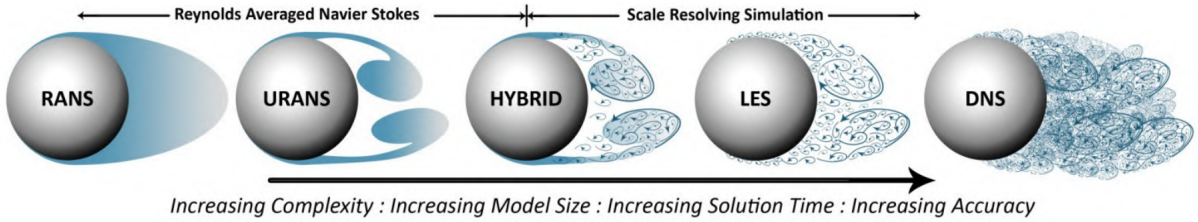

Figure 1.1: Representative wake structures behind a sphere, as predicted by the different turbulence models, from [4].

At the same time, higher fidelity is usually accompanied by increased demands in computational time and memory, which in some cases may differ even by orders of magnitude, creating practical constraints at development stages where many iterative evaluations are required.

Therefore, it is clear that model selection can lead from minor deviations to, in some cases, a fundamentally different picture of the flow, particularly in mildly unsteady regimes.r. Different models may predict the onset of separation differently, as well as the size or intensity of the recirculation region. These differences are reflected on critical performance metrics, such as drag, which is targeted for reduction both for efficiency reasons and for compliance with applicable standards and limits. Consequently, the feedback that engineers and designers receive from simulations depends directly on the assumptions of the selected model, and conclusions must be interpreted within this context.

This model dependence also has direct implications for computationally driven design processes, such as shape optimization (ShpO). Most optimization tools are built around cheaper steady-state approaches, which do not always capture critical flow phenomena with sufficient accuracy. As a result, the evaluation and optimization of a geometry may lead to new shapes that appear improved at that specific modelling level, but do not exhibit the expected improvement when assessed with more reliable methods or through experimental validation.

Therefore, the improvement of how turbulence models are used is becoming increasingly urgent. It is clear how valuable such progress would be at both the research and industrial level, as it would enable more reliable predictions at lower computational cost. In this way, simulation times are reduced and the development cycle is accelerated, saving both time and resources.

1.3 Turbulence Model Adaptation–Literature Survey

A straightforward direction for improving turbulence models has historically been to increase their complexity for example, by using multi-equation models, enriched transport terms. Although this approach can incorporate more physics, it is often accompanied by the introduction of additional free parameters and empirical constants, which require re-testing and tuning depending on the problem at hand. At the same time, increased complexity also raises computational cost, since additional equations must be solved. Nevertheless, greater complexity does not guarantee an equally consistent and predictable increase in accuracy, as a model may perform satisfactorily in some flows while exhibiting significant deviations in others.

Within this context, data-driven approaches have emerged as a particularly promising complementary strategy. In an industrial setting, where high-fidelity data from years of development (e.g., LES/DES simulations or experimental measurements) are often available, there is an opportunity to leverage this accumulated information for the systematic improvement of existing models. Of particular interest are approaches that attempt to identify and correct deficiencies in its functional form. In other words, the goal is to reveal where and how the baseline model deviates from the underlying flow physics, in order to achieve **Turbulence Model Adaptation (TMA)**.

One of the most characteristic methodologies for TMA is the approach often referred to as Field Inversion in the literature [5, 6, 7, 8, 9]. This methodology was initially introduced by Duraisamy and his colleagues [6], and the core idea is a method using an adjoint-based approach for turbulence closure, leveraging a data-driven technique. Specifically, [6] demonstrated this methodology on two distinct test cases, employing both the SA and k–ω turbulence models. In the SA framework, they introduced a corrective factor $\alpha(\mathbf{x}, t)$ was introduced in the destruction term, leading to the modified transport equation:

$$\frac{D\widetilde{\nu}}{Dt} = P(\widetilde{\nu}) - \alpha(\mathbf{x}, t)\, D(\widetilde{\nu}) + T(\widetilde{\nu}). \tag{1.1}$$

The aim of TMA is to identify $\alpha(\mathbf{x}, t)$ at every mesh cell so that the discrepancy in skin friction between high-fidelity LES data and the corresponding RANS prediction be minimized. This is expressed through the objective function:

$$J(\alpha) = \int w \left[\tau_w^{\text{data}}(s) - \tau_w^{\text{model}}(s)\right]^2 \mathrm{d}s, \tag{1.2}$$

where the values of $\alpha(\mathbf{x}, t)$ in each mesh cell act as the design variables of the optimization problem. The optimal correction field is obtained as:

$$\alpha_{\text{opt}} = \arg\min_{\alpha} J(\alpha). \tag{1.3}$$

A second representative formulation introduces a corrective coefficient $\beta(\mathbf{x})$ in the destruction term of the ω equation within the k–ω model [8]. The modified governing

system of equations is written as:

$$\frac{\partial(\rho k)}{\partial t} + \frac{\partial(\rho u_j k)}{\partial x_j} = P - \beta^* \rho \omega k + \frac{\partial}{\partial x_j}\left[(\mu + \sigma_k \mu_t)\frac{\partial k}{\partial x_j}\right], \tag{1.4}$$

$$\frac{\partial(\rho \omega)}{\partial t} + \frac{\partial(\rho u_j \omega)}{\partial x_j} = \gamma \frac{\nu_t}{k} P - \beta(\mathbf{x})\,\theta\,\rho\omega^2 + \frac{\partial}{\partial x_j}\left[(\mu + \sigma_\omega \mu_t)\frac{\partial \omega}{\partial x_j}\right] + 2(1 - F_1)\rho\frac{\sigma_{\omega 2}}{\omega}\frac{\partial k}{\partial x_j}\frac{\partial \omega}{\partial x_j}. \tag{1.5}$$

In this setting, the goal is to determine the spatial distribution $\beta(\mathbf{x})$ that makes the RANS solution match high-fidelity LES data as closely as possible. A common definition of the objective function is:

$$\min_{\beta} J = \lambda_{\text{obs}} \sum_i \left(\widehat{d}_i - d_i(\beta)\right)^2 + \lambda_{\text{prior}} \sum_j (\beta_j - 1)^2 . \tag{1.6}$$

The last term in this equation prevents β from drifting too far from its baseline value $\beta = 1$. This discourages extreme or noisy corrections and helps keep the inferred field smooth and physically plausible as a turbulence model modification.

More recently, extensions of TMA have moved beyond applying a single corrective coefficient to a specific term and ,instead, target the direct inference of the turbulent viscosity field ν_t [7]. This formulation has two key advantages. First, by treating ν_t itself as the unknown to be inferred, the approach can bypass the explicit solution of the turbulence transport equation and its associated adjoint, which can substantially reduce the overall computational overhead of the inversion workflow. Second, it avoids the inherent ambiguity of where to correct within a given turbulence model. When a single factor is inserted in a selected term, it is not always clear whether that term is truly responsible for the model discrepancy, and alternative correction placements may require repeated reformulation and reimplementation of the adjoint system. By contrast, optimizing ν_t directly removes this dependency on a priori choices about which term to modify and provides a clear quantitative target the optimal turbulent viscosity distribution that best aligns the low-fidelity prediction with the reference data.

Once the adaptation process is completed, correction fields or enhanced ν_t fields can be obtained that closely match the target quantities defined earlier. There are several ways to make use of these fields, but the most commonly suggested approach in the literature involves linking local flow-field quantities to the optimal correction term identified through the adaptation process, in order to create a dataset. This dataset can then be used to train neural networks [10] or apply Deep Symbolic Regression (DSR) [11]. If the dataset includes sufficient information from multiple geometries, it can be used with the TMA process and appropriate training to create new or modified turbulence models. Such an approach could find significant applications in industries with access to a large number of high-fidelity simulation runs, where a dataset can be built using data from different geometries, such as various car models or the same geometry with different accessories. These models could be generalized, offering better accuracy while requiring much less computational time. In both cases, the optimal field produced by the TMA serves as a reference dataset, facilitating the development of new, more accurate turbulence models. The stages of this process can be illustrated in the flowchart shown in Fig. 1.2.

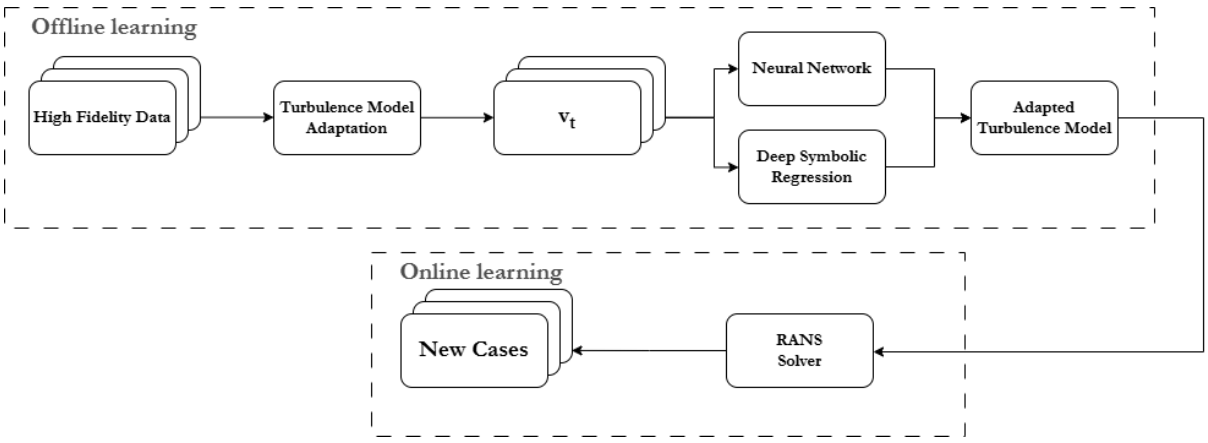

Figure 1.2: Turbulence model optimization process using adapted turbulence model and Neural Networks / Deep Symbolic Regression.

This thesis focuses on the development of an adjoint-based code for turbulence adaptation within the OpenFOAM computational tool, aiming to minimize the difference between two velocity fields: the RANS velocity field, which is the field to be improved, and the DES velocity field, which provides the data for the adaptation. This can be framed as an optimization problem, expressed by the following objective function:

$$J = \frac{1}{2} \int_{\Omega} \left(v_{RANS} - v_{DES} \right)^2 \, d\Omega$$

As optimization variables, the turbulence viscosity at each point in the domain will be used. This process, within the scope of this thesis, will be referred to as **Eddy Viscosity Adaptation (EVA)**.

1.4 Challenges of unsteady adjoint

This project, in addition to its current application, could also be extended to shape optimization (ShpO) problems. As highlighted in the thesis, RANS fields are often insufficient to accurately capture and describe the evolving flow, particularly in cases with unsteady flow, where unsteady flow solvers are necessary for a more precise representation. In such applications, steady-state adjoint solvers are not suitable, as they would optimize the geometry based on an incorrect field predicted by the RANS equations, and the new geometries would not necessarily yield improved solutions. To achieve accurate optimization, an unsteady adjoint solver must be employed, which introduces several challenges.

A major limitation of the unsteady adjoint is the rapid increase in computational cost. The order of magnitude difference between a simple RANS and DES simulation means that at each optimization cycle, both a primal and an adjoint problem need to be solved, each at a cost equivalent to running a DES simulation. In industrial cases, this can be prohibitive, as it may not be viable within the development and design stages of a product, where decision-making needs to be quick and immediate. Beyond the cost, the very nature of the

problem in DES makes the unsteady adjoint significantly more demanding than the steady RANS adjoint. Since the unsteady adjoint equations are integrated backward in time, the adjoint solver must have access to the instantaneous fields of the primal solution at every time step. This creates a practical dilemma: either the entire time history of the flow must be stored (with huge memory and disk requirements), or parts of the solution must be recomputed through checkpointing, which reduces memory requirements but introduces additional computational overhead and increases workflow complexity. In large 3D cases, data management alone can become a decisive limitation. At the same time, the hybrid nature of DES introduces additional difficulties in terms of mathematical smoothness and differentiability. DES models rely on switching mechanisms between RANS-like and LES-like behavior, which depend directly on the mesh. During ShpO, where the mesh changes even slightly, such non-smooth dependencies can produce discontinuities or strong sensitivity in the derivatives, complicating consistent linearization and, ultimately, the production of stable and repeatable gradients [12, 7].

Instead of using the unsteady adjoint, an alternative approach could be the use of the adapted ν_t fields, which are derived from the EVA process. Assuming that small changes in the geometry only affect the mean flow, this can be treated as applying a frozen eddy viscosity, without the need for an evolving turbulence model. The idea behind this approach is that high-fidelity information is introduced through the adapted fields, rather than by directly coupling DES to the gradient calculation. As a result, the optimization process can proceed without the need for a fully unsteady, DES-consistent adjoint formulation, thus avoiding the practical difficulties associated with unsteady adjoint optimization. This approach opens new possibilities for optimization and presents particular research interest, which will be explored in this thesis.

1.5 Thesis Outline

The aim of this diploma thesis is to investigate and develop a solver within the OpenFOAM environment that can be used to construct a surrogate turbulent viscosity through the continuous adjoint methodology. High-fidelity data, such as the simulation performed by the DES (SA) model, are then used as a reference for adapting the model through a EVA methodology, with the goal of improving its predictive capability. Finally, the adapted fields are incorporated into the Frozen Eddy Viscosity approach so that, through ShpO, geometries can be obtained that retain their improvement when evaluated with higher-fidelity models. In this way, the study seeks to approximate the benefit that would be expected from a fully unsteady adjoint approach, which in practice entails substantial technical and computational challenges.

- Chapter 2 presents the governing equations of incompressible flow, as well as the RANS and DES numerical approaches. In addition, the Spalart–Allmaras model and the near-wall treatment adopted in this work are described.
- Chapter 3 provides a comparison between RANS and DES within OpenFOAM by examining three representative cases: the U-bend duct, the NACA0012 airfoil, and the Toyota AYGO X vehicle geometry. For each case, the meshing procedure and

the results are presented in order to highlight differences in the predictions and to justify the need for EVA.

- Chapter 4 introduces the concept of EVA. The continuous adjoint used for constructing a surrogate turbulent viscosity is then developed, together with an interpretation of the procedure as an optimization problem, including the sensitivity-computation methods employed.

- Chapter 5 presents the results of applying EVA to selected cases. The surrogate turbulent viscosity fields are analyzed, and their impact is assessed both on the flow features and on the main performance metrics, in comparison with the baseline RANS and the corresponding DES results.

- Chapter 6 examines how ShpO can be linked with and profit of the EVA, with an application to the isolated NACA0012 airfoil.

- Finally, Chapter 7 provides a list of conclusions, the main findings of this thesis are summarized and proposals are made for future extensions and further development of the methodology.

Chapter 2
Turbulence

A phenomenon can be described as chaotic when a problem exhibits high sensitivity to initial conditions; that is, very small changes lead to drastically different outcomes, and as a result, long-term prediction becomes practically impossible. Turbulence is a characteristic example of such a phenomenon, with a 3D nature and time-dependent; due to its stochastic character, a strictly deterministic description is not feasible. The exact mathematical formulation of turbulence remains one of the greatest unsolved problems in physics, and accurate predictions are still an open and active field of research. In everyday life, turbulence can be observed in many examples, such as the vortices that form around a rock in a river or the irregular swirling patterns in a car's exhaust gases.

Solving the Navier–Stokes equations requires the use of numerical methods for the modeling of turbulence, which are associated with extra computational cost. The exponential progress of technology has led to a tremendous increase in available computational power and has been a driving force for the improvement and development of new, more accurate computational models, allowing us to achieve and approximate with high accuracy many physical problems in fields such as aeronautics and the automotive industry that, only a few decades ago, would have seemed like an unattainable dream.

The main methodologies that have been developed in recent years for turbulence modeling are:

- Direct Numerical Simulation (DNS),
- Large Eddy Simulation (LES),
- Hybrid RANS/LES approaches,
- Unsteady Reynolds-Averaged Navier–Stokes (URANS),
- Reynolds-Averaged Navier–Stokes (RANS).

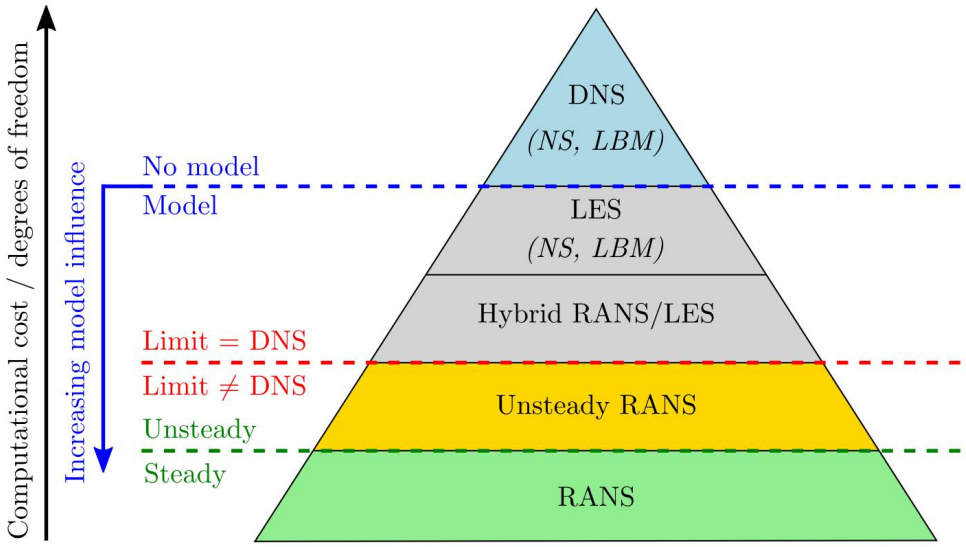

Figure 2.1: Hierarchy of turbulence models, illustrating the trade-off between computational cost and predictive, from accuracy [13].

The above approaches are often illustrated in the literature in the form of a pyramid, where the base consists of the most computationally economical models. These models rely on simplifications and assumptionsFocusing toward the top of the pyramid, the physical detail and predictive capability increase, but the computational cost rises accordingly.

As observed in Fig. 2.1 and Fig. 1.1, Direct Numerical Simulation (DNS) [14] constitutes the most accurate and fundamental computational approach for solving the Navier–Stokes equations, as it directly solves the full mass and momentum conservation equations without any modeling assumptions. Its goal is the complete resolution of all temporal and spatial scales of turbulence, from the largest eddies which contain the greatest share of kinetic energy to the smallest disturbances, known as the Kolmogorov scales. These requirements exceed the capabilities of most conventional computers and restrict DNS to the use of supercomputers and to highly simplified geometries or fundamental research. A more manageable and practical alternative is the Large Eddy Simulation (LES) method [15, 16] , which is based on filtering the turbulence spectrum, separating the large eddies from the small ones: it directly resolves the most energetically significant structures of the flow (large eddies), while the smaller ones, below a certain filter length (cut-off length scale), are modeled through appropriate subgrid-scale models. Although it can provide a highly reliable description of the main mechanisms of turbulence, its computational cost often remains prohibitive for many industrial applications, especially in complex geometries and at high Reynolds numbers.

Subsequently, methods such as DES and RANS will be analyzed, which progressively reduce the computational cost, but with a corresponding reduction in the fidelity of the results and the accuracy with which the turbulence is captured.

2.1 Governing Equations for Incompressible Flow

The governing equations describe fluid mechanics and constitute the mathematical formulation of the laws of physics; specifically, they concern the conservation of mass, momentum, and energy. In the present work, incompressible flows are described by the continuity equation (2.1) and the momentum equation (2.2), given by:

$$\nabla \cdot v = 0 \tag{2.1}$$

$$\frac{\partial v}{\partial t} + (v \cdot \nabla)v = -\nabla p + \nabla \cdot (\nu \nabla v) \tag{2.2}$$

where $\mathbf{v}$ denotes the velocity vector field, p the pressure scaled by the constant fluid density, and ν the kinematic viscosity.

2.2 Reynolds-Averaged Navier–Stokes (RANS)

The Reynolds-Averaged Navier–Stokes (RANS) equations are a fundamental tool in the modeling of turbulent flows and provide a computationally efficient compromise between accuracy and computational requirements [17]. Although RANS does not capture the detailed turbulence dynamics with the fidelity of methods such as LES or DES, it is widely used in many practical applications due to its numerical stability and computational efficiency. The central idea behind the RANS approach is that, in turbulent flows, any instantaneous quantity $f(x,t)$ can be decomposed into the sum of two components, a time-averaged mean and a fluctuating part:

$$f(x,t) = \bar{f}(x) + f'(x,t) \tag{2.3}$$

The mean value is defined as a time average over a time interval T, satisfying:

$$\bar{f} = \frac{1}{T} \int_{t_0}^{t_0+T} f(t)\,\mathrm{d}t \tag{2.4}$$

under the condition that the fluctuation has zero mean, that is, $\overline{f'} = 0$.

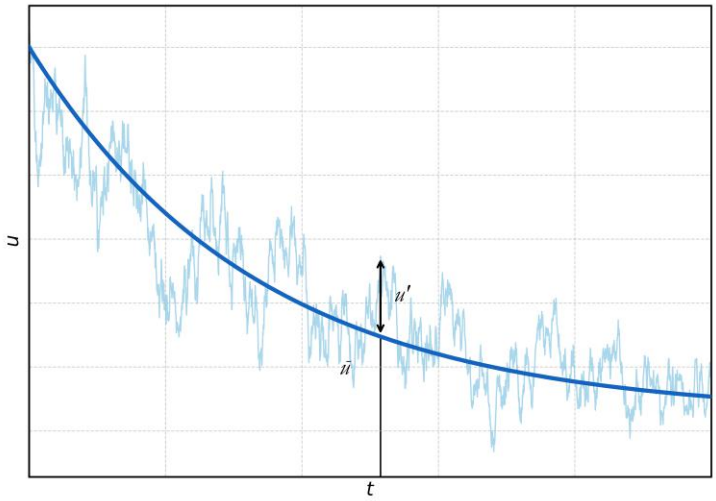

Figure 2.2: Time-averaged velocity field and velocity fluctuations

Applying Reynolds averaging to the Navier–Stokes equations yields the RANS equations, which describe the evolution of the mean fields. For incompressible flow, the equations take the form:

$$\frac{\partial \bar{v}_i}{\partial x_i} = 0 \tag{2.5}$$

$$\frac{\partial \bar{v}_i}{\partial t} + \bar{v}_j \frac{\partial \bar{v}_i}{\partial x_j} = \frac{\partial}{\partial x_j}\left[-\bar{p}\,\delta_{ij} + 2\nu\,\bar{S}_{ij} - \overline{v_i' v_j'}\right] \tag{2.6}$$

where the mean strain-rate tensor is defined as:

$$\bar{S}_{ij} = \frac{1}{2}\left(\frac{\partial \bar{v}_i}{\partial x_j} + \frac{\partial \bar{v}_j}{\partial x_i}\right) \tag{2.7}$$

The term $\overline{u_i' u_j'}$, known as the Reynolds stress tensor, represents the effects of turbulent fluctuations on the mean field. These stresses are unknown and must be modeled in order to close the system of equations. The most commonly used approach to address this closure problem is the Boussinesq hypothesis, which introduces a turbulent viscosity ν_t and expresses the Reynolds stress tensor as:

$$-\overline{v_i' v_j'} = \tau_{ij}^R = \nu_t\left(\frac{\partial \bar{v}_i}{\partial x_j} + \frac{\partial \bar{v}_j}{\partial x_i}\right) - \frac{2}{3}k\,\delta_{ij} \tag{2.8}$$

where:

$$k = \frac{1}{2}\overline{v_i' v_i'} \tag{2.9}$$

is the turbulent kinetic energy. The turbulent viscosity ν_t is not known a priori and is computed using additional transport equations provided by turbulence models such as Spalart–Allmaras, $k-\epsilon$ [18], $k-\omega$ [19], $k-\omega$ SST [20], and others.

Thus, based on Eqs. (2.7)–(2.9), the RANS continuity and momentum equations for steady, incompressible mean flows can be expressed as follows:

$$R^p = -\frac{\partial v_j}{\partial x_j} = 0 \tag{2.10}$$

$$R_i^v = v_j \frac{\partial v_i}{\partial x_j} - \frac{\partial}{\partial x_j}\left[(\nu + \nu_t)\left(\frac{\partial v_i}{\partial x_j} + \frac{\partial v_j}{\partial x_i}\right)\right] + \frac{\partial p}{\partial x_i} = 0 \tag{2.11}$$

2.3 The Spalart–Allmaras Model

The Spalart–Allmaras (S–A) model is a one-equation turbulence model for incompressible flows [21]. The core idea of the model is the introduction of an auxiliary turbulence variable, $\widetilde{\nu}$, which is related to the turbulent viscosity ν_t. The variable $\widetilde{\nu}$ is transported through the following transport equation:

$$\frac{D\widetilde{\nu}}{Dt} = P(\widetilde{\nu}) - D(\widetilde{\nu}) + T(\widetilde{\nu}) \tag{2.12}$$

where $P(\tilde{\nu})$ denotes the production term, $D(\tilde{\nu})$ the destruction term, and $T(\tilde{\nu})$ the diffusion term.

The turbulent viscosity ν_t is obtained from:

$$\nu_t = \widetilde{\nu}\, f_{v1} \tag{2.13}$$

with:

$$f_{v1} = \frac{X^3}{X^3 + C_{v1}^3} \tag{2.14}$$

The full differential transport equation for $\widetilde{\nu}$ within the RANS framework is given by:

$$\begin{aligned}\frac{\partial \widetilde{\nu}}{\partial t} + u_j \frac{\partial \widetilde{\nu}}{\partial x_j} = {} & C_{b1}\,(1 - f_{t2})\,\widetilde{S}\,\widetilde{\nu} + \frac{1}{\sigma}\Big(\nabla \cdot \big((\nu + \widetilde{\nu})\,\nabla\widetilde{\nu}\big) + C_{b2}\,(\nabla\widetilde{\nu})^2\Big) \\ & - \left(C_{w1} f_w - \frac{C_{b1}}{\kappa^2} f_{t2}\right)\left(\frac{\widetilde{\nu}}{d}\right)^2 + f_{t1}\,\Delta U^2\end{aligned} \tag{2.15}$$

The modified vorticity $\widetilde{S}$ is computed as:

$$\widetilde{S} = S + \frac{\widetilde{\nu}}{\kappa^2 d^2}\, f_{v2} \tag{2.16}$$

where:

$$S = \sqrt{2 S_{ij} S_{ij}} \tag{2.17}$$

The correction term f_{v2} is given by:

$$f_{v2} = 1 - \frac{X}{1 + X f_{v1}} \tag{2.18}$$

The damping term includes f_w, which is defined as:

$$f_w = g\left[\frac{1 + C_{w3}^6}{g^6 + C_{w3}^6}\right]^{1/6} \tag{2.19}$$

where the parameter g depends on r:

$$g = r + C_{w2}\left(r^6 - r\right) \tag{2.20}$$

and r is computed as:

$$r = \min\left(\frac{\widetilde{\nu}}{\widetilde{S}\kappa^2 d^2}, 10\right) \tag{2.21}$$

The additional correction term f_{t2} is computed as:

$$f_{t2} = C_{t3} e^{-C_{t4}X^2} \tag{2.22}$$

The model constants used in the computations are:

$$\sigma = \frac{2}{3}, \qquad C_{b1} = 0.1355, \qquad C_{b2} = 0.622, \qquad \kappa = 0.41, \qquad C_{w1} = 3.239, \qquad C_{v1} = 7.1 \tag{2.23}$$

In summary, the SA model is a particularly effective choice for low-Reynolds-number simulations when the viscous sublayer of the boundary layer is sufficiently resolved, that is, for y^+ values close to unity. This requirement implies a very fine mesh near walls and, consequently, increased computational cost due to the larger number of cells. To maintain simulation reliability without excessive mesh refinement in the near-wall region, wall functions are applied in the present work. The generated mesh is consistent with the theoretical requirements for the use of wall functions, enabling effective use of the model and the production of reliable results with reduced demands on computational resources.

2.4 Wall Functions

Wall functions are empirical or semi-empirical relations that approximate the flow behavior in the part of the boundary layer that is not directly resolved by the mesh, bridging the transition from the wall to the resolved region. This philosophy corresponds to a high-Reynolds-number (High-Re) approach, in contrast to Low-Re methods, which require detailed resolution of the near-wall region and typically $y^+ \approx 1$.

For the formulation of wall functions, the dimensionless quantities y^+ and u^+ are introduced:

$$y^+ = \frac{u_\tau\, y}{\nu}, \qquad u^+ = \frac{u}{u_\tau} \tag{2.24}$$

where y is the distance of the center of the first cell from the wall, ν is the kinematic viscosity of the fluid, u is the tangential component of the velocity, and u_τ is the friction velocity, with

$$u_\tau = \sqrt{\frac{\tau_w}{\rho}} \tag{2.25}$$

Based on y^+, the typical velocity profile in a turbulent boundary layer is commonly divided into three regions: the viscous sublayer ($y^+ \sim 1$–5), the buffer zone ($y^+ \sim 5$–30), and the logarithmic region ($y^+ \gtrsim 30$), where the law of the wall applies,

$$u^+ = \frac{1}{\kappa}\ln\left(y^+\right) + C. \tag{2.26}$$

In the simulations presented in this thesis, the near-wall treatment for the turbulent viscosity ν_t is selected according to the geometry and the available near-wall mesh resolution [22].

For some of the test cases, a low-Reynolds-number, wall-resolved treatment is adopted, for which the imposed boundary condition at the solid wall is

$$\nu_t = 0, \tag{2.27}$$

i.e. the turbulent viscosity is set to zero at the wall. The resulting y^+ values are then computed and used as a criterion for assessing the adequacy of the near-wall discretization.

For other test cases, where the mesh is not sufficiently fine to fully resolve the viscous sublayer, the Spalding wall function is employed [23]. This wall law provides a single relation valid across the full range of y^+, including the buffer zone:

$$y^+ = u^+ + \frac{1}{E}\left[\exp\left(\kappa u^+\right) - 1 - \kappa u^+ - \frac{1}{2}\left(\kappa u^+\right)^2 - \frac{1}{6}\left(\kappa u^+\right)^3\right]. \tag{2.28}$$

Here, $\kappa = 0.41$ is the von Kármán constant and $E = 9.53$. The use of a wall function is particularly appropriate when the first cell centre lies at relatively higher y^+ values (indicatively $y^+ \approx 40$–100). In OpenFOAM, wall functions are applied by computing the value or behaviour of ν_t in the near-wall cells so that the modelled near-wall shear remains consistent with the selected wall law.

2.5 Detached Eddy Simulation (DES)

Detached Eddy Simulation (DES) is one of the most widely used hybrid approaches for turbulence simulation in high Reynolds number applications with significant flow separation. It was introduced in 1997 by Spalart and co-workers, with the aim of bridging the gap between RANS and LES [24]. Unlike steady RANS computations, DES is inherently time-dependent and, therefore, requires an unsteady integration (Unsteady RANS), which constitutes a primary reason for its increased computational cost. The central idea of DES is to use a single turbulence model that behaves as a RANS model in near-wall regions and as an LES model in the outer flow, depending on the local grid resolution. This transition is not imposed through an explicit zonal treatment, instead, it arises naturally from the model formulation and the mesh, leading to what is commonly referred to as a gray zone between the two approaches. The criterion that governs the transition between the RANS and LES regions is based on a modified filter length scale. In the original formulation [24] , the model length scale is defined as:

$$\tilde{d} = \min\left(d_w,\, C_{DES}\,\Delta\right) \tag{2.29}$$

where d_w is the (standard) distance to the nearest wall, Δ is a characteristic cell size, and C_{DES} is an empirical constant. In this way, when the grid near the wall is relatively coarse, RANS is activated, whereas when the grid is sufficiently fine, LES is activated. This concept allows DES to employ fine resolution only where necessary, significantly reducing the computational cost compared with full LES.

To the improve accuracy further, variants of the original model have been developed, such as Delayed Detached Eddy Simulation (DDES) [25], in which a shielding mechanism (shielding function) is introduced to extend the RANS behavior near walls. The modified expression for the length scale becomes:

$$\tilde{d} = d_w - f_d \max\left(0,\, d_w - C_{DES}\,\Delta\right) \tag{2.30}$$

where f_d is an empirical function that takes the value 1 in LES regions and 0 in RANS regions. Even more recent versions, such as Improved DDES (IDDES) [26], incorporate more complex terms to achieve a smoother and more controlled transition between RANS and LES, particularly in boundary layers and regions with partial separation. Indicatively, a more complex form used in the transition can be expressed as:

$$\tilde{d} = f_d\left(1 + f_{d,\text{wall}}\right) d_w + \left(1 - f_d\right) C_{DES}\,\Delta \tag{2.31}$$

DES and its variants offer a significant advantage in applications where the flow remains mostly attached to surfaces, allowing RANS to dominate over much of the domain, while LES provides the desired accuracy in separated regions. They are often a realistic choice when improved accuracy is required compared with classical RANS, without incurring the prohibitive computational cost of LES or DNS. Thus, for complex flows, especially in industrial applications, DES can deliver satisfactory result quality within more realistic computational times.

2.6 OpenFOAM

The simulations presented in this thesis are carried out with OpenFOAM (Open Field Operation and Manipulation) [27]. is a software package/toolbox that can be used to solve differential equations. Its development began in the 1990s at Imperial College, and since 2004 it has been distributed as open-source software. The source code is written entirely in C++, giving the user the ability not only to modify existing solvers but also to develop new ones from scratch, tailored to the needs of a specific application. A characteristic example of this flexibility is the development of optimization tools, specifically adjoint-based methods (e.g., shape optimization, topology optimization, and related approaches), by the PCOpt Unit of the NTUA. Building on this existing infrastructure and the available codes, the following chapters present the formulation and implementation of the optimization problem considered in this work, with a focus on the TMA (EVA).

Despite this wide range of applications, OpenFOAM is used primarily in Computational Fluid Dynamics (CFD). Some of its main advantages include its parallelization capabilities, as well as built-in mesh-generation tools such as `blockMesh` and `snappyHexMesh` [28, 29]. The discretization of the governing equations is carried out using the Finite Volume Method (FVM), where the quantities of interest are computed at the cell centroids. Finally, OpenFOAM provides a large set of solvers for different flow regimes and fluid properties, based on algorithms such as SIMPLE and PIMPLE, among others [30, 31].

Chapter 3
Comparison of RANS and DES Models

In this section, it is examined how the choice of turbulence model between RANS and DES affects the results of a CFD analysis. The comparison aims, on the one hand, to highlight the extent to which the modeling choice influences the accuracy of the predictions, both in the flow fields and in the derived quantities, and, on the other hand, to demonstrate the increased computational cost associated with the use of higher-fidelity methods. Such a trade-off appears frequently both in simpler engineering problems and, more importantly, in industrial applications, when the RANS approach does not perform adequately and a more detailed description of the flow is required.

Within this framework, the present work examines a set of representative test cases using both RANS and DES, with the objective of identifying the regions and flow regimes where the RANS approach deviates from the higher-fidelity solution. Specifically, the following are analyzed: (Case A) a curved U-bend duct, (Case B) the NACA0012 airfoil, and (Case C) the Toyota Aygo X vehicle, which is simulated in an experimental wind-tunnel setup.

Each CFD analysis requires the generation of the computational mesh. The density and distribution of the nodes must achieve satisfactory accuracy in describing the physical phenomena without excessive computational cost. In the following, the cases are presented in detail, with an emphasis on mesh generation and the definition of the corresponding boundary conditions, while subsequently the results of the simulations performed in OpenFOAM are provided and analyzed.

3.1 Case A: U-Bend

3.1.1 Mesh Generation

Case A (U-bend), concerns flow through a U-bend configuration. This is a widely encountered internal-flow setup (e.g., in automotive ducting and related internal-flow systems). The experimental configuration used as a reference in the present work is that of Coletti et al. [32].

It consists of a 3D square-duct channel with hydraulic diameter $D_h = 0.075\,\mathrm{m}$, including an inlet straight section of length $23.3\,D_h$, a U-bend with outer radius $1.26\,D_h$, and an

outlet straight section of length $20\,D_h$. However, in order to reduce computational cost within the scope of this thesis, the numerical simulation of the flow field is carried out both in 2D using a shortened duct, in which case the upstream and downstream legs of the bend are limited to a length of $10\,D_h$.

For the construction of the geometry and the generation of a structured mesh, the `blockMesh` tool of OpenFOAM was used. Using `blockMesh` also enabled the desired refinement, particularly near the walls. This was accomplished through multi-grading. Specifically, in the cross-stream direction of the blocks, the mesh is refined towards the walls, while a more uniform distribution is maintained in the core-flow region.

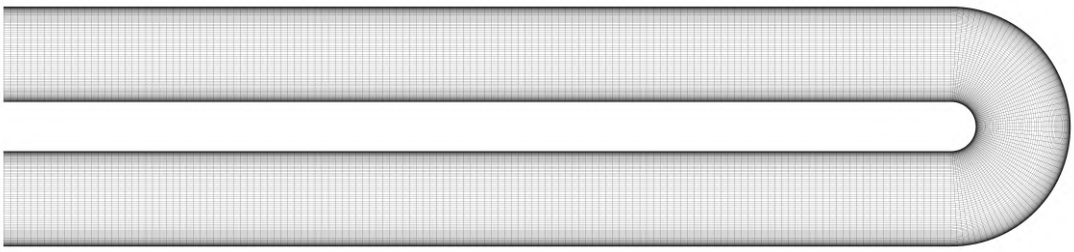

(a)

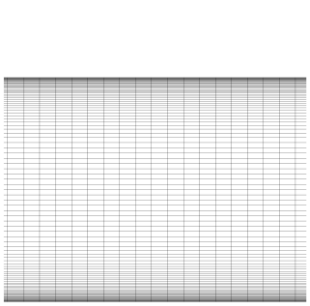

(b)

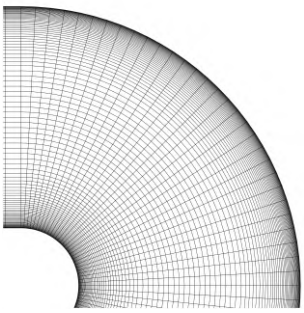

(c)

Figure 3.1: Case A: Computational mesh: (a) overall domain, (b) zoomed view highlighting the mesh refinement in the straight section, (c) zoomed view highlighting the mesh refinement in the bend region.

The same mesh is used for both the RANS and DES simulations, for the sake of fairness. For the RANS simulations, the steady-state solver `simpleFOAM` is used in combination with the SA turbulence model. For the DES (SA) simulations, the incompressible unsteady solver `pimpleFOAM` is used. The total simulated time is 4 s, with a time step of $\Delta t = 1 \times 10^{-4}$ s. Time-averaging starts at $t = 2$ s and continues until the end of the simulation. These simulations are performed on 48 cores. The RANS computation completes in 262 s (1.88 CPUh), whereas the corresponding DES requires approximately 1.87 h (89.63 CPUh). The difference in computational cost is particularly pronounced, for the same number of cores, DES is more expensive by more than one order of magnitude compared to RANS. This discrepancy is expected, given the nature of DES as an unsteady approach, in contrast to RANS. Thus, it becomes evident in practice that a higher-fidelity simulation is inevitably accompanied by a significantly greater computational burden, i.e., by execution-time requirements of a different order of magnitude. Finally, in both cases (RANS and DES), the same boundary conditions

are used, as summarized in Tab. 3.1.

	Inlet	**Outlet**	**Walls**
U	`fixedValue` (8.4 0 0)	`zeroGradient`	`noSlip`
p	`zeroGradient`	`fixedValue`	`zeroGradient`
`nuTilda` ($\tilde{\nu}$)	`fixedValue`	`zeroGradient`	`fixedValue`
`nut` (ν_t)	`calculated`	`calculated`	`nutLowReWallFunction`

Table 3.1: Case A: Boundary conditions.

3.1.2 Results

The convergence of the RANS and DES simulations is shown in Fig. 3.2.

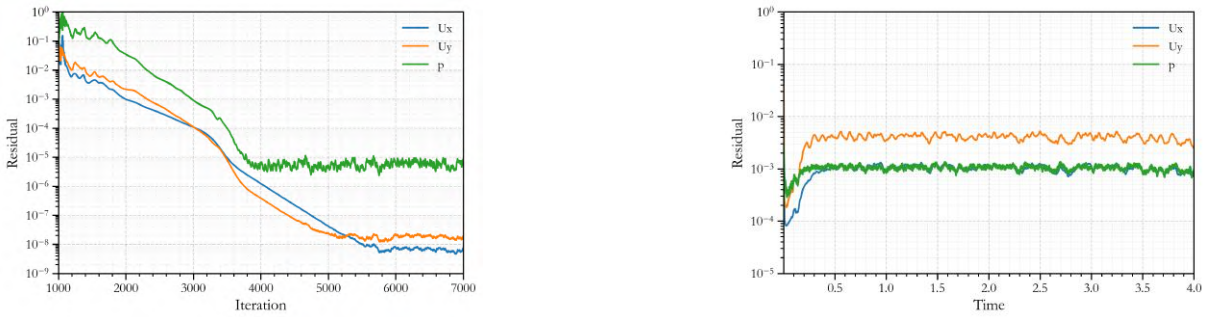

(a) (b)

Figure 3.2: Case A: Residuals of the governing equations for (a) RANS and (b) DES simulations.

The results are then compared, revealing clear differences between the RANS and DES approaches. In DES, the solution is unsteady, allowing the flow fields to evolve in time and to resolve unsteady turbulent structures. As shown in the Fig. 3.3, DES allows turbulent structures to appear and develop in the flow field, since it resolves the large eddies in regions where flow separation occurs.

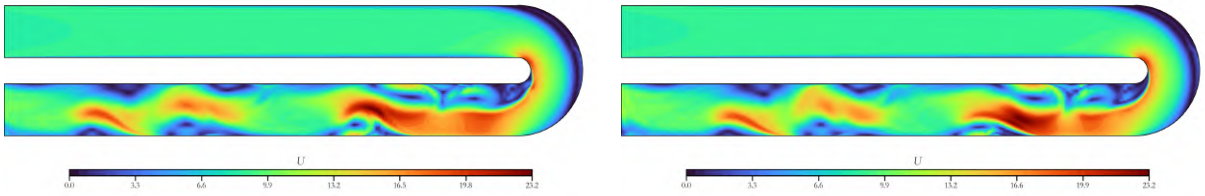

(a) (b)

Figure 3.3: Case A: Instantaneous velocity magnitude for the DES simulation at (a) $t = 3.9$ s and (b) $t = 4.0$ s. The unsteadiness of the flow, as simulated with the DES model, is apparent.

For improved comparison with the RANS results, it is common to also examine the time–averaged DES fields. These quantities are obtained by time-averaging the instantaneous solutions (over $t = 2$–4 s), and they represent the mean flow behavior, making them directly comparable to the RANS solution.

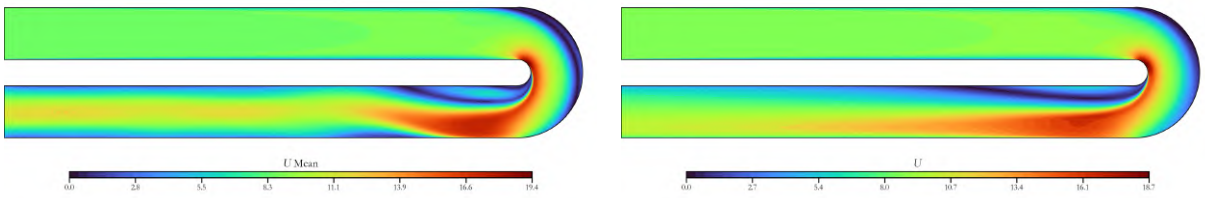

(a) (b)

Figure 3.4: Case A: Velocity magnitude field for (a) the time-averaged DES and (b) the RANS.

Nevertheless, for the mean field, substantial differences between DES and RANS are observed. The main discrepancy is associated with separation along the inner bend and the formation of a recirculation bubble. RANS tends to predict a more pronounced recirculation region, both in terms of its streamwise extent and its height, compared to DES. This leads to a different redistribution of momentum and, consequently, to lower acceleration of the flow towards the outer wall compared to DES. In addition, for the present case, RANS does not adequately reproduce a secondary recirculation region near the bottom wall of the U bend, which is captured more clearly in the unsteady DES run. These differences can also be identified in the pressure field Fig. 3.5 as well as in the turbulent viscosity field Fig. 3.6.

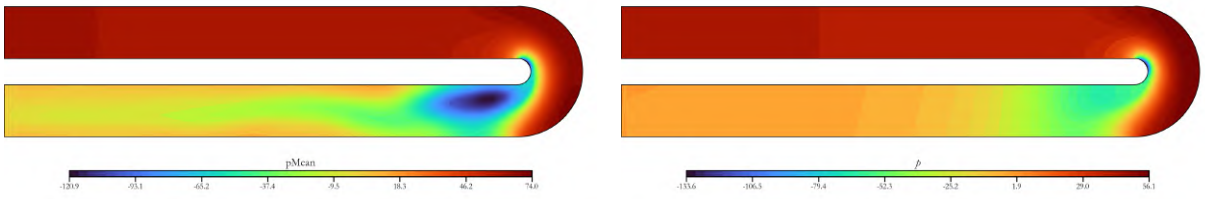

(a) (b)

Figure 3.5: Case A: Pressure field for (a) the time-averaged DES and (b) the RANS.

In particular, for ν_t turbulent viscosity, the maximum values predicted by RANS are significantly higher than those obtained from DES. The maximum value in RANS is $\sim \times 9$ larger than the maximum value of the time–averaged DES field, and similarly larger than the maxima observed in the instantaneous DES fields. This discrepancy indicates a substantially different order of magnitude for turbulent viscosity, which directly affects momentum diffusion and the representation of separation and mixing in the U bend. It is therefore reasonable to consider that this difference in ν_t contributes to the pronounced deviations between the RANS and DES fields.

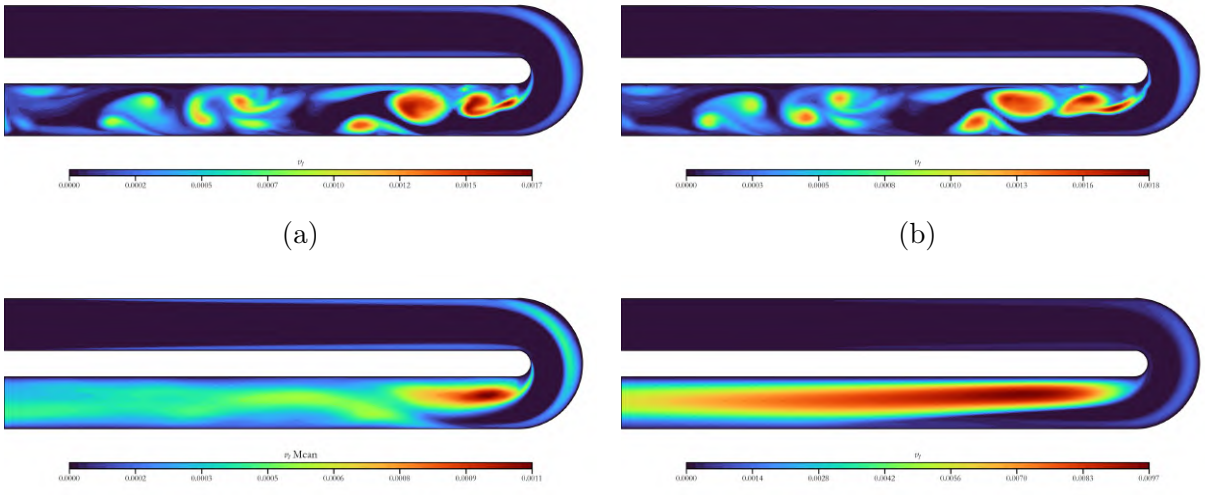

Figure 3.6: Case A: ν_t field for (a) instantaneous DES at $t = 3.9$ s, (b) instantaneous DES at $t = 4.0$ s, (c) time-averaged DES, (d) RANS.

3.2 Case B: NACA0012

3.2.1 Mesh Generation

Next, Case B considers external aerodynamics around the symmetric NACA0012 airfoil. A 2D C-type mesh was generated around the airfoil, with near-wall refinement and gradual stretching towards the far field.

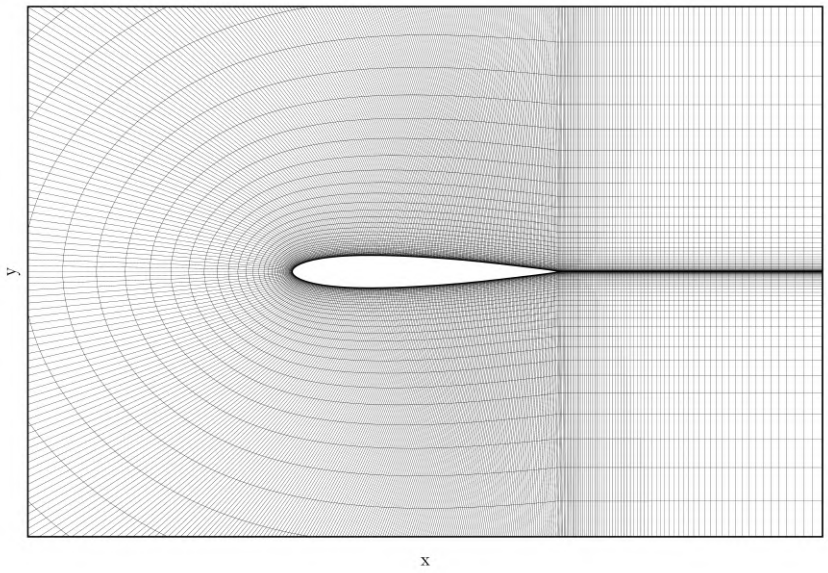

Figure 3.7: Case B: Computational mesh.

The angle of attack is $AoA = 12°$, where separation begins near the trailing edge, an

effect that RANS models often struggle to predict accurately. The flow conditions are $Re = 10^6$.

As in Case A, the RANS and DES simulations in Case B are performed using the same numerical setup. These simulations were performed on 48 cores. The RANS computation completes in 494 s (1.95 CPUh), whereas the corresponding DES requires 0.75 h (35.77 CPUh). For the same number of cores, DES is more expensive by more than one order of magnitude compared to RANS; this increase is expected, since DES is an unsteady, higher-fidelity approach and therefore entails substantially higher computational demands.

Finally, in both cases (RANS and DES), the same boundary conditions were used, as summarized in Tab. 3.2.

	Inlet	**Pressure/Suction**
U	`freestream` (58.686 12.474 0)	`fixedValue`
p	`outletInlet`	`zeroGradient`
`nuTilda` ($\tilde{\nu}$)	`freestream`	`fixedValue`
`nut` (ν_t)	`calculated`	`nutUSpaldingWallFunction`

Table 3.2: Case B: Boundary conditions.

3.2.2 Results

The convergence of the RANS and DES simulations is shown in Fig. 3.8b.

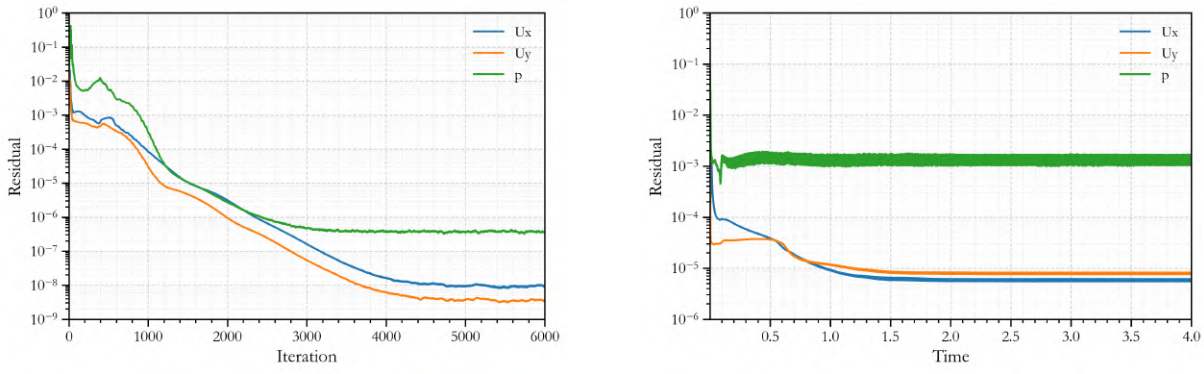

(a) (b)

Figure 3.8: Case B: Residuals of the governing equations for (a) RANS and (b) DES simulations.

Similarly to the U bend case, the discrepancies between RANS and DES become more pronounced as the flow approaches separation conditions, namely at higher angles of attack. For this reason, $\alpha = 12°$ was selected as this corresponds to incipient separation, particularly near the trailing edge, while the flow has not yet reached full stall.

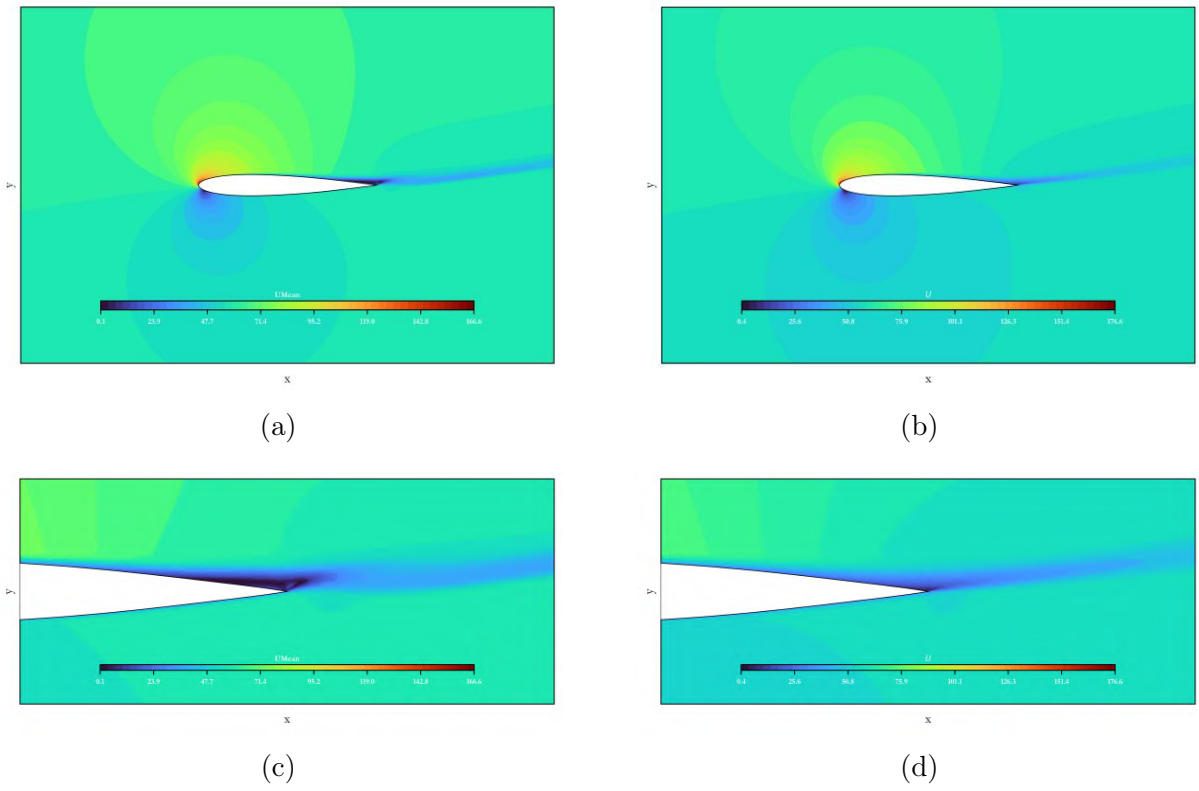

(a) (b)

(c) (d)

Figure 3.9: Case B: Velocity magnitude field for (a) the time-averaged DES and (b) the RANS, (c) zoomed view near the trailing edge for the time-averaged DES and (d) zoomed view near the trailing edge for the RANS.

The results indicate that, for $\alpha = 12°$, flow separation in the trailing edge region is clearly stronger in DES compared to the corresponding RANS results, which directly affects the overall aerodynamic behaviour of the airfoil. Variations in both the extent and the intensity of separation modify the pressure distribution along the surface, leading to different values of the aerodynamic coefficients (e.g. C_L, C_D) 3.3 and, consequently, to different conclusions depending on the application.

	C_L	C_D
RANS	1.21932	2.2395×10^{-2}
DES	1.12985	2.4018×10^{-2}

Table 3.3: Case B: Comparison of lift and drag coefficients (C_L, C_D) between RANS and DES.

These differences are also reflected on the pressure coefficient C_p distributions Fig. 3.10.

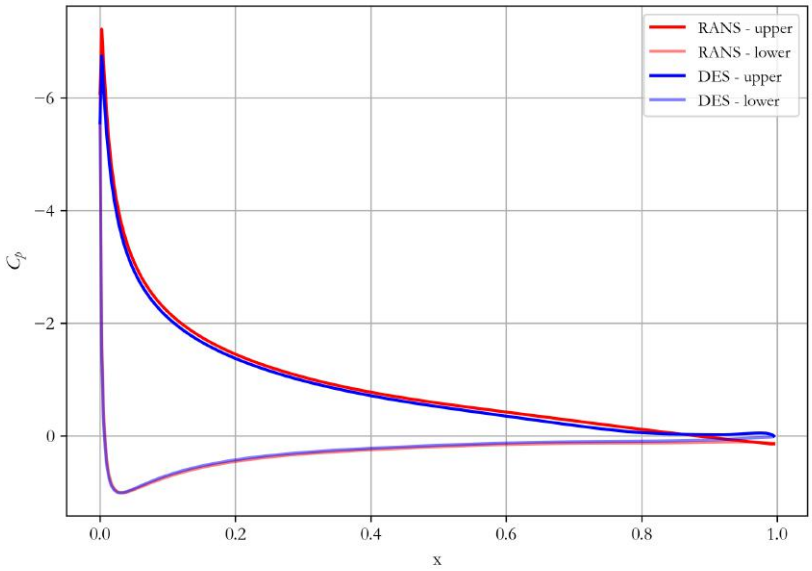

Figure 3.10: Case B: Comparison of pressure coefficient (C_p) distributions from the DES and RANS simulations.

In addition, further indications of the differences between the two approaches can be observed in the pressure fields Fig. 3.11.

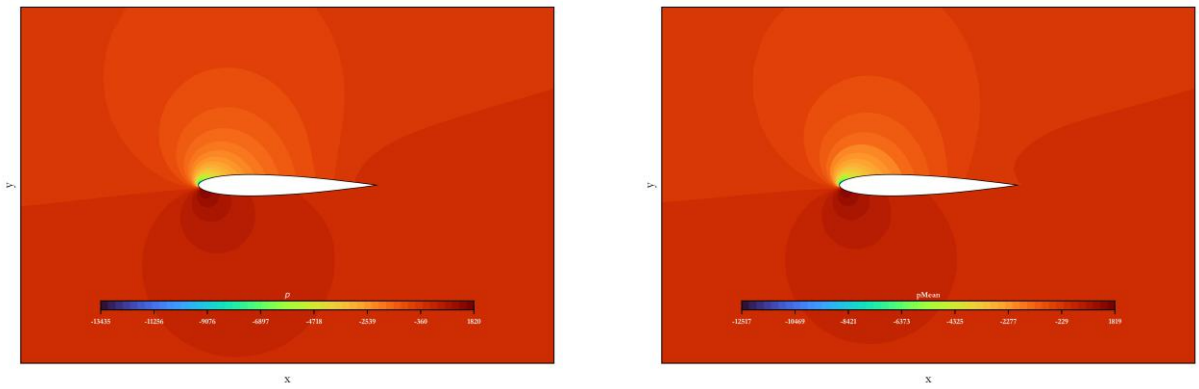

(a) (b)

Figure 3.11: Case B: Pressure field for (a) the time-averaged DES and (b) the RANS.

Likewise, the ν_t fields Fig. 3.12 obtained from DES and RANS show significant differences both in their spatial distribution and in the overall level of the values. In particular, in RANS the maximum ν_t is one order of magnitude higher than the maximum value of the time averaged DES field, as well as the corresponding instantaneous fields. At the same time, the shape and structure of the field differ noticeably between the two approaches, reflecting the different way turbulence is modelled and represented in each method.

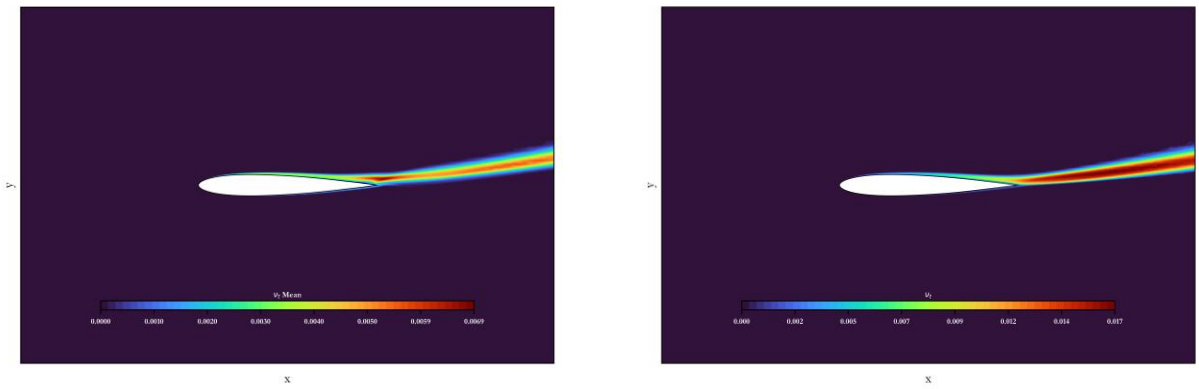

(a) (b)

Figure 3.12: Case B: ν_t field for (a) the time-averaged DES and (b) the RANS.

3.3 Case C: Toyota AYGO X

3.3.1 Mesh Generation

Case C investigates a real-world application provided by Toyota Motor Europe (TME) and focuses on the external aerodynamics of the Toyota AYGO X model.

(a) (b) (c)

Figure 3.13: Case C: Vehicle geometry shown from different viewing angles: (a) front, (b) side, and (c) isometric.

During the development of a vehicle, aerodynamic evaluation often requires repeated experimental testing to confirm that the final geometry meets the expected performance levels. A well established approach is wind tunnel testing, where the flow conditions can be controlled accurately and quantities such as the drag coefficient C_d can be measured directly. In the present study, the reference configuration includes a moving ground and wheel rotation systems. In particular, five moving belts are used, one beneath each wheel and one beneath the vehicle underbody. In this way, road motion is simulated and wheel rotation is represented realistically, both of which directly affect the flow field around the vehicle and, consequently, the aerodynamic measurements. The domain is defined as shown in the figure below, and the vehicle geometry is introduced accordingly, as it would be in the experiment.

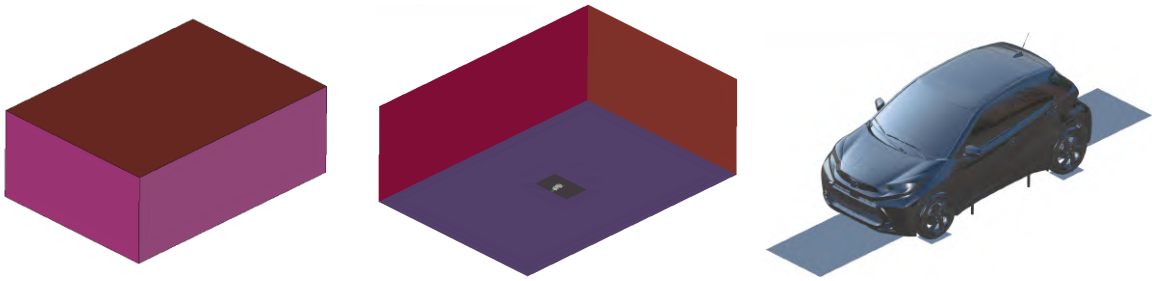

(a) (b) (c)

Figure 3.14: Case C: Vehicle computational setup: (*a,b*) computational domain around the vehicle, (*c*) wind-tunnel configuration showing the vehicle installation, including the road and wheel belt systems and the corresponding supports.

Once the geometry is defined, and before meshing, local refinement regions are defined, where increased resolution is required because more complex flow phenomena are expected. This is done by specifying refinement zones around the wheels, the mirrors, and in regions where separation is likely, such as the rear wake and near edges or corners where strong velocity gradients and vortical structures occur. Two additional, larger scale refinement regions that enclose the entire geometry are then defined, aiming to better capture the near wake and the main flow structures, while keeping the overall cell count under control Fig. 3.15.

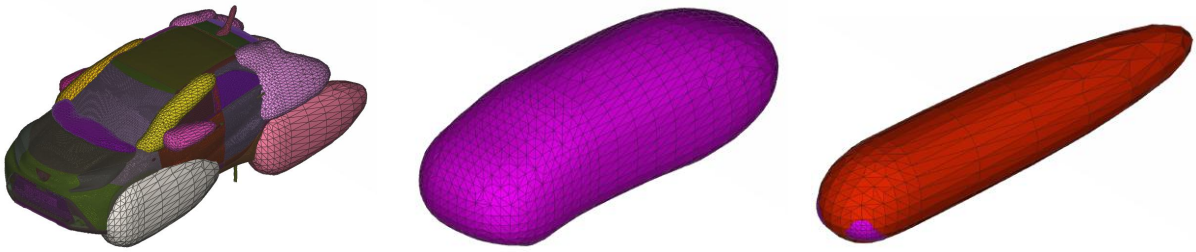

(a) (b) (c)

Figure 3.15: Case C: Refinement regions: (*a*) local refinements around key features, (*b*) enclosing refinement region, (*c*) outer refinement region encompassing all zones.

The final mesh consists of approximately 81 million cells, featuring high refinement in the specified local refinement regions, while also ensuring adequate boundary layer resolution on the solid surfaces of the geometry. The final mesh resulting from the meshing process is shown in Fig. 3.16 and Fig. 3.17, illustrating both the surface mesh and the volumetric mesh of the entire computational domain.

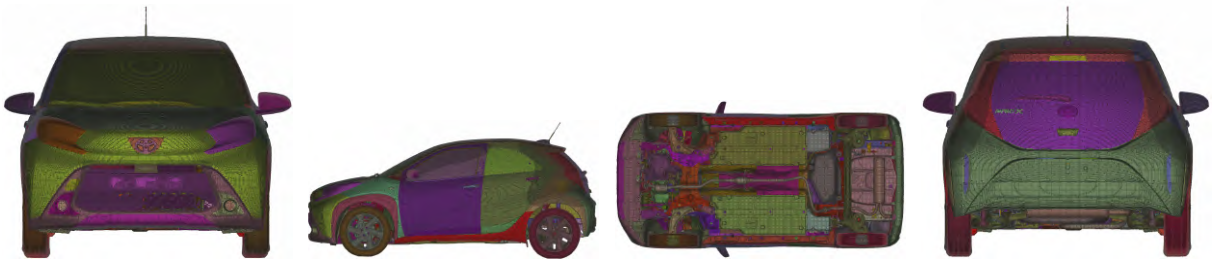

(a) (b) (c) (d)

Figure 3.16: Case C: Surface mesh of the vehicle shown from different viewing angles.

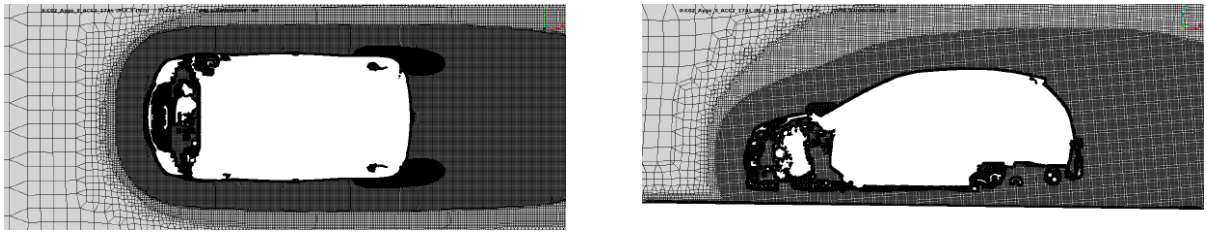

(a) (b)

Figure 3.17: Case C: Mesh on (a) the x–z plane and (b) the y–z plane.

The RANS simulation is performed using the steady-state OpenFOAM solver `simpleFOAM`, in combination with the SA turbulence model. For the DES (SA) simulation, the converged RANS solution is used as the initial condition, and the incompressible unsteady solver `pimpleFOAM` is then employed. The total simulated time is 5 s, with a time step of $\Delta t = 1.4 \times 10^{-4}$ s. Time-averaging starts at $t = 2$ s and continues until the end of the simulation. These simulations are performed on 512 cores. The RANS computation completes in 2 h (3000 CPUh), whereas the corresponding DES requires 22 h (25000 CPUh). Compared to the previous cases, the difference in computational cost is clearly more pronounced and critical here. Consequently, the choice between DES and RANS entails a markedly higher computational cost, which can often become a practical limitation during design phases where rapid testing and immediate assessment of results are required.

Finally, for both the RANS and DES simulations, the same boundary conditions were used, which are summarized as follows:

	Top / Side	**Inlet**	**Outlet**	**Road**	**Belts**	**Car**
U	Symmetry	Dirichlet	Inlet-Outlet	Slip	Dirichlet	No Slip
p	Symmetry	Zero Neumann	Zero Dirichlet	Zero Neumann	Zero Neumann	Zero Neumann

Table 3.4: Case C: Boundary conditions .

3.3.2 Results

The convergence of the RANS and DES simulations is shown in Fig. 3.18a, and Fig. 3.18b.

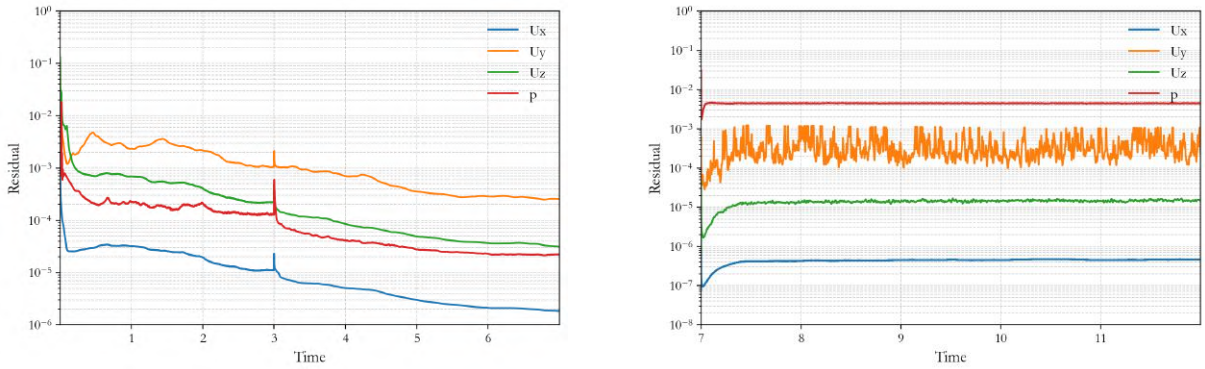

(a) (b)

Figure 3.18: Case C: Residuals of the governing equations for (a) RANS and (b) DES simulations.

A comparison of RANS and DES results in 3D and more complex geometries highlights substantial differences between the two approaches, since turbulence is inherently 3D and unsteady. In external vehicle aerodynamics, the accuracy of numerical predictions is critical, because aerodynamic design is directly linked to energy consumption and driving range and, consequently, to CO_2 emissions. Therefore, the simulation results must be sufficiently reliable to be used in evaluation workflows and design optimization processes.

Within the reliability requirements defined by the WLTP standard (Worldwide Harmonized Light Vehicles Test Procedure) [3] , a simulation is considered to have acceptable accuracy when the deviation from the corresponding wind-tunnel data does not exceed

$$\Delta(C_D A_f) = (C_D A_f)_{\text{CFD}} - (C_D A_f)_{\text{WT}} \leq \pm 0.015 \text{ m}^2, \tag{3.1}$$

where C_D is the drag coefficient and A_f is the vehicle frontal area (m^2). In the present comparison, the RANS simulations do not achieve this level of accuracy, in contrast to DES, which shows better agreement and more stable behaviour in the aerodynamic quantities of interest. The two approaches also lead to different predictions of flow development, particularly in separated regions and in the wake, which can significantly affect flow topology and the main sources of drag.

This difference can be observed clearly through the analysis of the total pressure coefficient C_{pt}. The total pressure coefficient is defined as:

$$C_{pt} = \frac{p_t - p_{t,\infty}}{\frac{1}{2}\rho U_\infty^2}. \tag{3.2}$$

An isosurface C_{pt}, as shown in Fig. 3.19, is indicative of a specific value of C_{pt}, and can be interpreted as a practical boundary separating the relatively undisturbed flow from the wake region. Downstream of the vehicle, separation and recirculation cause total pressure losses due to viscous effects and turbulent mixing. This deficit region is a defining feature of the wake and is directly linked to drag generation, as it reflects a loss of mechanical energy in the flow and, consequently, the aerodynamic resistance of the vehicle.

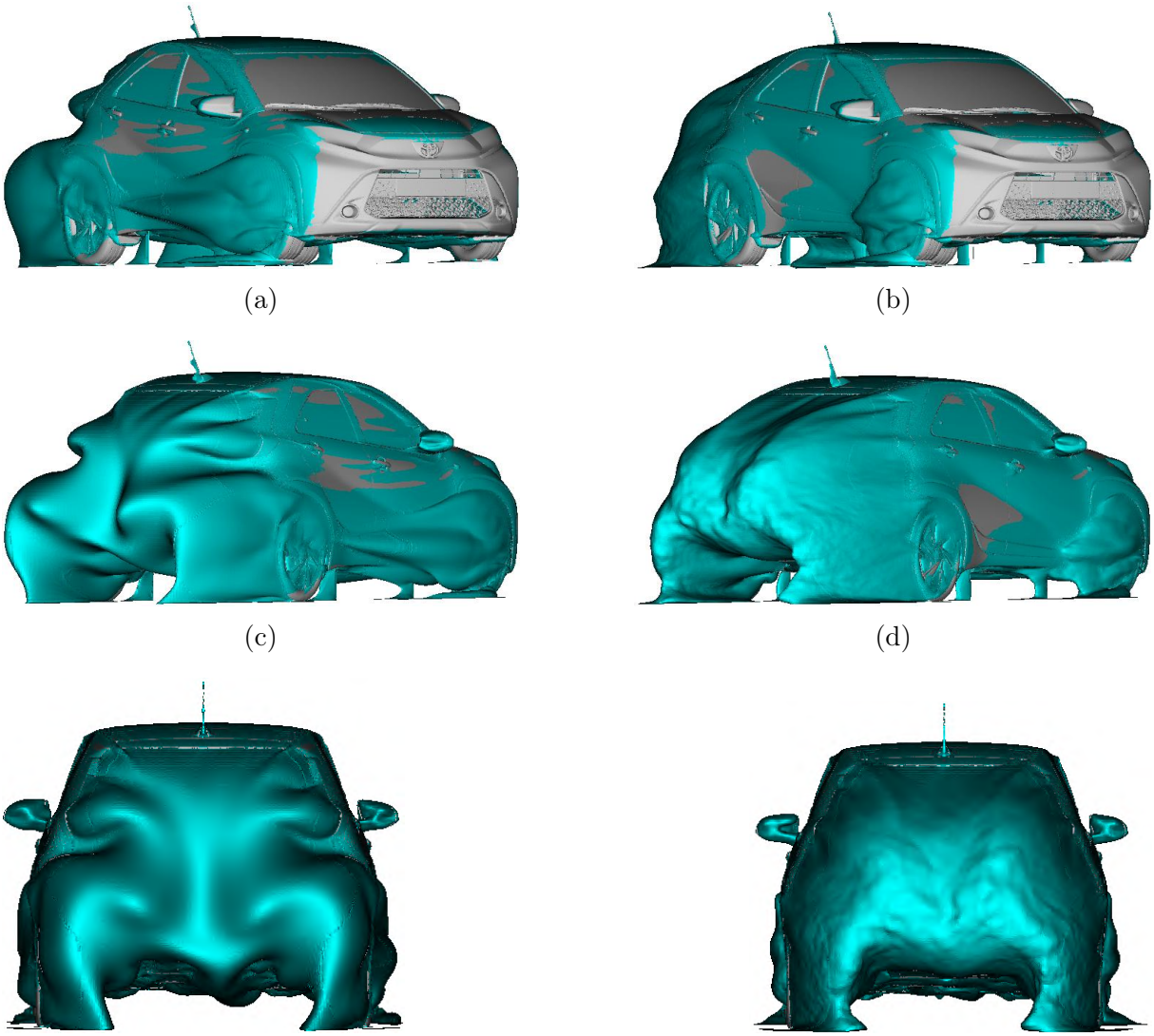

Figure 3.19: Case C: Iso-surface of C_{pt}, indicative of a specific value, shown from different viewing angles: (a,c,e) RANS and (b,d,f) DES.

The differences between the two models can lead to fundamentally different conclusions, since the wake field differs substantially in critical regions. Starting from the front wheel area, the contrast between RANS and DES in both wake shape and wake extent becomes particularly pronounced. RANS predicts a markedly larger region of total pressure deficit and recirculation than DES. More specifically, in the RANS case a dominant central wake lobe develops, extending across a large portion of the lateral and central region of the vehicle, influencing the overall flow morphology along the body, and terminating shortly upstream of the rear wheel region Fig. 3.19a and Fig. 3.19b. In contrast, DES yields a qualitatively different wake topology. Rather than a single extended lobe, it exhibits multiple smaller scale structures and a noticeably shorter recirculation length. This behaviour is consistent with the non steady nature of DES, where mixing and the evolution of shear layers around the wheels and geometric edges are captured more realistically, instead of being smoothed into a single stable lobe.

Beyond the wheel region, the most significant difference between RANS and DES arises at

the rear of the vehicle, where separation and the wake largely govern drag. In particular, near the rear lights, the two models predict distinct flow behaviors. In the RANS case, the flow tends to remain attached over a larger portion of the rear body surface, leading to a different development of the shear layer and, consequently, a different downstream wake structure. In contrast, in DES the flow separates earlier at the critical tail edges, producing a different recirculation region and a different distribution of total pressure losses behind the vehicle Fig. 3.19e and Fig. 3.19f.

The static-pressure coefficient $C_{p,s}$ distributions also provide useful insight into these differences, as they indicate where the flow remains attached and where separation occurs Fig. 3.20. In both approaches, regions of lower $C_{p,s}$ appear at the rear of the vehicle, meaning lower base pressure. However, the $C_{p,s}$ patterns differ significantly between RANS and DES. In the RANS case, in the body region where the main deviation is observed, lower pressure values and stronger spatial variations in $C_{p,s}$ appear, which is consistent with local development or influence of separation on the surface. In contrast, in DES the $C_{p,s}$ distribution at the rear is more uniform, which is consistent with a clearer or more extended separated region and the presence of a strong wake and downstream recirculation, which tends to produce a more uniform pressure distribution.

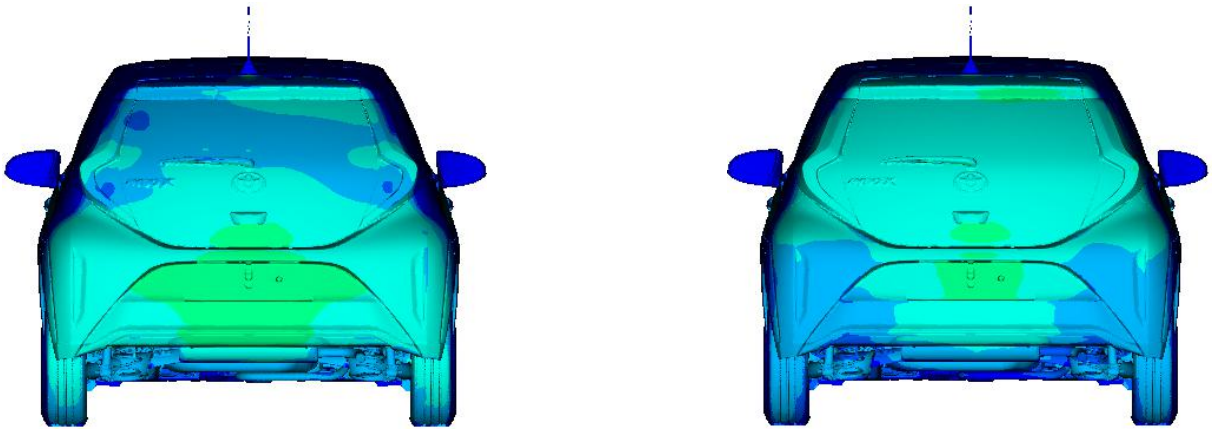

(a) (b)

Figure 3.20: Case C: Static pressure coefficient contribution for (a) RANS and (b) DES.

Significant differences are also observed in the velocity fields. Since DES provides an unsteady solution, comparison with RANS is performed using both instantaneous fields and time averaged results. Velocity magnitude plots highlight the detailed development of vortical structures in DES in the instantaneous field, and also reveal how the DES mean field differs from the steady RANS field. Particularly in the wake region, the shape and extent of recirculation show noticeable deviations, which directly affect C_D and, more broadly, the overall aerodynamic behavior of the vehicle Fig. 3.21.

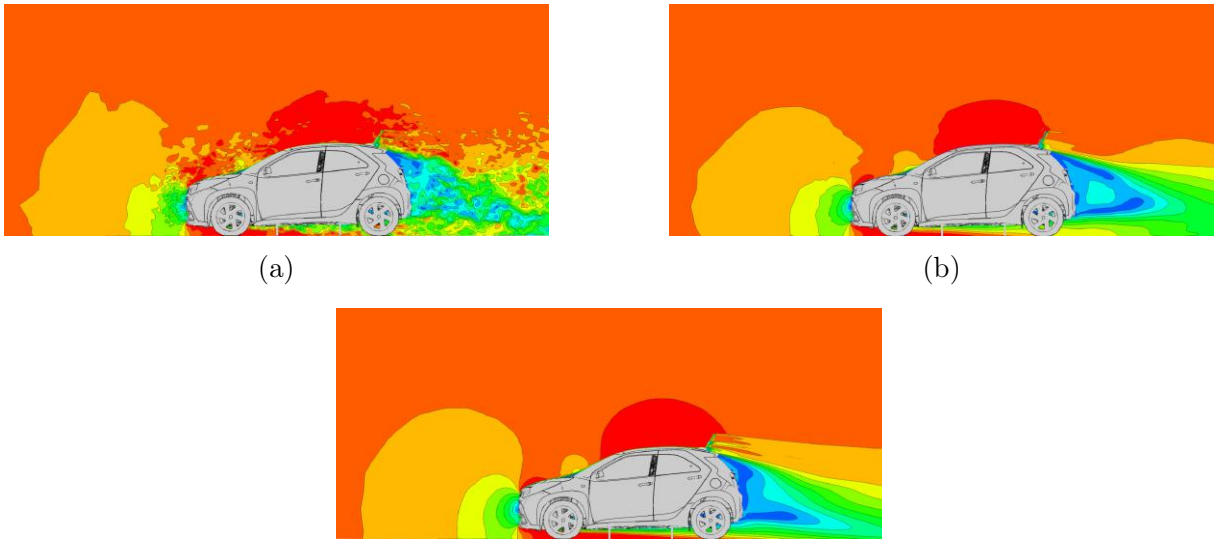

(a) (b)

(c)

Figure 3.21: Case C: Velocity magnitude field: (a) instantaneous DES at $t = 5$ s, (b) time-averaged DES, (c) RANS.

The differences between the two solutions are also evident on the $X\Upsilon$ plane, particularly at elevations where RANS predicts predominantly attached flow while DES indicates separation Fig. 3.22. Overall, RANS shows a consistent tendency to delay or suppress separation in regions where DES captures detached flow. Consequently, the predicted wake topology differs between the two approaches, including a noticeable shift in the position of the recirculation centre relative to the DES result.

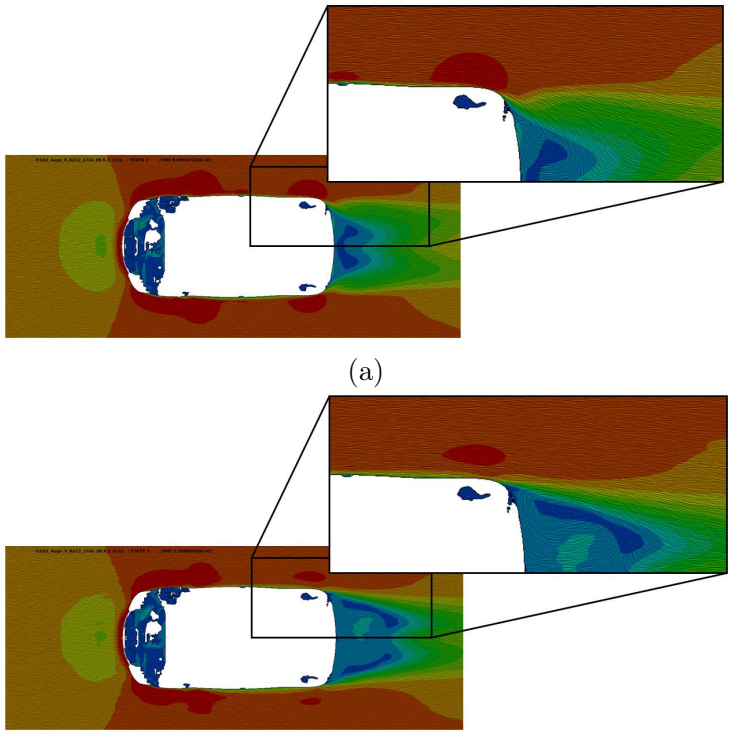

(a)

(b)

Figure 3.22: Case C: Velocity vector field on the x–z plane for (a) RANS and (b) DES.

Velocity magnitude plots on the YZ plane are also particularly informative, since they allow the wake structure to be visualized at several downstream stations. In the RANS case Fig. 3.23, a typical pair of contra rotating vortices is observed, which shift and evolve as the flow moves downstream. Their displacement towards the ground further downstream indicates wake interaction with the ground plane and the 3D development of the flow behind the vehicle.

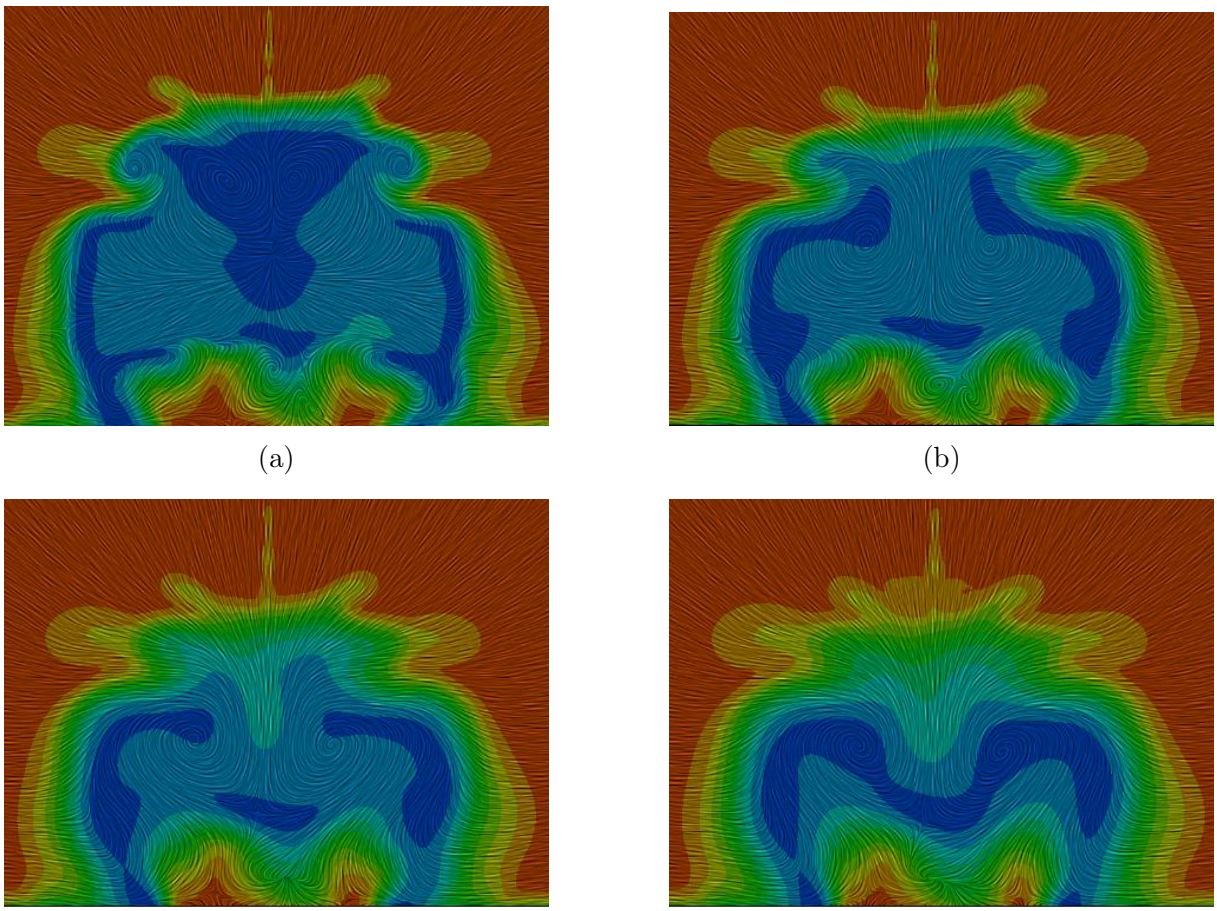

(a) (b)

(c) (d)

Figure 3.23: Case C: Velocity vector field on y–z sections downstream of the vehicle for the RANS simulation (a–d), from the near wake to farther downstream locations behind the rear of the vehicle.

In contrast, in DES Fig. 3.23, due to the non steady nature of the solution and the partial resolution of large scale vortical structures, the picture changes. More intense and more fragmented structures are observed, typically with a smaller overall extent, while merging and splitting are often visible due to stronger mixing. This behaviour is consistent with a more realistic representation of the wake, where large eddies evolve and interact dynamically, affecting the location, intensity, and extent of recirculation.

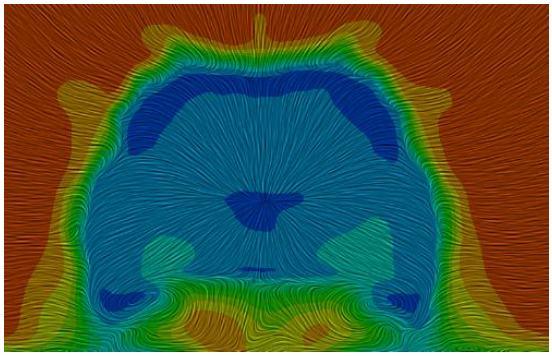

(a)

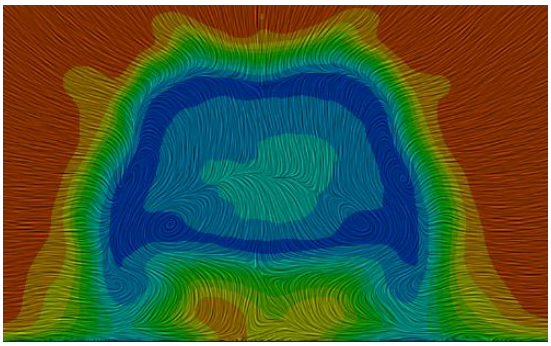

(b)

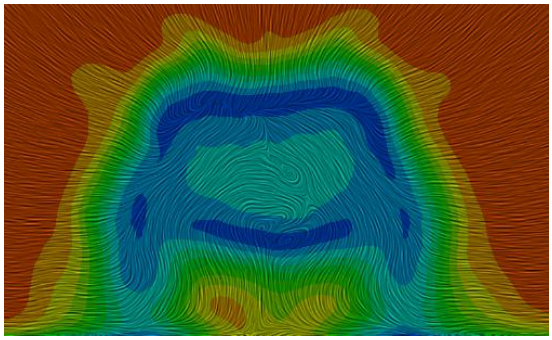

(c)

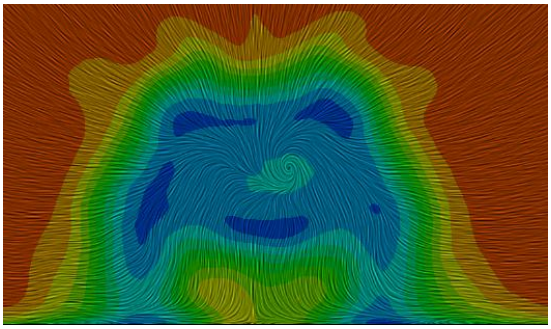

(d)

Figure 3.24: Case C: Velocity vector field on y–z sections downstream of the vehicle for the DES simulation (a–d), from the near wake to farther downstream locations behind the rear of the vehicle.

Finally, in this case as well, the turbulent-viscosity field ν_t Fig. 3.26 obtained with DES differs markedly from the corresponding RANS result, both in terms of spatial distribution and in the overall magnitude. In particular, the peak ν_t predicted by RANS is one order of magnitude higher than the maximum value in the time-averaged DES field, as well as in the representative instantaneous DES snapshots. Beyond the difference in peak levels, the topology of the ν_t field is also noticeably different between the two approaches, which is consistent with the fundamentally different way turbulence is represented in RANS and DES. These observations underline how strongly ν_t depends on the chosen turbulence-modelling approach and, consequently, how this choice can influence the final converged outcome of the overall problem.

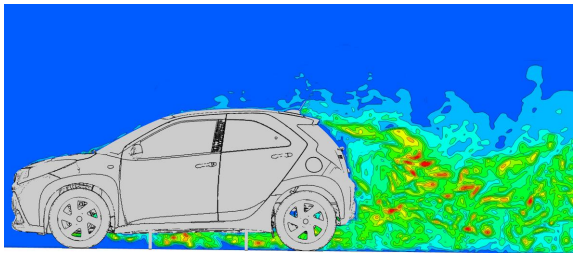

(a)

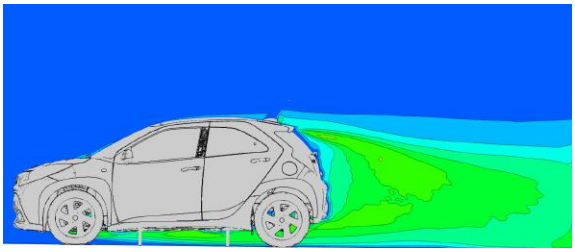

(b)

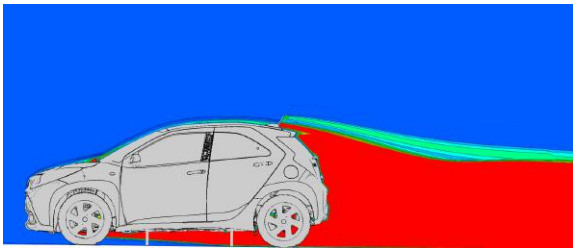

(c)

Figure 3.26: Case C: ν_t field for (a) instantaneous DES at $t = 5$ s, (b) time-averaged DES, and (c) RANS.

Chapter 4
Turbulence Model Adaptation

4.1 Eddy Viscosity Adaptation

As shown by the results of the previous section, the choice of turbulence model can lead to substantial differences in the predicted flow field and quantities of interest, in some cases even resulting in conflicting conclusions. For this reason, in recent years there has been an increasingly strong need for turbulence models that combine the accuracy of higher-fidelity approaches, such as DES or LES, with the lower computational cost of simpler models, such as RANS. Within this context, a method that has gained increasing popularity in recent years is known as Field Inversion, which aims to bridge the gap between low-fidelity RANS predictions and higher-fidelity reference data, such as DES, LES, or experiments.

The key idea behind this technique is that the turbulence fields predicted by RANS and DES can differ substantially, both in their structure and in their magnitude. This naturally raises the question of whether a corrective term or a correction factor can be introduced, or even determine ν_t directly at each mesh point, so that the turbulence model, and consequently the predicted flow, can be adjusted appropriately, achieving DES-comparable accuracy without the corresponding increase in computational cost. In this sense, the objective is to construct a spatially varying corrective field that modifies the model response in a consistent way across the computational domain.

In practice, the TMA problem is formulated as an optimization problem, since the goal is to minimise the discrepancy in a chosen quantity of interest of the flow field (for example velocity, pressure, skin friction, drag coefficient, and so on) between the RANS solution and the reference data. This is expressed through an objective function of the form:

$$J = \frac{1}{2} \int_{\Omega} \left(Q_{\mathrm{RANS}} - \bar{Q}_{\mathrm{ref}} \right)^2 \, \mathrm{d}\Omega, \tag{4.1}$$

where Q denotes the selected quantity of interest, and $\bar{Q}_{\mathrm{ref}}$ represents the corresponding reference field (e.g. time-averaged DES or LES, or experimental data).

It is worth noting that, in this optimization setting, the number of optimization variables typically coincides with the number of cells in the computational mesh. This means that, even for relatively simple 2D problems, the optimization may involve several tens of thousands of variables, whereas in industrial-scale applications the

number can reach, or even exceed, tens of millions. Therefore, it becomes immediately clear that the only practically feasible optimization approach for such problems is the adjoint method, which enables the computation of sensitivities at a computational cost that is essentially independent of the number of optimization.

Although there are various methods in the literature that develop the TMA idea, in this thesis, the Eddy Viscosity Adaptation (EVA) method will be developed. In this method, the optimization variables will be the turbulence viscosity, and the code will be adjoint-based for turbulence closure. Depending on the set objective, the corresponding adjoint problem will be formulated. The logic behind this approach is to focus on a target field (specifically, the mean velocity field of the DES).

Regarding the initialization of ν_t, in principle, it would be possible to start from a uniform field and allow the optimization procedure to converge from scratch. However, to reduce the computational cost, the ν_t field obtained from the RANS solution was selected as the initial condition. Tests were also performed using the ν_t fields obtained from the corresponding DES, but these fields were not derived from mathematical equations and do not directly satisfy the flow equations. As a result, when these fields were used as the initial condition, the system failed to reach satisfactory convergence levels and eventually diverged (the tests were conducted on Case A & B).

For this reason, initializing from RANS places the optimization at a more realistic starting point, which ensured satisfactory convergence and results. To develop the appropriate solver for this methodology within the OpenFOAM computational tool, the adjoint problem needs to be thoroughly analyzed to ensure its correct formulation and implementation.

4.2 Adjoint formulation of EVA

In this section, the optimization problem is formulated for the case where the target is a velocity field. The goal is to determine the field ν_t in the RANS model, so that a target field (e.g. the velocity field v_i) approximates as closely as possible the reference mean field $\overline{v}_i$, which has been obtained from the DES. This process is formulated as a minimization problem with an objective function:

$$J = \frac{1}{2} \int_{\Omega} \left(v_{RANS} - \overline{v}_{DES} \right)^2 d\Omega \tag{4.2}$$

The objective is to determine the turbulent viscosity field ν_t that minimizes the cost function J ($\min J(v, \nu_t)$). This leads to the definition of an optimization problem in which the control variable is the spatially distributed field ν_t. The solution of the problem is carried out using the adjoint method [33], since the number of design variables (i.e., the values of ν_t) is equal to the number of computational cells. The main advantage of the adjoint method is that it computes the gradient $\frac{\delta J}{\delta \nu_t}$ with a computational cost that is independent of the number of optimization variables, which here are as many as the mesh cells.

The governing equations for steady, incompressible mean flows are the Reynolds-Averaged Navier–Stokes (RANS) equations. These consist of the momentum equations and the

continuity equation, which are expressed as follows:

$$R^p = -\frac{\partial v_j}{\partial x_j} = 0 \tag{4.3a}$$

$$R_i^v = v_j \frac{\partial v_i}{\partial x_j} - \frac{\partial}{\partial x_j}\left[(\nu + \nu_t)\left(\frac{\partial v_i}{\partial x_j} + \frac{\partial v_j}{\partial x_i}\right)\right] + \frac{\partial p}{\partial x_i} = 0 \tag{4.3b}$$

The starting point for the formulation of the adjoint problem is the introduction of the augmented functional F_{aug}, which is defined as follows:

$$F_{\text{aug}} = J + \int_\Omega u_i R_i^v d\Omega + \int_\Omega q R^p d\Omega \tag{4.4}$$

where R_i^v denotes the momentum equations, R^p the continuity equation, u_i the adjoint velocity components, q denotes the adjoint pressure, and Ω is the computational domain.

The augmented functional is differentiated with respect to the control field ν_t, and is thus expressed as:

$$\begin{aligned} \frac{\delta F_{\text{aug}}}{\delta \nu_t} &= \frac{\delta J}{\delta \nu_t} + \frac{\delta}{\delta \nu_t}\int_\Omega u_i R_i^v d\Omega + \frac{\delta}{\delta \nu_t}\int_\Omega q R^p d\Omega \\ \frac{\delta F_{\text{aug}}}{\delta \nu_t} &\overset{\Rightarrow}{=} \frac{\delta J}{\delta \nu_t} + \int_\Omega u_i \frac{\delta R_i^v}{\delta \nu_t} d\Omega + \int_\Omega q \frac{\delta R^p}{\delta \nu_t} d\Omega \end{aligned} \tag{4.5}$$

Useful Mathematical Relationships

The following mathematical development is based on the total (or material) derivative of an arbitrary quantity $\phi = \Phi(b, x(b))$ with respect to a set of design variables b_n, with $n \in [1, N]$. This derivative, denoted by $\frac{\delta \Phi}{\delta b_n}$, accounts for the total variation in Φ due to changes in b_n, as expressed by the relation:

$$\frac{\delta \Phi}{\delta b_n} = \frac{\partial \Phi}{\partial b_n} + \frac{\partial \Phi}{\partial x_k}\frac{\delta x_k}{\delta b_n} \tag{4.6}$$

The term $\frac{\delta x_k}{\delta b_n}$ represents the total derivative of the spatial coordinate x_k (i.e., the position of a point in space) with respect to an optimization variable b_n. In our problem, the optimization variables is the ν_t field. Therefore, the last term on the right-hand side of Eq. (4.6) is independent of ν_t, as changes in ν_t do not affect the geometry. It follows that:

$$\frac{\delta x_k}{\delta \nu_t} = 0 \tag{4.7}$$

So, throughout this work:

$$\frac{\delta \Phi}{\delta \nu_t} = \frac{\partial \Phi}{\partial \nu_t} \tag{4.8}$$

An additional useful relation which links the the spatial and total derivatives with respect to ν_t is given by:

$$\frac{\delta}{\delta \nu_t}\left(\frac{\partial \Phi}{\partial x_j}\right) = \frac{\partial}{\partial x_j}\left(\frac{\partial \Phi}{\partial \nu_t}\right) - \frac{\partial \Phi}{\partial x_k}\frac{\partial}{\partial x_j}\left(\frac{\delta x_k}{\delta \nu_t}\right) \tag{4.9}$$

Since $\frac{\delta x_k}{\delta \nu_t} = 0$, the following simplified expression holds:

$$\frac{\delta}{\delta \nu_t}\left(\frac{\partial \Phi}{\partial x_j}\right) = \frac{\partial}{\partial x_j}\left(\frac{\partial \Phi}{\partial \nu_t}\right) \tag{4.10}$$

Computation of the first term in Eq. (4.5)

The objective function is differentiated with respect to ν_t, using the chain rule to express the derivative as:

$$\frac{\delta J}{\delta \nu_t} = \frac{\partial J}{\partial v_i} \cdot \frac{\delta v_i}{\delta \nu_t} + \frac{\partial J}{\partial p} \cdot \frac{\delta p}{\delta \nu_t} \tag{4.11}$$

Given equation (4.8), the above expression can be rewritten as:

$$\frac{\delta J}{\delta \nu_t} = \int_\Omega \frac{\partial j}{\partial v_i}\frac{\delta v_i}{\delta \nu_t} d\Omega + \int_\Omega \frac{\partial j}{\partial p}\frac{\delta p}{\delta \nu_t} d\Omega \tag{4.12}$$

Computation of the second term in Eq. (4.5)

R_p is the residual of the continuity equation. Therefore:

$$\int_\Omega q \frac{\delta R_p}{\delta \nu_t} d\Omega = -\int_\Omega q \frac{\delta}{\delta \nu_t}\left(\frac{\partial v_j}{\partial x_j}\right) d\Omega \tag{4.13}$$

Based on equation (4.10) and by applying the Green–Gauss theorem:

$$\int_\Omega q \frac{\delta R_p}{\delta \nu_t} d\Omega = -\int_\Omega q \frac{\partial}{\partial x_j}\left(\frac{\partial v_j}{\partial \nu_t}\right) d\Omega \quad = -\int_S q \frac{\partial v_j}{\partial \nu_t} n_j dS + \int_\Omega \frac{\partial q}{\partial x_j}\frac{\partial v_j}{\partial \nu_t} d\Omega \tag{4.14}$$

Computation of the third term in Eq. (4.5)

R_i^v is the residual of the mean momentum equation. Therefore:

$$\frac{\delta R_i^v}{\delta \nu_t} = \frac{\delta}{\delta \nu_t}\left(v_j \frac{\partial v_i}{\partial x_j}\right) - \frac{\delta}{\delta \nu_t}\left[\frac{\partial}{\partial x_j}\left((\nu + \nu_t)\left(\frac{\partial v_i}{\partial x_j} + \frac{\partial v_j}{\partial x_i}\right)\right)\right] + \frac{\delta}{\delta \nu_t}\left(\frac{\partial p}{\partial x_i}\right) \tag{4.15}$$

Thus:

$$\begin{aligned}\int_\Omega u_i \frac{\partial R_i^v}{\partial \nu_t} d\Omega = &\underbrace{\int_\Omega u_i \frac{\delta}{\delta \nu_t}\left(v_j \frac{\partial v_i}{\partial x_j}\right) d\Omega}_{I} - \underbrace{\int_\Omega u_i \frac{\delta}{\delta \nu_t}\left[\frac{\partial}{\partial x_j}\left((\nu + \nu_t)\left(\frac{\partial v_i}{\partial x_j} + \frac{\partial v_j}{\partial x_i}\right)\right)\right] d\Omega}_{II} \\ &+ \underbrace{\int_\Omega u_i \frac{\delta}{\delta \nu_t}\left(\frac{\partial p}{\partial x_i}\right) d\Omega}_{III}\end{aligned} \tag{4.16}$$

Terms I, II, and III are further analyzed as :

$$
\begin{aligned}
I &= \int_\Omega u_i \frac{\delta}{\delta \nu_t}\left(v_j \frac{\partial v_i}{\partial x_j}\right) d\Omega = \int_\Omega u_i \left(\frac{\delta v_j}{\delta \nu_t}\frac{\partial v_i}{\partial x_j} + v_j \frac{\delta}{\delta \nu_t}\left(\frac{\partial v_i}{\partial x_j}\right)\right) d\Omega \\
&= \int_\Omega u_i \frac{\partial v_j}{\partial \nu_t}\frac{\partial v_i}{\partial x_j}\, d\Omega + \int_\Omega u_i v_j \frac{\delta}{\delta \nu_t}\left(\frac{\partial v_i}{\partial x_j}\right) d\Omega \\
&= \int_\Omega u_i \frac{\partial v_j}{\partial \nu_t}\frac{\partial v_i}{\partial x_j}\, d\Omega + \int_\Omega u_i v_j \frac{\partial}{\partial x_j}\left(\frac{\partial v_i}{\partial \nu_t}\right) d\Omega \\
&= \int_\Omega u_i \frac{\partial v_j}{\partial \nu_t}\frac{\partial v_i}{\partial x_j}\, d\Omega + \int_S u_i v_j n_j \frac{\partial v_i}{\partial \nu_t}\, dS - \int_\Omega \frac{\partial (u_i v_j)}{\partial x_j}\frac{\partial v_i}{\partial \nu_t}\, d\Omega
\end{aligned}
\tag{4.17}
$$

$$
\begin{aligned}
II &= -\int_\Omega u_i \frac{\delta}{\delta \nu_t}\left[\frac{\partial}{\partial x_j}\left((\nu+\nu_t)\left(\frac{\partial v_i}{\partial x_j}+\frac{\partial v_j}{\partial x_i}\right)\right)\right] d\Omega \\
&\overset{(4.10)}{=} -\int_\Omega u_i \frac{\partial}{\partial x_j}\left[\frac{\partial}{\partial \nu_t}\left((\nu+\nu_t)\left(\frac{\partial v_i}{\partial x_j}+\frac{\partial v_j}{\partial x_i}\right)\right)\right] d\Omega \\
&= -\int_S u_i n_j \left[\frac{\partial}{\partial \nu_t}\left((\nu+\nu_t)\left(\frac{\partial v_i}{\partial x_j}+\frac{\partial v_j}{\partial x_i}\right)\right)\right] dS + \int_\Omega \frac{\partial u_i}{\partial x_j}\left[\frac{\partial}{\partial \nu_t}\left((\nu+\nu_t)\left(\frac{\partial v_i}{\partial x_j}+\frac{\partial v_j}{\partial x_i}\right)\right)\right] d\Omega \\
&= -\int_S u_i n_j \left[\frac{\partial}{\partial \nu_t}\left((\nu+\nu_t)\left(\frac{\partial v_i}{\partial x_j}+\frac{\partial v_j}{\partial x_i}\right)\right)\right] dS + \int_\Omega \frac{\partial u_i}{\partial x_j}\frac{\delta \nu_t}{\delta \nu_{t,P}}\left(\frac{\partial v_i}{\partial x_j}+\frac{\partial v_j}{\partial x_i}\right) d\Omega \\
&\quad + \int_\Omega (\nu+\nu_t)\frac{\partial u_i}{\partial x_j}\frac{\partial}{\partial \nu_t}\left(\frac{\partial v_i}{\partial x_j}+\frac{\partial v_j}{\partial x_i}\right) d\Omega \\
&= -\int_S u_i n_j \left[\frac{\partial}{\partial \nu_t}\left((\nu+\nu_t)\left(\frac{\partial v_i}{\partial x_j}+\frac{\partial v_j}{\partial x_i}\right)\right)\right] dS + \int_\Omega \frac{\partial u_i}{\partial x_j}\frac{\delta \nu_t}{\delta \nu_{t,P}}\left(\frac{\partial v_i}{\partial x_j}+\frac{\partial v_j}{\partial x_i}\right) d\Omega \\
&\quad + \int_\Omega (\nu+\nu_t)\frac{\partial u_i}{\partial x_j}\frac{\partial}{\partial \nu_t}\left(\frac{\partial v_i}{\partial x_j}\right) d\Omega + \int_\Omega (\nu+\nu_t)\frac{\partial u_i}{\partial x_j}\frac{\partial}{\partial \nu_t}\left(\frac{\partial v_j}{\partial x_i}\right) d\Omega \\
&= -\int_S u_i n_j \left[\frac{\partial}{\partial \nu_t}\left((\nu+\nu_t)\left(\frac{\partial v_i}{\partial x_j}+\frac{\partial v_j}{\partial x_i}\right)\right)\right] dS + \int_\Omega \frac{\partial u_i}{\partial x_j}\frac{\delta \nu_t}{\delta \nu_{t,P}}\left(\frac{\partial v_i}{\partial x_j}+\frac{\partial v_j}{\partial x_i}\right) d\Omega \\
&\quad + \int_\Omega (\nu+\nu_t)\frac{\partial u_i}{\partial x_j}\frac{\partial}{\partial x_j}\left(\frac{\partial v_i}{\partial \nu_t}\right) d\Omega + \int_\Omega (\nu+\nu_t)\frac{\partial u_i}{\partial x_j}\frac{\partial}{\partial x_i}\left(\frac{\partial v_j}{\partial \nu_t}\right) d\Omega
\end{aligned}
\tag{4.18}
$$

The two volume integral terms on the right-hand side of equation (4.18) are further analyzed as follows:

$$
\int_\Omega (\nu+\nu_t)\frac{\partial u_i}{\partial x_j}\frac{\partial}{\partial x_j}\left(\frac{\partial v_i}{\partial \nu_t}\right) d\Omega = \int_S (\nu+\nu_t)\frac{\partial u_i}{\partial x_j}\frac{\partial v_i}{\partial \nu_t} n_j dS - \int_\Omega \frac{\partial}{\partial x_j}\left[(\nu+\nu_t)\frac{\partial u_i}{\partial x_j}\right]\frac{\partial v_i}{\partial \nu_t} d\Omega \tag{4.19}
$$

$$
\begin{aligned}
\int_\Omega (\nu+\nu_t)\frac{\partial u_i}{\partial x_j}\frac{\partial}{\partial x_i}\left(\frac{\partial v_j}{\partial \nu_t}\right) d\Omega &= \int_S (\nu+\nu_t)\frac{\partial u_i}{\partial x_j}\frac{\partial v_j}{\partial \nu_t} n_i dS - \int_\Omega \frac{\partial}{\partial x_i}\left[(\nu+\nu_t)\frac{\partial u_i}{\partial x_j}\right]\frac{\partial v_j}{\partial \nu_t} d\Omega \\
&= \int_S (\nu+\nu_t)\frac{\partial u_j}{\partial x_i}\frac{\partial v_i}{\partial \nu_t} n_j dS - \int_\Omega \frac{\partial}{\partial x_j}\left[(\nu+\nu_t)\frac{\partial u_j}{\partial x_i}\right]\frac{\partial v_i}{\partial \nu_t} d\Omega
\end{aligned}
\tag{4.20}
$$

Thus, the final expression becomes:

$$
\begin{aligned}
II = & -\int_S u_i n_j \left[\frac{\partial}{\partial \nu_t}\left((\nu+\nu_t)\left(\frac{\partial v_i}{\partial x_j}+\frac{\partial v_j}{\partial x_i}\right)\right)\right] dS \\
& + \int_\Omega \frac{\partial u_i}{\partial x_j}\frac{\delta \nu_t}{\delta \nu_{t,P}}\left(\frac{\partial v_i}{\partial x_j}+\frac{\partial v_j}{\partial x_i}\right) d\Omega \\
& + \int_S (\nu+\nu_t)\frac{\partial u_i}{\partial x_j}\frac{\partial v_i}{\partial \nu_t} n_j dS - \int_\Omega \frac{\partial}{\partial x_j}\left[(\nu+\nu_t)\frac{\partial u_i}{\partial x_j}\right]\frac{\partial v_i}{\partial \nu_t} d\Omega \\
& + \int_S (\nu+\nu_t)\frac{\partial u_j}{\partial x_i}\frac{\partial v_i}{\partial \nu_t} n_j dS - \int_\Omega \frac{\partial}{\partial x_j}\left[(\nu+\nu_t)\frac{\partial u_j}{\partial x_i}\right]\frac{\partial v_i}{\partial \nu_t} d\Omega \\
= & -\int_S u_i n_j \left[\frac{\partial}{\partial \nu_t}\left((\nu+\nu_t)\left(\frac{\partial v_i}{\partial x_j}+\frac{\partial v_j}{\partial x_i}\right)\right)\right] dS \\
& + \int_\Omega \frac{\partial u_i}{\partial x_j}\frac{\delta \nu_t}{\delta \nu_{t,P}}\left(\frac{\partial v_i}{\partial x_j}+\frac{\partial v_j}{\partial x_i}\right) d\Omega \\
& + \int_S (\nu+\nu_t)\left(\frac{\partial u_i}{\partial x_j}+\frac{\partial u_j}{\partial x_i}\right) n_j \frac{\partial v_i}{\partial \nu_t} dS \\
& - \int_\Omega (\nu+\nu_t)\frac{\partial}{\partial x_j}\left[\frac{\partial u_i}{\partial x_j}+\frac{\partial u_j}{\partial x_i}\right]\frac{\partial v_i}{\partial \nu_t} d\Omega
\end{aligned}
\tag{4.21}
$$

Term $\delta_{\nu_t,P}$ is essentially a discrete Kronecker-type delta applied at cell P: it takes the value 1 when ν_t refers to the same cell P and 0 for all other cells, so within the integral it isolates the contribution of cell P.

$$
\begin{aligned}
III &= \int_\Omega u_i \frac{\delta}{\delta \nu_t}\left(\frac{\partial p}{\partial x_i}\right) d\Omega = \int_\Omega u_i \frac{\partial}{\partial x_i}\left(\frac{\partial p}{\partial \nu_t}\right) d\Omega \\
&= \int_S u_i n_i \frac{\partial p}{\partial \nu_t} dS - \int_\Omega \frac{\partial u_i}{\partial x_i}\frac{\partial p}{\partial \nu_t} d\Omega
\end{aligned}
\tag{4.22}
$$

Based on the above equations, the expression for $\frac{\delta F_{\text{aug}}}{\delta \nu_t}$, becomes:

$$
\begin{aligned}
\frac{\delta F_{\text{aug}}}{\delta \nu_t} = & \int_\Omega \frac{\partial j}{\partial v_i}\frac{\partial v_i}{\partial \nu_t} d\Omega + \int_\Omega \frac{\partial j}{\partial p}\frac{\partial p}{\partial \nu_t} d\Omega - \int_S q \frac{\partial v_j}{\partial \nu_t} n_j dS + \int_\Omega \frac{\partial q}{\partial x_j}\frac{\partial v_j}{\partial \nu_t} d\Omega \\
& + \int_\Omega u_i \frac{\partial v_j}{\partial \nu_t}\cdot\frac{\partial v_i}{\partial x_j} d\Omega + \int_S u_i v_j n_j \frac{\partial v_i}{\partial \nu_t} dS - \int_\Omega \frac{\partial\left(u_i v_j\right)}{\partial x_j}\frac{\partial v_i}{\partial \nu_t} d\Omega \\
& - \int_S u_i n_j \left[\frac{\partial}{\partial \nu_t}\left((\nu+\nu_t)\left(\frac{\partial v_i}{\partial x_j}+\frac{\partial v_j}{\partial x_i}\right)\right)\right] dS + \int_\Omega \frac{\partial u_i}{\partial x_j}\frac{\delta \nu_t}{\delta \nu_{t,P}}\left(\frac{\partial v_i}{\partial x_j}+\frac{\partial v_j}{\partial x_i}\right) d\Omega \\
& + \int_S (\nu+\nu_t)\left(\frac{\partial u_i}{\partial x_j}+\frac{\partial u_j}{\partial x_i}\right) n_j \frac{\partial v_i}{\partial \nu_t} dS - \int_\Omega (\nu+\nu_t)\frac{\partial}{\partial x_j}\left[\frac{\partial u_i}{\partial x_j}+\frac{\partial u_j}{\partial x_i}\right]\frac{\partial v_i}{\partial \nu_t} d\Omega \\
& + \int_S u_i n_i \frac{\partial p}{\partial \nu_t} dS - \int_\Omega \frac{\partial u_i}{\partial x_i}\frac{\partial p}{\partial \nu_t} d\Omega
\end{aligned}
\tag{4.23}
$$

or :

$$
\begin{aligned}
\frac{\delta F_{\text{aug}}}{\delta \nu_t} = & \int_\Omega \left[\frac{\partial j}{\partial v_i} + \frac{\partial q}{\partial x_i} + u_j \frac{\partial v_j}{\partial x_i} - \frac{\partial \left(u_i v_j \right)}{\partial x_j} - \left(\nu + \nu_t \right) \frac{\partial}{\partial x_j} \left[\frac{\partial u_i}{\partial x_j} + \frac{\partial u_j}{\partial x_i} \right] \right] \frac{\partial v_i}{\partial \nu_t} d\Omega \\
& + \int_\Omega \left[\frac{\partial j}{\partial p} - \frac{\partial u_i}{\partial x_i} \right] \frac{\partial p}{\partial \nu_t} d\Omega \\
& + \int_\Omega \frac{\partial u_i}{\partial x_j} \frac{\delta \nu_t}{\delta \nu_{t,P}} \left(\frac{\partial v_i}{\partial x_j} + \frac{\partial v_j}{\partial x_i} \right) d\Omega \\
& + \int_S \left[-q n_i \ + u_i v_j n_j + \left(\nu + \nu_t \right) \left(\frac{\partial u_i}{\partial x_j} + \frac{\partial u_j}{\partial x_i} \right) n_{\ j} \right] \frac{\partial v_i}{\partial \nu_t} dS \\
& + \int_S u_i n_i \frac{\partial p}{\partial \nu_t} dS - \int_S u_i n_j \left[\frac{\partial}{\partial \nu_t} \left(\left(\nu + \nu_t \right) \left(\frac{\partial v_i}{\partial x_j} + \frac{\partial v_j}{\partial x_i} \right) \right) \right] dS
\end{aligned}
\tag{4.24}
$$

To avoid computing the derivatives with respect to the flow variables in equation (4.24), their multipliers are set to zero, leading to the Field Adjoint Equations (FAE), which are expressed in the following form of continuous PDEs:

$$
R^p = \frac{\partial j}{\partial p} - \frac{\partial u_i}{\partial x_i} = 0 \tag{4.25}
$$

$$
R_i^u = \frac{\partial j}{\partial v_i} + \frac{\partial q}{\partial x_i} + u_j \frac{\partial v_j}{\partial x_i} - \frac{\partial \left(u_i v_j \right)}{\partial x_j} - \left(\nu + \nu_t \right) \frac{\partial}{\partial x_j} \left[\frac{\partial u_i}{\partial x_j} + \frac{\partial u_j}{\partial x_i} \right] = 0 \tag{4.26}
$$

Taking the definition of the objective function (4.2), into account it holds that:

$$
\frac{\partial j}{\partial p} = 0 \quad \& \quad \frac{\partial j}{\partial v_i} = v_i - \overline{v}_i \tag{4.27}
$$

Therefore, equations (4.25) & (4.26) can be written as:

$$
R^p = -\frac{\partial u_i}{\partial x_i} = 0 \tag{4.28}
$$

$$
R_i^u = \left(v_{RANS} - \overline{v}_{DES} \right) + \frac{\partial q}{\partial x_i} + u_j \frac{\partial v_j}{\partial x_i} - \frac{\partial \left(u_i v_j \right)}{\partial x_j} - \left(\nu + \nu_t \right) \frac{\partial}{\partial x_j} \left[\frac{\partial u_i}{\partial x_j} + \frac{\partial u_j}{\partial x_i} \right] = 0 \tag{4.29}
$$

Once the field adjoint equations are satisfied, the remaining terms in equation (4.24) are expressed as:

$$
\begin{aligned}
\frac{\delta F_{\text{aug}}}{\delta \nu_t} = & + \int_\Omega \frac{\partial u_i}{\partial x_j} \frac{\delta \nu_t}{\delta \nu_{t,P}} \left(\frac{\partial v_i}{\partial x_j} + \frac{\partial v_j}{\partial x_i} \right) d\Omega \\
& + \int_S \left[-q n_i \ + u_i v_j n_j + \left(\nu + \nu_t \right) \left(\frac{\partial u_i}{\partial x_j} + \frac{\partial u_j}{\partial x_i} \right) n_{\ j} \right] \frac{\partial v_i}{\partial \nu_t} dS + \int_S u_i n_i \frac{\partial p}{\partial \nu_t} dS \\
& - \int_S u_i n_j \left[\frac{\partial}{\partial \nu_t} \left(\left(\nu + \nu_t \right) \left(\frac{\partial v_i}{\partial x_j} + \frac{\partial v_j}{\partial x_i} \right) \right) \right] dS
\end{aligned}
\tag{4.30}
$$

Once the adjoint field equations (FAE) have been formulated, the boundary conditions of the primal problem are applied in order to derive the corresponding boundary conditions for the adjoint. This leads to the final form of the sensitivity derivatives, which is presented in the next section.

Inlet

At the inlet patches (S_I), Dirichlet conditions are imposed on the velocity components and a Neumann zero-gradient condition on the pressure. The inlet velocity is independent of ν_t, therefore:

$$\frac{\partial v_i}{\partial \nu_t} = 0 \tag{4.31}$$

For the elimination of the second and third surface terms of equation (4.30), instead of working in a simple Cartesian coordinate system (x, y, z), is used the local orthogonal Frenet system, which is defined by the vectors n, t^I, t^{II}. In this framework, the adjoint velocity vector is decomposed into one normal and two tangential components:

$$u = u_{(n)}n + u^I_{(t)}t^I + u^{II}_{(t)}t^{II} \tag{4.32}$$

The quantities $u^I_{(t)}$ and $u^{II}_{(t)}$ correspond to the components of the adjoint velocity along the directions t^I and t^{II}, respectively. The first tangential vector t^I can be defined as any unit vector parallel to the inlet boundary (S_I), while the second arises from the relation

$$t^{II}_i = \varepsilon_{ijk} n_j t^I_k \tag{4.33}$$

where ε_{ijk} is the permutation symbol Levi–Civita.

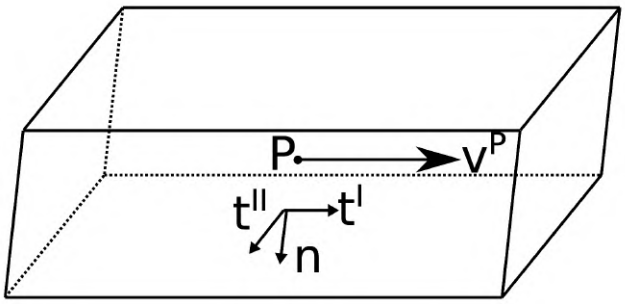

Figure 4.1: Typical finite-volume cell adjacent to a solid wall. Vector n denotes the outward unit normal, t^I is aligned with the velocity vector at the first cell center P, and $t^{II}_i = \varepsilon_{ijk}\, n_j\, t^I_k$ defines the second tangential direction, from [34].

The two tangential components in the directions t^I and t^{II} acquire physical meaning only in combination with the normal direction, as they are always defined with respect to the normal vector n. Assuming that the normal direction corresponds to axis $i = 3$, , the following is obtained:

$$\begin{gathered} u_i n_i = 0 \\ \Rightarrow \quad u_1 n_3 = 0, \quad u_2 n_3 = 0, \quad u_3 n_3 = 0 \end{gathered} \tag{4.34}$$

The inlet boundary conditions, expressed in the local orthogonal system, are then written concisely as:

$$u_{(n)} = 0, \qquad u^I_{(t)} = 0, \qquad u^{II}_{(t)} = 0 \tag{4.35}$$

Finally, and without resulting from the above eliminations, a zero Neumann condition is imposed on the adjoint pressure q at the inlet:

$$\frac{\partial q}{\partial x_j} n_j = 0 \tag{4.36}$$

Solid Wall

Over the solid walls (S_w) a constant velocity is imposed, which for stationary walls is zero. In the primal solver, Dirichlet conditions are applied to the velocity components and a Neumann zero-gradient condition to the pressure. Thus, for the velocity:

$$\frac{\partial v_i}{\partial \nu_t} = 0 \tag{4.37}$$

For the elimination of the second and third surface terms of equation (3.25), the same procedure as for the inlet boundaries is applied. As a result, the boundary conditions at the wall are defined as:

$$u_i n_i = u_{(n)} = 0, \qquad u^I_{(t)} = 0, \qquad u^{II}_{(t)} = 0 \tag{4.38}$$

Finally, and without resulting from the above eliminations, a zero Neumann condition is imposed for the adjoint pressure q at the inlets of the integration domain:

$$\frac{\partial q}{\partial x_j} n_j = 0 \tag{4.39}$$

Outlet

At the outlet patches (S_O), a Dirichlet boundary condition is imposed on p and a Neumann zero-gradient condition on the velocity components. Thus, for p:

$$\frac{\partial p}{\partial \nu_t} = 0 \tag{4.40}$$

Due to the large distance of the outlet boundary from the controlled region, the velocity profile along S_O can be assumed to be almost uniform. Thus:

$$\frac{\partial v_i}{\partial x_j} = \frac{\partial v_j}{\partial x_i} = 0 \tag{4.41}$$

To eliminate the first surface integral in equation 3.25 , it is set to:

$$-q\, n_i + u_i v_j n_j + (\nu + \nu_t) \left(\frac{\partial u_i}{\partial x_j} + \frac{\partial u_j}{\partial x_i} \right) n_j = 0 \tag{4.42}$$

Expressing the relation for $i = 1, 2, 3$ yields:

$$\begin{aligned} u_1 v_3 n_3 + (\nu + \nu_t)\left(\frac{\partial u_1}{\partial x_3} + \frac{\partial u_3}{\partial x_1}\right) n_3 = 0, \\ u_2 v_3 n_3 + (\nu + \nu_t)\left(\frac{\partial u_2}{\partial x_3} + \frac{\partial u_3}{\partial x_2}\right) n_3 = 0, \\ -q n_3 + u_3 v_3 n_3 + (\nu + \nu_t)\left(\frac{\partial u_3}{\partial x_3} + \frac{\partial u_3}{\partial x_3}\right) n_3 = 0 \end{aligned} \tag{4.43}$$

Projecting the above relations onto the directions of the local orthogonal Frenet system (n, t^I, t^{II}), the boundary conditions are obtained. Multiplication by the normal vector n leads to the relation for the adjoint pressure at the outlet boundary:

$$q \ = u_{(n)} v_{(n)} + 2\,(\nu + \nu_t)\,\frac{\partial u_{(n)}}{\partial n} \tag{4.44}$$

while the tangential components of the adjoint velocity $u^I_{(t)}$ are obtained by multiplying with the tangential t^l_i $(l = 1, 2)$:

$$v_{(n)}\ u^l_{(t)} + (\nu + \nu_t)\left(\frac{\partial\ u^l_{(t)}}{\partial n} + \frac{\partial u_{(n)}}{\partial\ t^l}\right) = 0 \tag{4.45}$$

The above relations show that the tangential components of the adjoint velocity satisfy mixed or Robin-type conditions.

Sensitivity Derivatives

Once the FAE and their corresponding boundary conditions are satisfied, the expression for the sensitivity derivatives, takes the form:

$$\frac{\delta F_{\text{aug}}}{\delta \nu_t} = \frac{\partial u_i}{\partial x_j}\left(\frac{\partial v_i}{\partial x_j} + \frac{\partial v_j}{\partial x_i}\right)\Delta\Omega \tag{4.46}$$

4.3 Finite Differences (FD)

To verify the validity of both the code and the governing equations implemented, it is advisable to validate the sensitivity derivatives by comparing them with results obtained from an independent numerical method. For this purpose, the Finite Differences (FD) method was selected. Although it is mathematically and programmatically straightforward, it can present significant challenges in applications such as the present one. In what follows, the forward FD scheme is used. For an objective function F and the design variable b_n, the derivative is approximated as:

$$\frac{\delta F}{\delta b_n} = \frac{F(b_1, b_2, \ldots, b_n + \epsilon, \ldots, b_{N-1}, b_N) - F(b_1, b_2, \ldots, b_n, \ldots, b_{N-1}, b_N)}{\epsilon}. \tag{4.47}$$

Applying FD requires N additional evaluations of the objective function, where N is the number of design variables. This means that, to compute the derivative with respect to a single variable, a small perturbation ϵ must be applied to that design variable, and then a full simulation must be run again in order to obtain the new value of J. In our case, where the design variables correspond to values of the turbulent viscosity ν_t per mesh cell, the number of variables is effectively equal to the number of cells. Therefore, computing derivatives over the entire field would require $N = N_{\text{cells}}$ independent simulations. Even for a simple 2D application, N_{cells} can be on the order of tens of thousands, while for industrial applications (such as Case C) it may reach tens of millions. It is, therefore, evident that such a procedure is practically infeasible in terms of computational cost. This also highlights, in a very direct way, the importance of the adjoint method, which is essentially the only methodology that can address problems of this type, since its cost is independent of the number of design variables.

The derivatives computed with forward FD are defined as:

$$\left.\frac{\delta F}{\delta \nu_t}\right|_n = \frac{J(\nu_{t,0}, \nu_{t,1}, \ldots, \nu_{t,n} + \epsilon, \ldots, \nu_{t,N}) - J(\nu_{t,0}, \nu_{t,1}, \ldots, \nu_{t,n}, \ldots, \nu_{t,N})}{\epsilon}. \tag{4.48}$$

This test is applied to Case A and Case B, primarily due to computational cost considerations. For each case, a representative cell is selected in regions where the discrepancy between the RANS and DES solutions is largest; the corresponding selected locations are highlighted in red in Fig. 4.2a 4.2b.

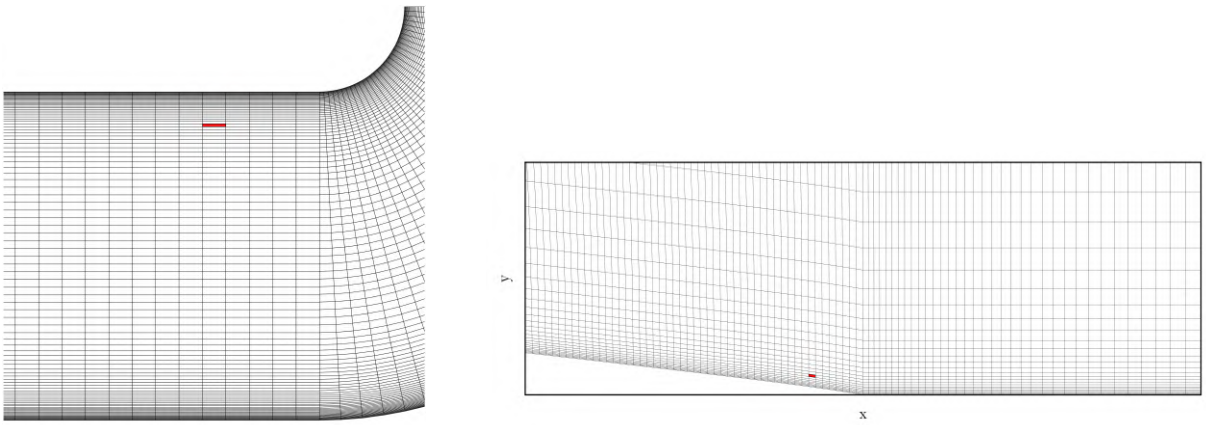

(a) (b)

Figure 4.2: FD sampling points used for the sensitivity evaluation: (a) Case A and (b) Case B. Red markers indicate the points where the ε perturbation was applied.

The resulting finite-difference sensitivities for Cases A and B are summarized in Tabs. 4.1 and 4.2, respectively.

Case A	
ϵ	$\left.\frac{\mathrm{d}J}{\mathrm{d}\nu_t}\right\|_n$
10^{-5}	-0.0001362
10^{-6}	-0.0001370
10^{-7}	-0.0001400

Table 4.1: Case A: FD sensitivities.

Case B	
ϵ	$\left.\frac{\mathrm{d}J}{\mathrm{d}\nu_t}\right\|_n$
10^{-5}	0.5351
10^{-6}	0.535
10^{-7}	0.53

Table 4.2: Case B: FD sensitivities.

The corresponding adjoint-based results (derived from the proposed formulation and implemented solver) are reported in Tab. 4.3, together with the corresponding FD values for comparison.

	Case A	**Case B**
Adjoint	-0.00013543	0.541662
FD	-0.0001400	0.53

Table 4.3: Case A and B: Comparison of sensitivity derivatives obtained with the adjoint method and FD.

It can be observed that the adjoint values are very close to those obtained from FD, which serves as strong evidence that both the theoretical formulation and the code implementation are correct. Consequently, the method can be used with confidence for further analysis and investigation.

Chapter 5
TMA Results

Once the verification test was successfully completed through a comparison of the sensitivity derivatives, an evaluation of our implementation can be performed across all three cases (Cases A, B, and C) discussed previously. The objective is to examine whether the EVA procedure can compute ν_t fields that reduce the discrepancy between the RANS solution and the time–averaged DES velocity field. The success of the methodology is reflected, on the one hand, on a reduction of the objective function and, on the other hand, on an improved agreement of key flow features, such as separation and the recirculation region. In this way, it can be assessed whether RANS, after being surrogated through EVA, begins to approach more closely the more detailed flow description provided by DES.

To update the values of the design variables at each optimization cycle, an update method is required. In the present work, two update algorithms available in the OpenFOAM optimization framework were employed: Steepest Descent and the Method of Moving Asymptotes (MMA).

5.1 Case A

For this case, MMA was selected as the update method, while upper and lower bounds were also imposed on the values that the ν_t field can take, in order to ensure physical consistency and numerical stability of the solution. More specifically, the upper bound was set to a value slightly higher than the maximum ν_t observed in the RANS and DES fields (typically using a small safety factor), so that sufficient optimization freedom is allowed without producing non physical extremes. The minimization loop of the EVA was performed over 20 cycles. Indicatively, the residuals of the final cycle are provided, corresponding to the last iteration Fig. 5.2.

Figure 5.1: Case A: Converge of the residuals of the primal and adjoint equations in the final EVA-minimixation cycle.

The convergence of the minimization problem of EVA is shown in the Fig. 5.2.

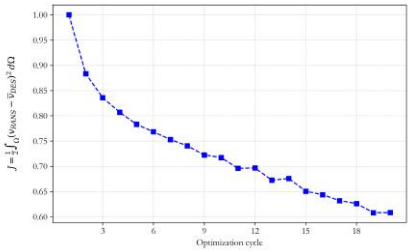

Figure 5.2: Case A: Convergence of the EVA minimization problem.

The largest reduction of the objective function occurs during the first cycles while the process is then gradually driven towards a stabilized regime. Towards the end of the minimization, the variation of J becomes negligible; indicatively, between iterations 19 and 20, J changed by only 0.02739%, which indicates satisfactory convergence.

Overall, J was reduced by approximately 40% compared to its initial value. This improvement is also reflected in the flow fields, as the overall differences between the velocity fields have been significantly reduced, which is confirmed through comparison of the corresponding distributions.

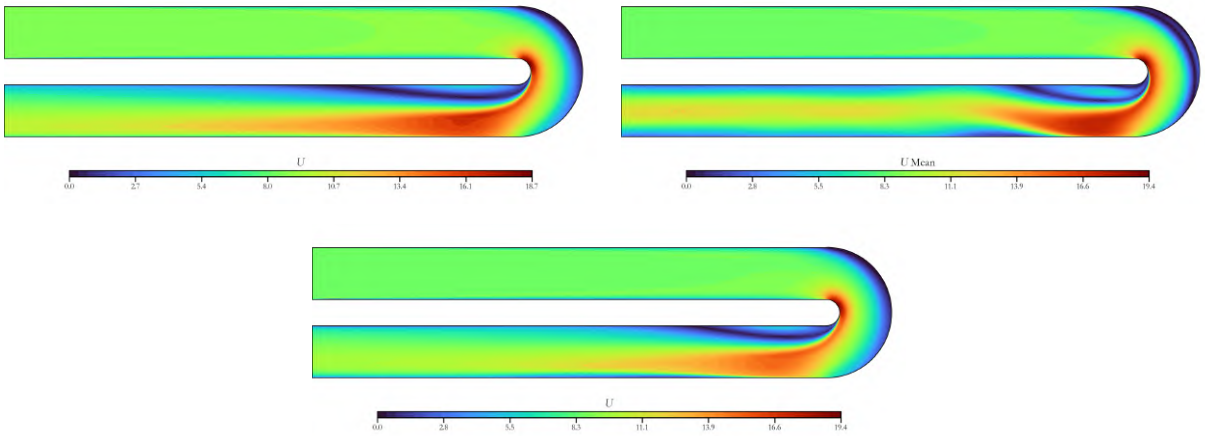

Figure 5.3: Case A: Velocity magnitude field for (a) RANS, (b) Time-averaged DES , and (c) EVA model.

As shown in Figs.5.3, the solution after EVA approaches the mean DES field clearly better than the original RANS prediction. The most important improvement is observed in the recirculation zone at the inner bend, where the baseline RANS exhibits an extended region of low velocities and strong momentum deficit. After EVA, this zone shrinks and the velocity distribution becomes closer to the morphology of U_{mean} (DES), indicating a more realistic prediction of separation and reattachment. At the same time, the development of a secondary recirculation zone is observed near the lower wall of the duct, a feature that was not captured in the RANS solution. The formation of this flow structure implies that the EVA process modifies ν_t in a way that enables the reproduction of additional local phenomena that are critical for the adapted field structure in the region downstream of the bend.

To further clarify in which regions of the mesh the difference between the velocity fields is reduced, the corresponding adapted quantities, such as $(v_{\text{RANS}} - v_{\text{DES}})^2$ and $(v_{\text{RANS}} - v_{\text{DES}})^2\, d\Omega$, can be examined, as shown in Fig. 5.4.

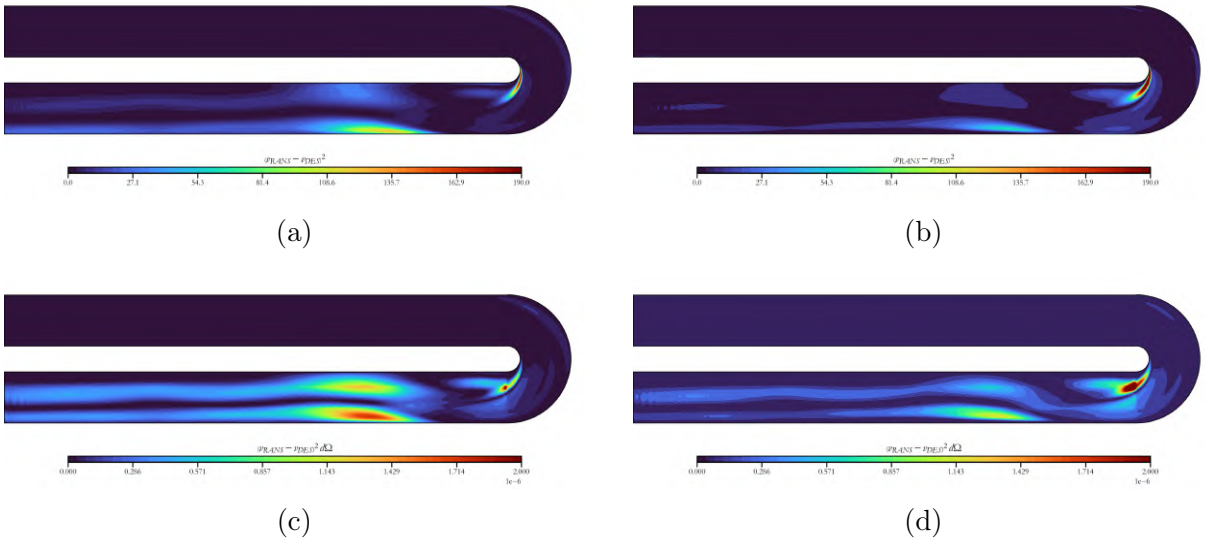

Figure 5.4: Case A: (a) Initial distribution of $(v_{\text{RANS}} - v_{\text{DES}})^2$, (b) minimized distribution of $(v_{\text{RANS}} - v_{\text{DES}})^2$, (c) initial value of the objective $(v_{\text{RANS}} - v_{\text{DES}})^2\, d\Omega$, (d) minimized value of $(v_{\text{RANS}} - v_{\text{DES}})^2\, d\Omega$.

Based on the results, the largest discrepancies (i.e., the red regions) are significantly reduced across most of the domain, while in several areas the difference becomes negligible. Nevertheless, a few localized regions of increased mismatch persist after the EVA. However, this is not unexpected, as such regions may remain or even become locally stronger, since the solution must remain consistent with the governing flow equations and the imposed model constraints. The key point is that, despite possible local redistributions of the error, the overall objective function decreases, which indicates a clear improvement when integrated over the computational domain.

Similarly, the EVA–based ν_t field Fig. 5.5c is smooth and well-organized across the domain, showing no signs of non-physical oscillations or isolated irregularities. Overall, its morphology closely follows the characteristic distribution produced by the SA model, which is also used for initialization.

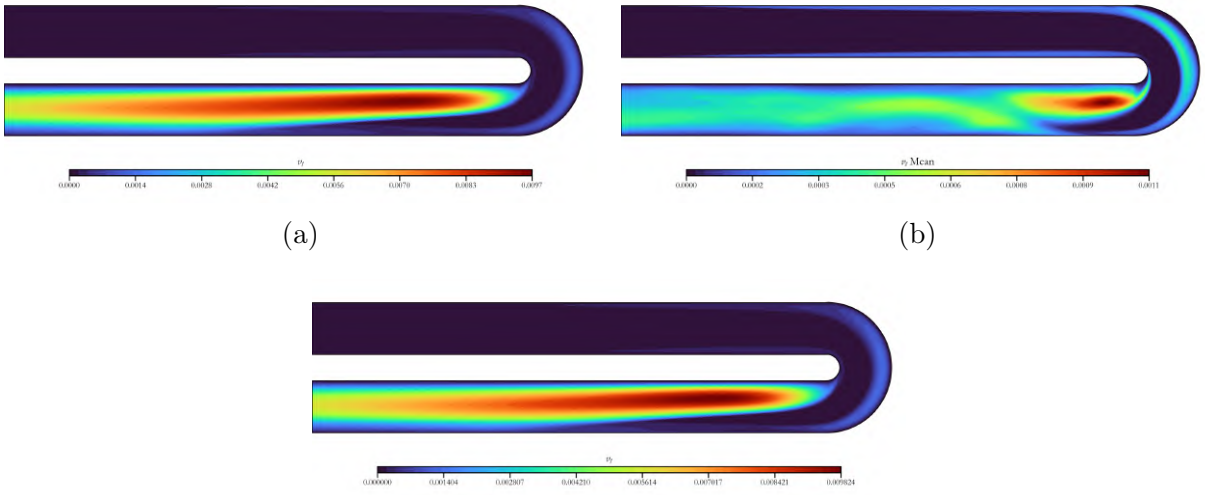

(a) (b)

(c)

Figure 5.5: Case A: ν_t field for (a) RANS, (b) time-averaged DES, and (c) EVA computed.

Finally, the adjoint velocity and pressure fields from the final EVA–minimization cycle are presented, corresponding to the converged solution of the problem Fig. 5.6.

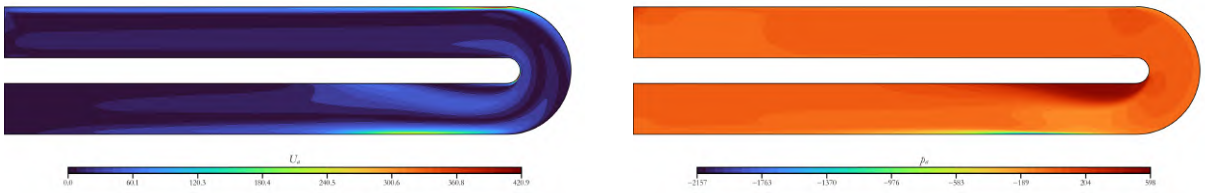

(a) (b)

Figure 5.6: Case A: (a) Adjoint velocity field, (b) adjoint pressure field.

5.2 Case B

For this case, our code was tested using both the steepest descent method and MMA as the update strategy for the design variables. The EVA–minimization with steepest descent was carried out over 10 cycles, while additional tests were performed for different values of the parameter n (step length). For the steepest descent runs, the method's performance depends strongly on the choice of n, since this parameter controls the update step and, consequently, how conservatively or aggressively the process moves towards the optimal solution. The convergence of the EVA–minimization are shown in Fig. 5.7.

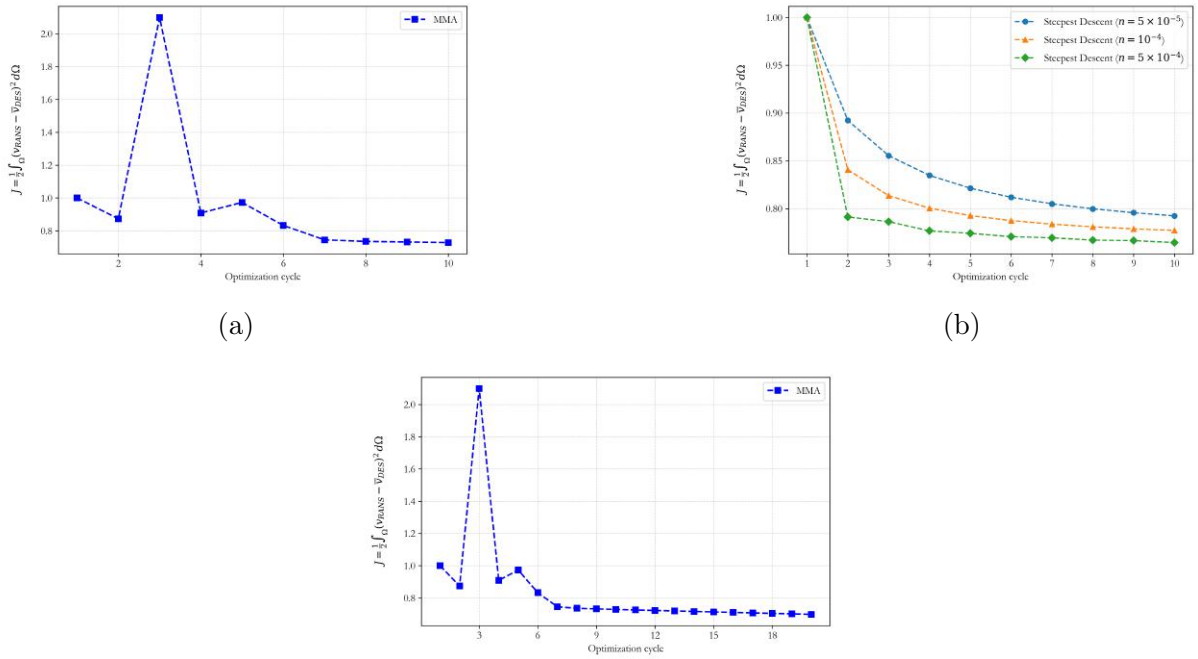

Figure 5.7: Case B: Convergence of the EVA minimization problem using: (a) MMA, (b) steepest descent, (c) MMA over, 20 cycles.

Similarly, for MMA, it is observed that, during the first 10 cycles a faster improvement is achieved compared to steepest descent. MMA leads to an additional reduction of the objective function by 3.59%. For this reason, the MMA minimization was extended to more cycles, specifically 20. Indicatively, the residuals of the final cycle are provided, corresponding to the last iteration Fig. 5.8.

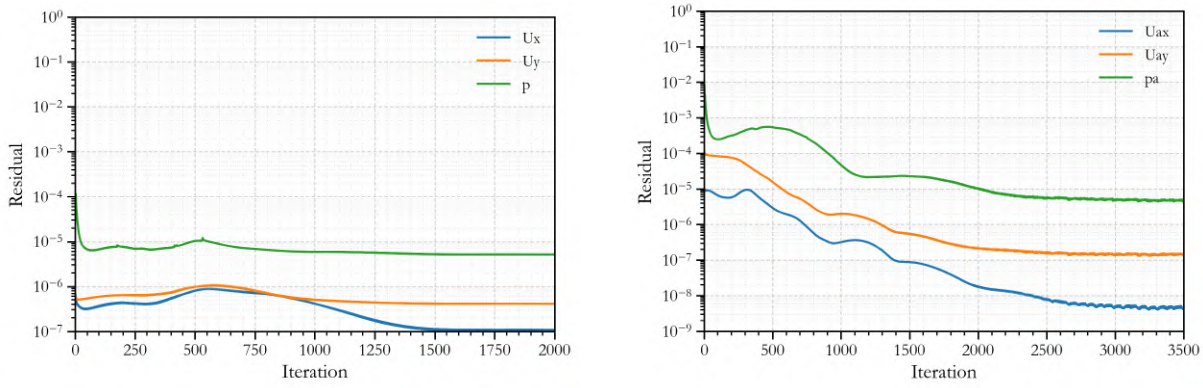

Figure 5.8: Case B: Convergence of the residuals of the primal and adjoint equations in the final EVA–minimization cycle.

The objective function J was reduced by approximately 30% compared to its initial value, which is also reflected in the flow fields, as the overall differences between the velocity fields have decreased noticeably. This is confirmed both quantitatively and visually through comparison of the corresponding distributions.

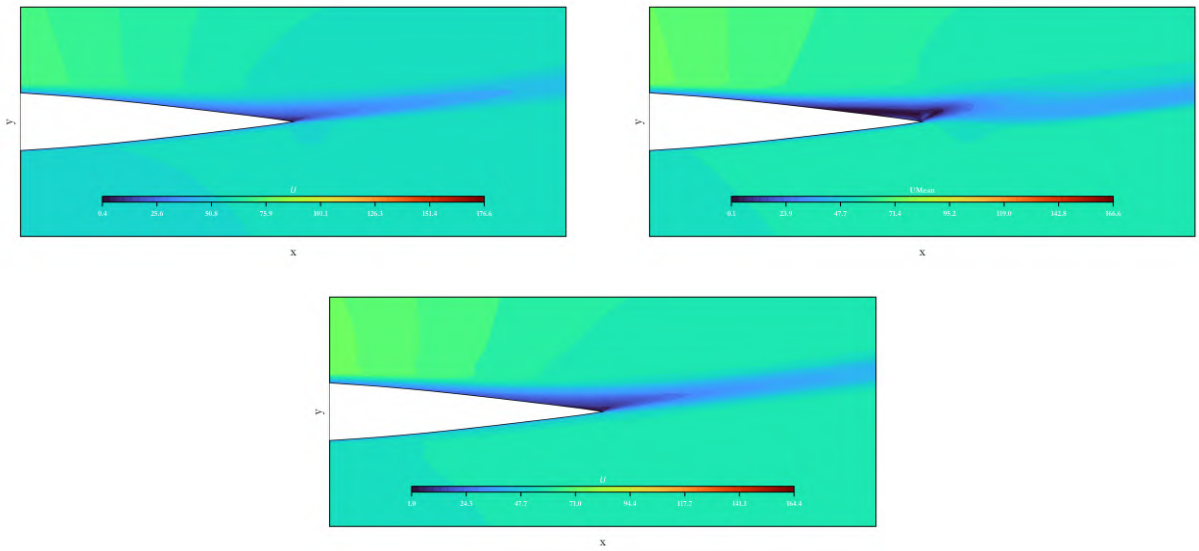

Figure 5.9: Case B: Velocity magnitude field for (a) the time-averaged DES, (b) the RANS, and (c) EVA model.

Accordingly, using the adapted quantities, $(v_{\mathrm{RANS}} - v_{\mathrm{DES}})^2$ and $(v_{\mathrm{RANS}} - v_{\mathrm{DES}})^2\, d\Omega$, a substantial reduction in the discrepancies is observed, particularly near the trailing edge, as shown in Fig. 5.10. In this region, separation is now captured, leading to a significant decrease in the difference relative to the DES solution.

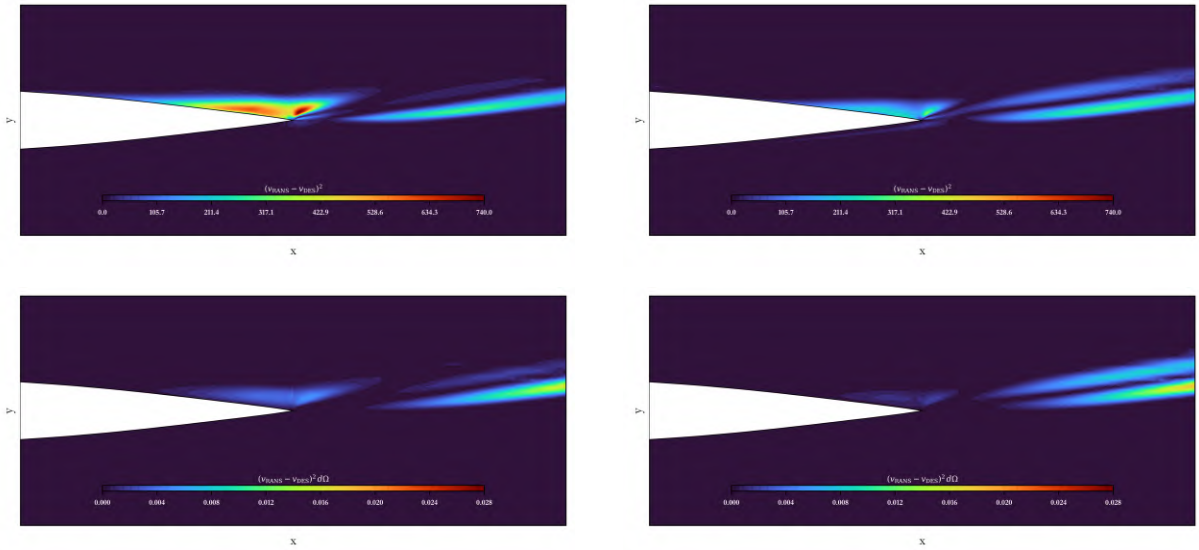

Figure 5.10: Case B: (a) Initial distribution of $(v_{\mathrm{RANS}} - v_{\mathrm{DES}})^2$, (b) minimized distribution of $(v_{\mathrm{RANS}} - v_{\mathrm{DES}})^2$, (c) initial value of the objective $(v_{\mathrm{RANS}} - v_{\mathrm{DES}})^2\, d\Omega$, (d) minimized value of $(v_{\mathrm{RANS}} - v_{\mathrm{DES}})^2\, d\Omega$.

One of the main changes observed after EVA is that the flow now reproduces the recirculation and separation region more realistically, which was the dominant deviation between RANS and DES. This is also confirmed by the C_p plots, where, as discussed, differences between DES and RANS were previously observed. It is now observed that the EVA model curve tends to approach DES along the entire length, indicating an

improved pressure distribution and, therefore, a more consistent representation of the flow Fig. 5.11.

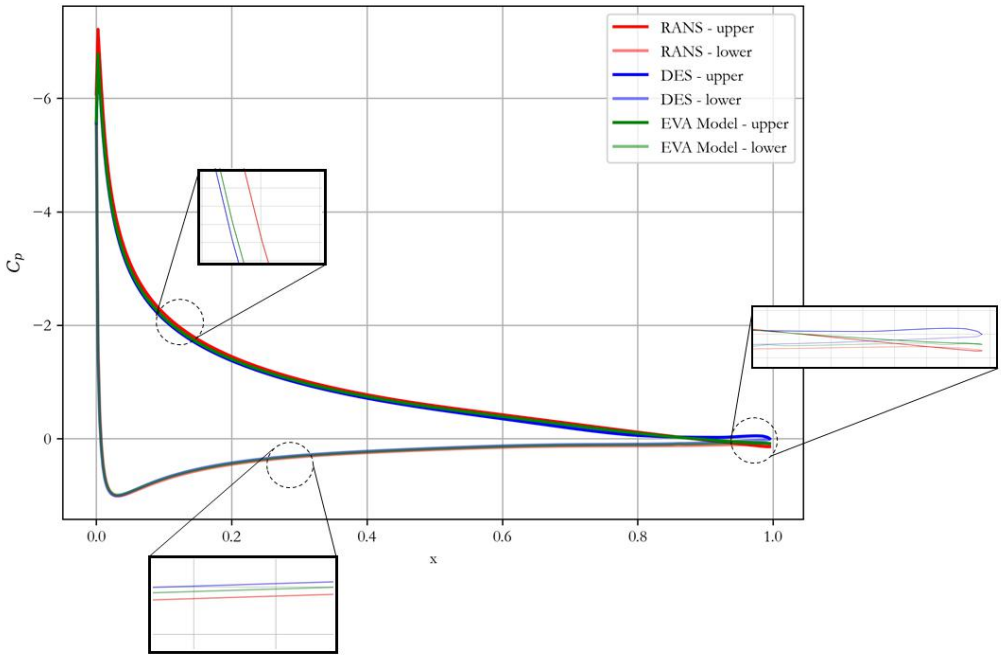

Figure 5.11: Case B: Comparison of pressure coefficient (C_p) distributions obtained from the DES, RANS, and EVA model.

Since C_L is related to the area enclosed by the C_P distribution, an improvement in the C_P curve would be expected to lead to a corresponding improvement in C_L Tab. 5.1. After EVA minimization, the predicted C_L is 65.75% closer to the DES value than the baseline RANS prediction.

	C_L
RANS	1.21932
DES	1.12985
EVA Model	1.16049

Table 5.1: Case B: Comparison between RANS, DES, and the EVA model in C_L.

On the other hand, the adapted results for the drag coefficient C_D do not improve and even deteriorate, Tab. 1. To achieve simultaneous improvements in multiple targets (e.g., velocity, pressure, C_L, and C_D), the EVA–minimization should be posed as a multi-objective (or weighted) problem, where deviations across all quantities of interest are included in the cost function.

	C_D
RANS	2.2395×10^{-2}
DES	2.4018×10^{-2}
EVA Model	2.7967×10^{-2}

Table 5.2: Case B: Comparison between RANS, DES, and the EVA model in terms of the drag coefficient C_D.

The ν_t field obtained through EVA–minimization Fig. 5.12, in contrast to Case A, exhibits more pronounced deviations from the SA initialization. Nevertheless, it retains the main wake structure introduced by the initialization, with local modifications that are introduced in order to reduce the mismatch between the RANS and DES velocity fields. The main difference observed is the formation of a distinct streamwise band of elevated ν_t, upstream of the airfoil. A similar pattern can also be identified in the corresponding adjoint-velocity field.

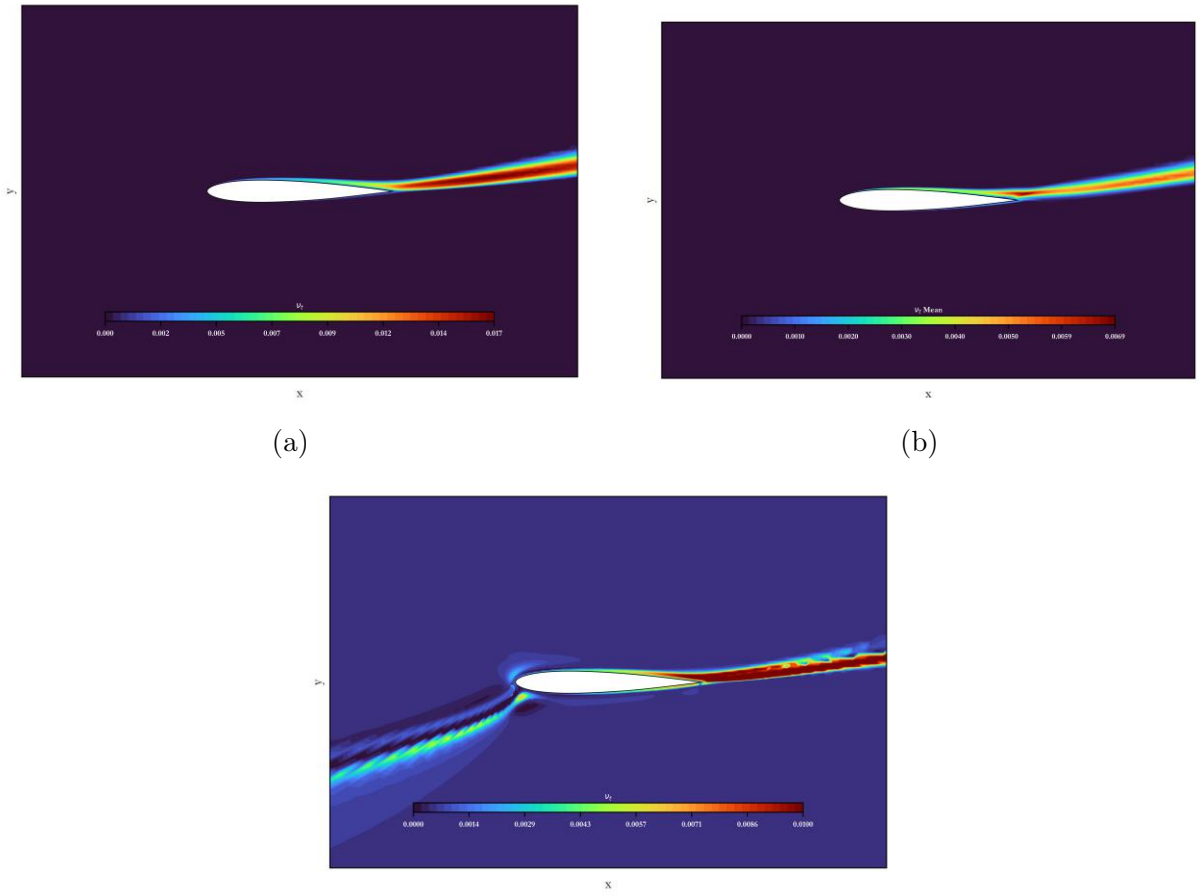

(a) (b)

(c)

Figure 5.12: Case B: ν_t field for (a) RANS, (b) time-averaged DES, and (c) the one computed using EVA.

The adjoint velocity and pressure fields are also presented in Fig. 5.13. The adjoint solution from the final EVA–minimization cycle is reported.

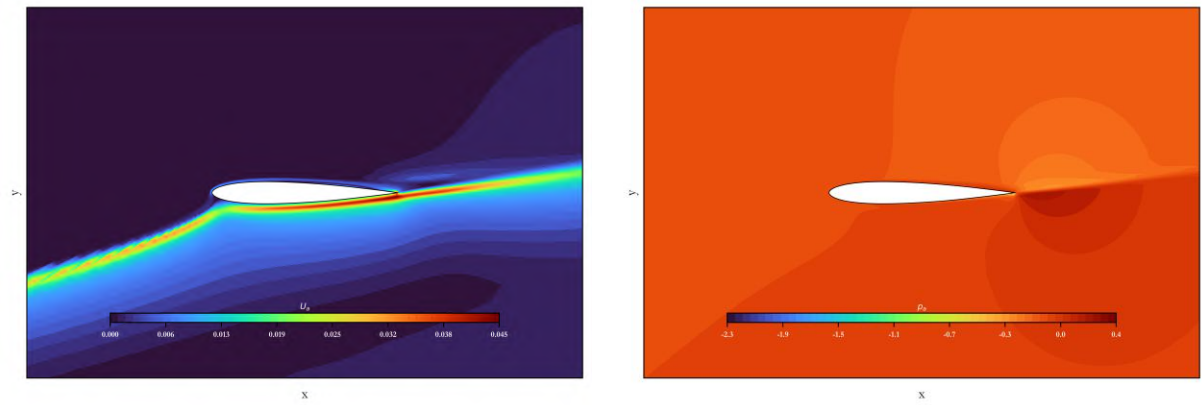

Figure 5.13: Case B: (a) Adjoint velocity field, (b) adjoint pressure field.

5.3 Case C

In the relevant literature, most applications EVA are limited to relatively simplified academic test cases that showcase the methodology and its capabilities; however, there are clearly fewer available examples in industrial applications, where the method is applied to real product geometries rather than idealized configurations. Nevertheless, the true value of EVA is demonstrated precisely in such cases, since it can contribute to reducing development time and optimizing the use of computational and experimental resources, by systematically reducing the modelling error of RANS.

The setup used is based on second-order discretization schemes, stricter (smaller) relaxation factors, and a slightly more suitable tuning of the ATC term, with the aim of improving the numerical stability of the adjoint problem. It is worth noting that the adjoint problem proved particularly sensitive, since in certain minimization cycles the adjoint solution exhibited abrupt increases and very large values in the adjoint quantities, which could lead to divergence. This behavior is also reported in the literature as a characteristic difficulty in adjoint problems and often requires additional numerical treatment to ensure reliable convergence. A central role in this difficulty is played by the Adjoint Transpose Convection (ATC) term [35], which appears in the adjoint momentum equations and is defined as:

$$u_j \frac{\partial v_j}{\partial x_i} \tag{5.1}$$

ATC is numerically stiff and often degrades the stability and convergence of the adjoint system. In (`adjointOptimisationFOAM`), a corresponding parameterization (`ATCModel`) is provided to limit its adverse effect, with options for smoothing and diffusing the correction near surfaces/patches. Indicatively, parameters such as $nSmooth$ allow the propagation of ATC smoothing over predefined layers close to the geometry, which is particularly useful [36].

Finally, due to the high computational cost of this industrial application, the procedure was limited to three (3) EVA–minimization cycles. The convergence in the final EVA–minimization cycle are presented indicatively, both for the primal solution and for the

adjoint solution Fig. 5.14b.

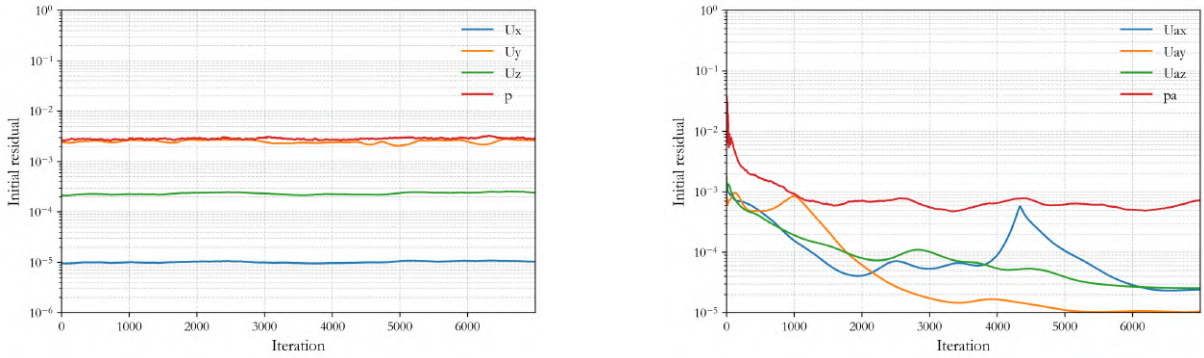

(a) (b)

Figure 5.14: Case C: Converge of the residuals of the primal and adjoint equations in the final EVA–minimization cycle.

The convergence of the drag value for the final EVA–minimization cycle is also presented Fig. 5.15.

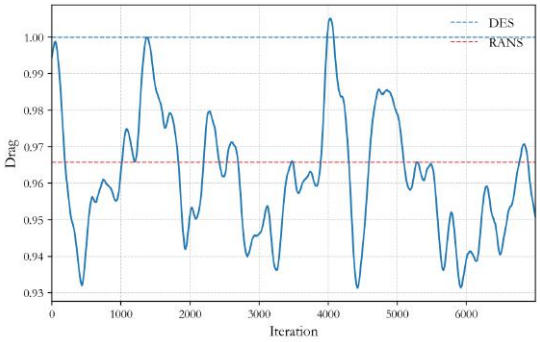

Figure 5.15: Case C: Drag coefficient evolution during the final EVA–minimization cycle.

The results indicate a clear reduction in the objective function. As will be discussed in the following, the adapted solution leads to noticeable improvements in the velocity field, as well as in related aerodynamic quantities such as $C_{p,s}$ and $C_{p,t}$, which are linked to key flow features (e.g., separation and wake development). However, as already highlighted in Case B, improving the selected objective does not necessarily imply that all quantities of interest will improve. In particular, the drag coefficient C_D does not improve in this case: the initial deviation between DES and RANS was 3.42%, whereas after the minimization EVA model yields a deviation of 3.99%. Although this difference remains small, so no definitive conclusion can be drawn on whether the method systematically degrades C_D or whether other factors contribute to this deviation, it indicates that, if accurate drag prediction is a primary requirement, C_D should be included explicitly in the minimization formulation. This would naturally lead to a multi-objective optimization setup, where the improvement of the velocity field is pursued alongside the reduction of the C_D mismatch.

Next step is to examine key quantities such as the velocity fields and the pressure-related distributions. The analysis begins with $C_{p,t}$, since it exhibited the largest differences between the RANS and DES results Fig. 7.

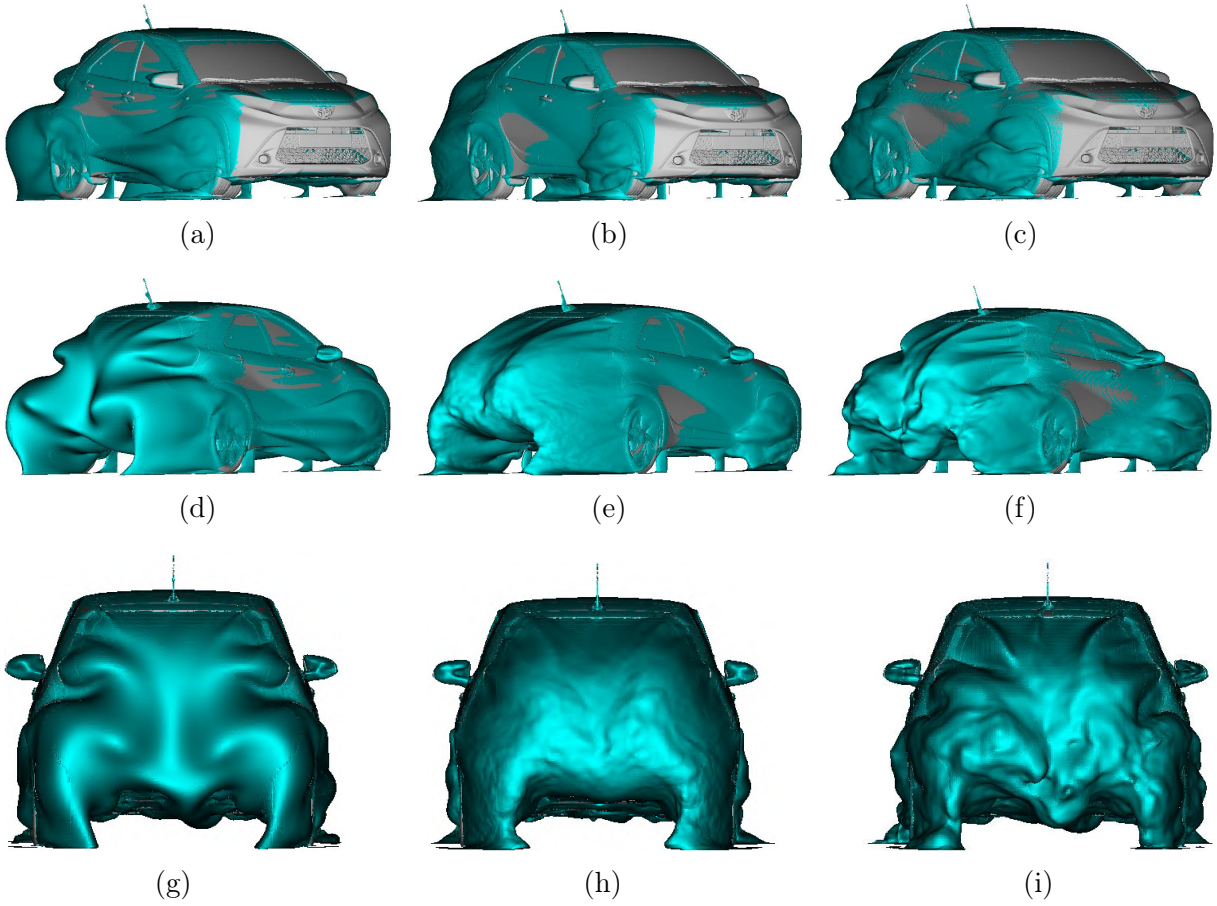

Figure 5.16: Case C: Iso-surface of C_{pt} shown from different viewing angles: (a,d,g) RANS, (b,e,h) DES, and (c,f,i) EVA model.

A clear improvement can be observed after the EVA procedure precisely in the regions where the largest discrepancies between RANS and DES were previously identified. Starting from the front-wheel area, the extended total-pressure deficit predicted by RANS is noticeably reduced. The central wake lobe becomes weaker and more confined, and the wake distribution appears more local and more clearly segmented. Although the wake topology does not fully match the DES prediction, which remains more fine-scale, the overall trend is clearly towards a more realistic flow representation than the original RANS. The most substantial improvement, however, is found at the rear of the vehicle, where the RANS tended to keep the flow attached and to underestimate separation. As a result of the EVA, separation becomes more distinct along the critical trailing edges, leading to a wake and recirculation region that is qualitatively closer to the DES behaviour. This convergence is reflected both in the $C_{p,t}$ distributions, through a reduction of the overly diffused wake predicted by the baseline RANS, and in the static-pressure coefficient $C_{p,s}$ distributions, which adopt a pattern that is more consistent with the expected separation and base-pressure characteristics at the rear of the vehicle.

This reduction is further evidenced by the $C_{p,t}$ distributions, where the EVA result shows a clear shift from the baseline RANS pattern towards the DES behavior. In addition, the static-pressure coefficient $C_{p,s}$ at the rear becomes more uniform after adaptation, which is consistent with a more distinct and extended separated region and the presence of a

stronger wake and downstream recirculation Fig. 5.17. Such a flow state typically leads to a more coherent, single-region pressure distribution, in line with the trend also observed in the RANS prediction.

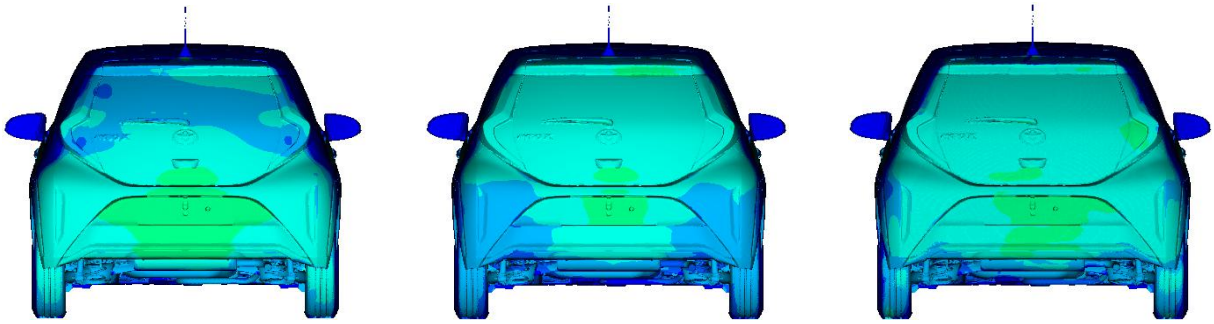

(a) (b) (c)

Figure 5.17: Case C: Static pressure coefficient contribution for (a) RANS, (b) DES, and (c) EVA model.

Finally, the discrepancies observed on the $X\Upsilon$ plane are noticeably reduced compared to the baseline RANS results Fig. 5.19. Separation, which previously represented the most pronounced difference, is now captured more clearly, while both the recirculation core and the overall wake topology approach the DES target more closely.

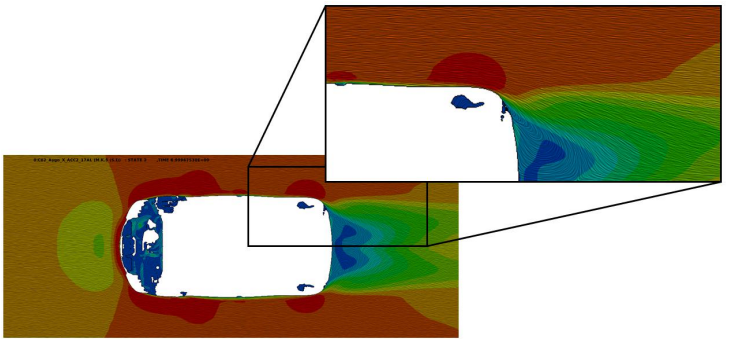

(a)

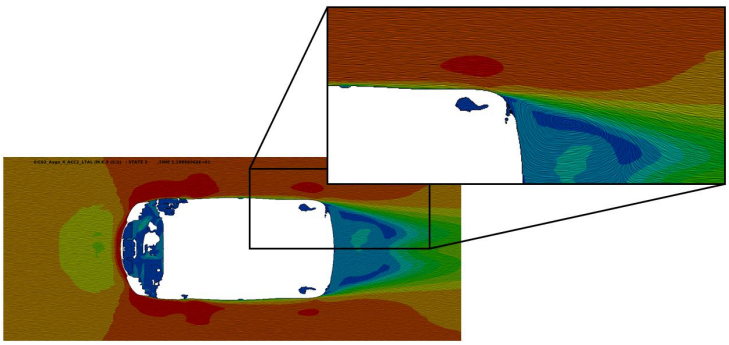

(b)

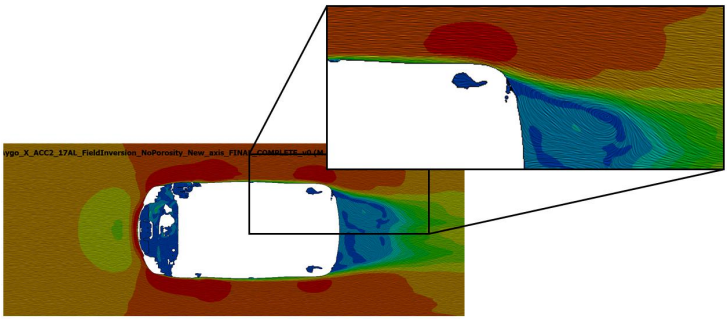

(c)

Figure 5.19: Case C: Velocity vector field on the x–z plane for (a) RANS, (b) DES, and (c) EVA model.

Similarly, on the YZ plane, the flow exhibits stronger and more fragmented structures, typically of smaller spatial extent, with frequent merging and splitting driven by enhanced mixing Fig. 5.20. Overall, these features are in much closer agreement with the corresponding DES patterns.

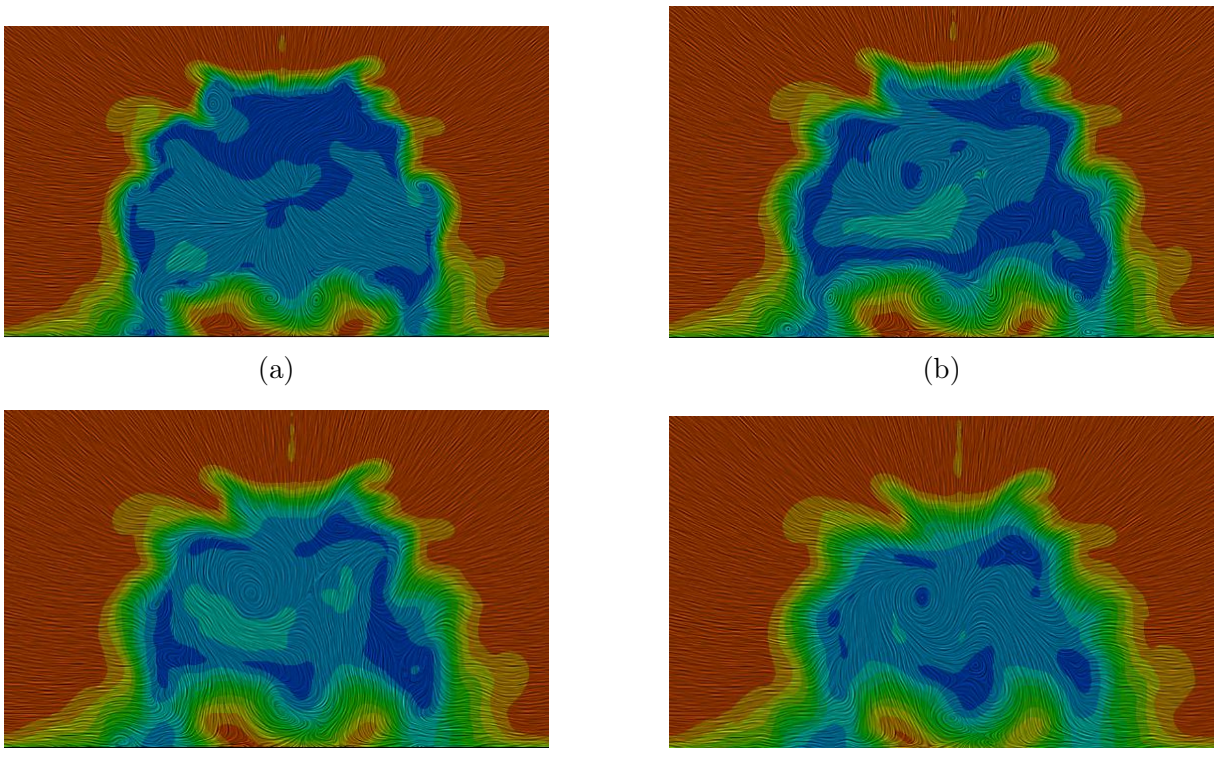

(a) (b)

(c) (d)

Figure 5.20: Case C: Velocity vector field on y–z sections downstream of the vehicle for the EVA (a–d), from the near wake to farther downstream locations behind the rear of the vehicle.

The ν_t field produced by EVA is smooth and well organized across the domain, showing no signs of non-physical oscillations or isolated irregularities Fig. 5.21. Overall, its morphology closely follows the characteristic distribution produced by the SA model, which is also used for initialization. Nevertheless, it preserves the main wake structure

of the initial field while introducing local modifications aimed at reducing the mismatch between the RANS and DES velocity fields.

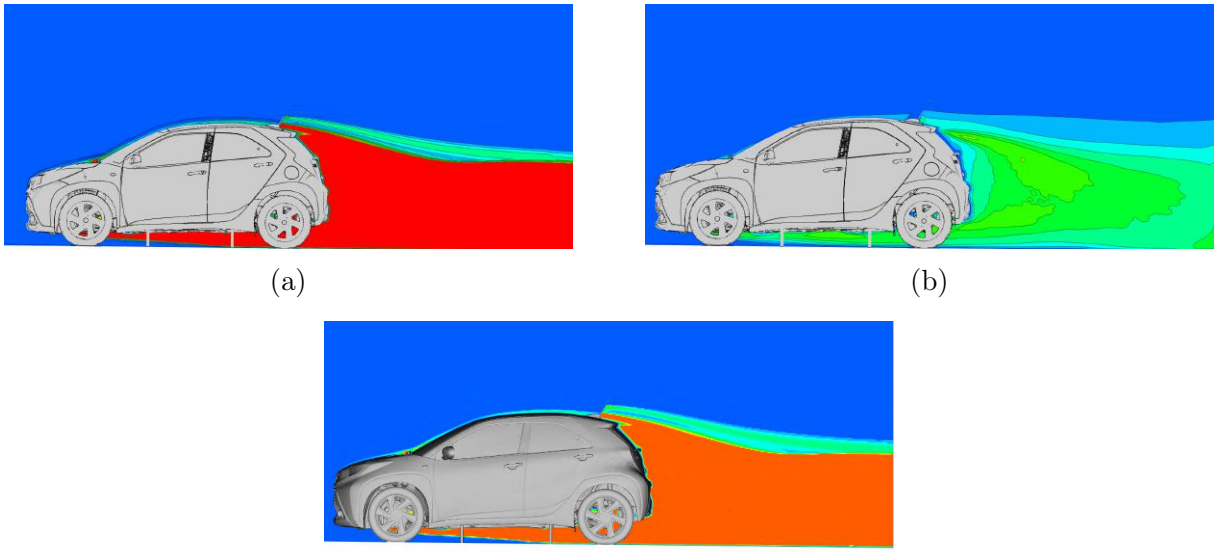

(a) (b)

(c)

Figure 5.21: Case C: ν_t field for (a) RANS, (b) time-averaged DES, and (c) EVA computed.

Chapter 6
ShpO and EVA

In OpenFOAM, the automated continuous adjoint method is employed, with the mathematical formulation and software programming developed by the PCOpt/NTUA team, to perform ShpO. This iterative process modifies the geometry of an object gradually, aiming to improve specific performance criteria, such as reducing drag or minimizing total pressure losses [36, 34]. To allow the geometry to change in a controlled and smooth manner, a parametric description of the deformation is adopted through control points, which define a 2D deformation volume around the body. The control points constitute the degrees of freedom; their displacement results in a smooth change of the surface and of the computational mesh, without abrupt changes or local discontinuities. For this reason, a particularly widespread parameterization choice is volumetric B-splines, which ensures high smoothness during the deformation, limiting the likelihood of non-physical mesh distortions. In this framework, the Cartesian coordinates of a mesh point within the control grid are obtained from the tensor product of the basis functions in the two parametric directions:

$$x\left(u,v\right)=\sum_{i=0}^{I}\sum_{j=0}^{J}U_{i,p_u}\left(u\right)V_{j,p_v}\left(v\right)b_{ij} \tag{6.1}$$

where (u, v) are the parametric coordinates of the point, U_{i,p_u}, V_{j,p_v} are the B-spline basis functions of degrees $p_u,\ p_v$, and b_{ij} are the Cartesian coordinates of the (i, j)-th control point, with I, J denoting the number of control points per direction.

After the completion of each cycle, both the improved geometry and the correspondingly deformed computational mesh are obtained, and the process is repeated in the next optimization cycles. In this way, ShpO functions as a computational tool that produces a sequence of geometries which systematically improve the selected criterion, that is, they lead to a reduction or an increase of the objective function depending on the goal, while keeping the computational cost for computing the sensitivities independent of the number of design variables.

In many cases, such as Case B with higher angles of attack or Case C, phenomena related to the unsteady phase of the flow begin to emerge, and RANS models often fail to accurately capture and represent these behaviors. In such scenarios, performing ShpO requires the use of an unsteady-type adjoint solver, which introduces several challenges.

The main difficulty with unsteady adjoint solvers is the significant computational cost, which is further compounded by the additional complexities of storing or recomputing the entire flow history. This not only increases memory usage but also adds substantial computational overhead, complicating the optimization process. There is a clear need for the development of new tools capable of generating new geometries, especially when RANS models fail to accurately reproduce the flow fields. One such technique is the frozen turbulence assumption. This approach assumes that small geometric changes only affect the mean turbulence fields. However, the sensitivities computed using this method may occasionally exhibit incorrect signs, which can significantly affect the optimization process. This issue has been extensively investigated by the PCOpt/NTUA team [37, 38].

In this thesis, building on the EVA (Eddy Viscosity Adaptation) process developed in earlier sections, a solver has been created that identifies new ν_t fields. These fields produce flow patterns that are much closer to those generated by unsteady simulations, effectively capturing phenomena such as flow separation. Here, the idea is to freeze the ν_t field computed by the EVA process during ShpO. From this point of view, such a ShpO loop will be characterized as **Frozen Eddy Viscosity (FEV)**. This way, high-fidelity information is introduced through the adapted fields rather than directly coupling DES with the gradient calculation. As a result, optimization can proceed without the need for an unsteady, DES adjoint, thus avoiding the practical challenges of unsteady adjoint optimization. To assess the proposed technique, the optimization results are compared to a steady-adjoint optimization baseline. The optimized geometries are, then, evaluated using DES to determine whether this methodology leads to a superior solution. The proposed method will be tested in Case B.

For Case B, with the same settings ($\alpha = 12^\circ$, $Re = 10^6$), a ShpO will be performed first with classic RANS for the minimization of C_D and then using the ν_t field obtained from the EVA, in order to evaluate the reliability of the procedure. The same mesh is used, and a morphing box with volumetric B-splines is defined. Specifically, the airfoil is parameterized with a Cartesian B-splines lattice 6×4. The morphing box is deliberately placed so that it does not include the leading edge and the trailing edge; in other words, the active deformation is restricted to an intermediate part of the chord, and additionally the first and last line, as well as the first two and last two columns of the control points, remain fixed, in order to ensure continuity in the y direction and continuity in the x direction. This choice reduces the risk of creating unrealistic spikes or thinning at the ends of the airfoil and helps maintain a physical and numerically stable geometry. As design variables, the internal control points are defined (4 in total), which are free to move in the x and y directions during the optimization; therefore, 8 design variables arise.

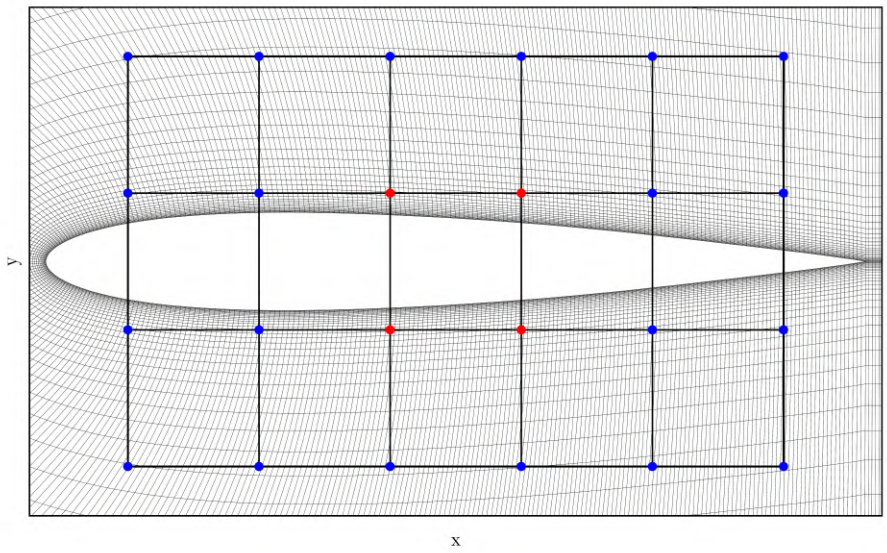

Figure 6.1: ShpO (Case B): Morphing box active control points, free to move in the x and y directions during the ShpO, are highlighted in red.

The optimized geometries using the two methods, together with the initial geometry, are compared in Fig. 6.2.

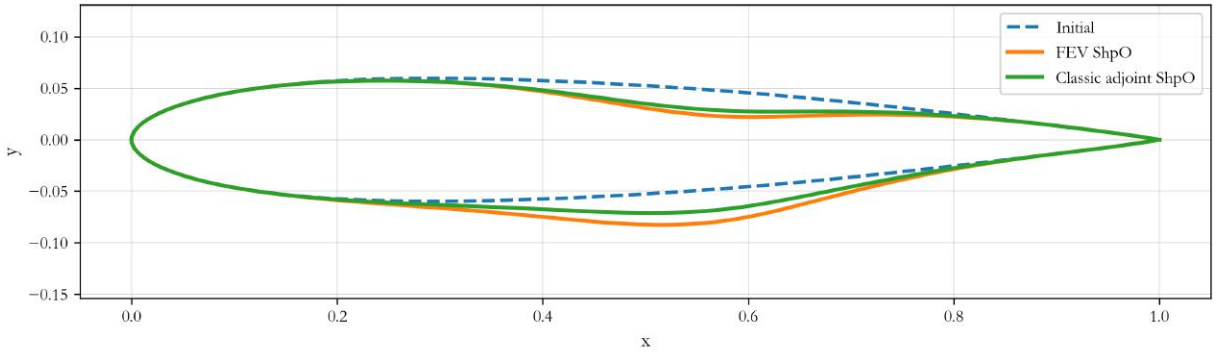

Figure 6.2: ShpO (Case B): Shape of the baseline airfoil and the optimized geometries obtained via the classic (including the adjoint to the SA model) and FEV adjoint approaches.

The drag values of the initial geometry and of the optimized geometries, re-evaluated using DES, are presented in Fig. 6.3.

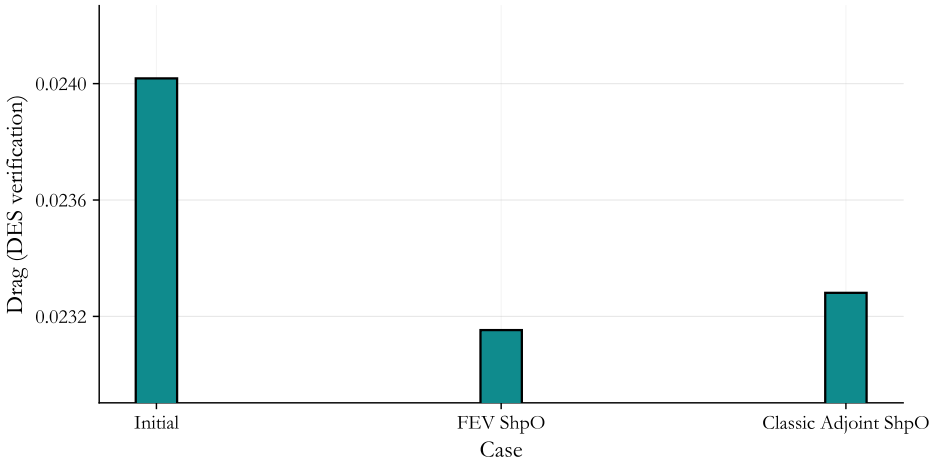

Figure 6.3: ShpO (Case B): DES-based verification of the final drag coefficient reduction for the optimized geometries obtained with the classic and frozen-turbulence approaches.

As can be observed, the EVA-based ShpO leads to an improvement of the objective function also at the DES verification level. Compared to the initial geometry (DES value), the proposed method reduces the value by 3.60%, while the classic steady-adjoint optimization reduces it by 3.07%. The difference between the two improvements at the DES level is relatively small (approximately 0.5 percentage points). For the geometry obtained with the proposed method, the wake recirculation region is reduced both in intensity and in spatial extent, which is consistent with the reduction in C_D.

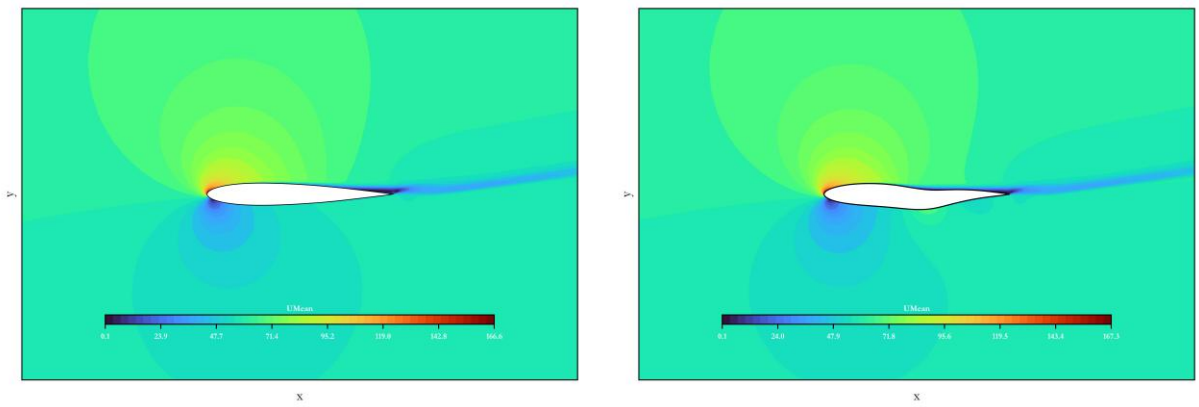

(a) (b)

Figure 6.4: ShpO (Case B): Velocity magnitude field of the time-averaged DES for (a) the initial geometry and (b) the optimized geometry obtained with the FEV approach.

Although the observed, even marginal, superiority at the DES level is a positive indication that the proposed procedure can steer the design towards improved performance also at a higher-fidelity level, this is particularly encouraging in cases where conventional RANS-based ShpO may fail to capture the key flow phenomena.

From a computational cost perspective, the proposed ShpO framework can be, per optimization cycle, more economical, since it avoids solving the additional

turbulence-model adjoint equations and associated terms during sensitivity computation. However, for a fair cost–benefit assessment, the extra preparation time required by EVA to compute the improved ν_t field which is subsequently kept fixed during the ShpO must also be taken into account. The generation of this field presupposes a higher-fidelity reference solution (DES) and a corresponding RANS run, used for forming and comparing ν_t. Therefore, the overall time-to-solution is not limited to the cost of the optimization cycles, but also includes the initial cost (RANS + DES) required to enable the proposed workflow.

Despite the above, the proposed framework remains practical and cost-effective, particularly in scenarios where the DES and RANS fields are already available. This is important because a fully unsteady, DES-consistent adjoint formulation remains practically inaccessible for many applications due to its high cost, complexity, and the limited availability of robust solvers. Moreover, once EVA has been completed, the improved ν_t field could be generated more rapidly through data-driven surrogates (e.g., neural networks) or through new closed-form turbulence models trained on the reference results. Under such a perspective, the additional preparation cost can be significantly reduced, further increasing the practical value of the proposed methodology as an efficient design-exploration procedure.

Overall, the present results indicate that further investigation of this methodology is necessary and this is, really, a realistic and promising direction for future development and application.

Chapter 7
Conclusion & Proposal for Future Work

7.1 Summary

This diploma thesis focuses on improving the predictive capability of RANS-type simulations through turbulence model adaptation. This work relies on the RANS and DES models, corresponding to the low- and high-fidelity models, respectively. Both are based on, the Spalart-Allmaras model.

Next, a systematic comparison between RANS and DES was carried out on three geometries: the U-bend duct, the NACA0012 airfoil, and the Toyota Aygo X vehicle. It was observed that the velocity fields showed significant differences, mainly in the recirculation zones, as well as in the intensity and extent of flow separation. Specifically, for the Toyota Aygo X, the predictions from the RANS model did not meet the accuracy requirements set by the WLTP regulation, and the field estimates presented completely different results for the impact of the geometry on the rear part of the body, as the RANS model failed to predict flow separation.

Subsequently, an EVA method, also known in the literature as Field Inversion, was developed and implemented. The objective function was defined as the difference between the velocity fields obtained from the RANS model and the average DES field, with the turbulent viscosity ν_t being the field of optimization variables. Since the problem involves as many optimization variables as mesh cells, the adjoint method was used for optimization. The corresponding equations were derived, leading to the final expression for the sensitivity derivatives. These were programmed in OpenFOAM.

The results showed clear improvements, as the velocity fields began to better approximate the areas with large discrepancies. Specifically, in the U-bend duct, the recirculation zone was better approximated, while in the NACA0012 airfoil, the lift coefficient improved, the separation became more pronounced, and the C_p diagram approached the target more closely. In the case of the Toyota Aygo X car, significant improvements were observed in the flow separation areas that the RANS model had failed to predict, and the predictions were now more accurate, providing a clearer picture for engineers regarding the effect of the geometry on the overall result.

Additionally, for the NACA0012 airfoil, the feasibility of using the adapted models from EVA for ShpO was investigated. The results were promising, as the steady-state

optimization method was compared with optimization using the FEV approach. Verification through DES demonstrated that this method outperformed traditional techniques in reducing the drag coefficient, providing strong evidence of the potential effectiveness of this new approach.

7.2 Conclusion & Proposal for Future Work

The EVA has proven to be highly promising, as it significantly improved the fields in all the cases studied. This method can serve as a valuable computational tool for generating suitable data that could be used in the development of new turbulence models. Although this technique is relatively recent and innovative, it appears that there is still considerable room for further improvement, so that the coefficient ν_t can have an even better impact on other flow parameters.

To achieve this, the method should be expanded to a MOO problem, with additional objectives, such as reducing drag coefficient (C_D) or minimizing pressure losses, depending on the application. Furthermore, to ensure that the field remains as uniform and generalizable as possible, it is crucial to implement constraints that prevent the unrealistic deviation of the ν_t field from the original methodology.

This method shows strong potential and represents a promising step forward, making effective use of today's available computational resources and expertise. It is particularly suitable for industries that possess both experimental data and high-fidelity simulations. With further in-depth investigation and in combination with the development of suitable datasets for training NN and DSR, as suggested in the literature, it could offer significant benefits for the creation of new turbulence models. This technique could lead to substantial cost savings, given the high computational cost of such applications, while also significantly reducing development time.

Additionally, for the NACA0012 airfoil, the potential of using the adapted models for shape optimization was examined. The results were very encouraging, as the classical RANS optimization method was compared with the proposed optimization framework. Verification with DES showed that the proposed approach achieved a larger reduction in the drag coefficient than the traditional method, providing evidence of its potential. Nevertheless, further investigation is required to assess the robustness and generality of the FEV approach across a wider range of geometries and flow conditions, and to determine whether it can consistently deliver satisfactory results.

This technique is particularly useful for products that are already manufactured and only require minor local adjustments or changes, offering significant benefits in the optimization and evaluation of new geometries with reduced computational cost.

Bibliography

[1] European Environment Agency. *Greenhouse gas emissions from transport in Europe.* Accessed: 2026-02-01. 2025. URL: https://www.eea.europa.eu/en/analysis/indicators/greenhouse-gas-emissions-from-transport.

[2] Toyota Belgium. *Worldwide Harmonized Vehicle Test Procedure (WLTP).* Accessed: 2026-02-01. Toyota Belgium. 2026. URL: https://nl.toyota.be/ontdek-toyota/doen-nul/wltp.

[3] Ministry of Land, Infrastructure, Transport and Tourism (MLIT). *Flowchart of Alternative Method Validation/Revalidation (MLIT position paper).* Working document WLTP-28-10e, Appendix 2. Document on alternative-method validation/revalidation and equivalency demonstration (incl. CFD) in the WLTP type-approval context. Ministry of Land, Infrastructure, Transport and Tourism (Japan), Sept. 2019.

[4] J. Hart. «Comparison of turbulence modeling approaches to the simulation of a dimpled sphere». In: *Procedia Engineering* 147 (2016), pp. 68–73.

[5] K. J. Fidkowski. «Gradient-based shape optimization for unsteady turbulent simulations using field inversion and machine learning». In: *Aerospace Science and Technology* 129 (2022). Published online: 26 August 2022, p. 107843.

[6] K. Duraisamy, Z. Zhang, and A. Singh. «New approaches in turbulence and transition modeling using data-driven techniques». In: *53rd AIAA Aerospace Sciences Meeting.* 2015.

[7] G. Alessi. «Adjoint Shape Optimization Based on Large Eddy Simulations through an Adaptation of the Reynolds-Averaged Navier–Stokes Equations». Supervisors: B. Blocken, J.-P.-A.-J. van Beeck, T. Verstraete. PhD dissertation. Leuven, Belgium: KU Leuven, Faculty of Engineering Science (Arenberg Doctoral School), Dec. 2020.

[8] C. Wu and Y. Zhang. «Data-driven Turbulence Modeling Using Field Inversion and Deep Symbolic Regression». In: *Aerospace Europe Conference 2023 (10th EUCASS / 9th CEAS).* 2023.

[9] V. Srivastava et al. *Augmenting RANS Turbulence Models Guided by Field Inversion and Machine Learning.* Tech. rep. NASA/TM–20240012512. Available from NASA Center for AeroSpace Information (CASI), NASA STI Program. NASA Langley Research Center, 2024.

[10] D. J. C. MacKay. *Information Theory, Inference, and Learning Algorithms.* On-screen viewing permitted. Cambridge: Cambridge University Press, 2003.

[11] B. K. Petersen et al. «Deep Symbolic Regression: Recovering Mathematical Expressions from Data via Risk-Seeking Policy Gradients». In: *International Conference on Learning Representations (ICLR)*. 2021.

[12] A.-S. I. Margetis. «Unsteady RANS & (D)DES Continuous Adjoint and Compression Techniques in Aerodynamic Shape Optimization». Supervisor: K. C. Giannakoglou. PhD Thesis. Athens, Greece: National Technical University of Athens (NTUA), School of Mechanical Engineering, Fluids Section, Parallel CFD & Optimization Unit, 2024.

[13] P. Sagaut, S. Deck, and M. Terracol. *Multiscale and Multiresolution Approaches in Turbulence*. 2nd ed. Imperial College Press, 2013.

[14] G. N. Coleman and R. D. Sandberg. *A Primer on Direct Numerical Simulation of Turbulence: Methods, Procedures and Guidelines*. Technical Report AFM-09/01a. Southampton, United Kingdom: University of Southampton, School of Engineering Sciences, Aerodynamics & Flight Mechanics Research Group, Mar. 2010.

[15] D. G. E. Grigoriadis et al., eds. *Direct and Large-Eddy Simulation X*. Vol. 24. ERCOFTAC Series. Springer International Publishing, 2018.

[16] Y. Hoarau et al., eds. *Progress in Hybrid RANS–LES Modelling: Papers Contributed to the 6th Symposium on Hybrid RANS-LES Methods, 26–28 September 2016, Strasbourg, France*. Vol. 137. Notes on Numerical Fluid Mechanics and Multidisciplinary Design. Springer International Publishing, 2018.

[17] O. Reynolds. «On the Dynamical Theory of Incompressible Viscous Fluids and the Determination of the Criterion». In: *Philosophical Transactions of the Royal Society of London. Series A* 186 (1895), pp. 123–164. URL: `http://www.jstor.org/stable/90643`.

[18] B. E. Launder and D. B. Spalding. «The Numerical Computation of Turbulent Flows». In: *Computer Methods in Applied Mechanics and Engineering* 3.2 (1974), pp. 269–289.

[19] F. R. Menter. «Zonal Two-Equation k–ω Turbulence Models for Aerodynamic Flows». In: *24th Fluid Dynamics Conference*. AIAA Paper 93-2906. American Institute of Aeronautics and Astronautics, 1993.

[20] F. R. Menter. «Two-Equation Eddy-Viscosity Turbulence Models for Engineering Applications». In: *AIAA Journal* 32.8 (1994), pp. 1598–1605.

[21] P. R. Spalart and S. R. Allmaras. «A One-Equation Turbulence Model for Aerodynamic Flows». In: *La Recherche Aérospatiale* 1 (1994), pp. 5–21.

[22] M. A. H. Al-fahham. «A Modelling and Experimental Study to Reduce Boundary Layer Flashback with Microstructure». PhD thesis. Cardiff, UK: Cardiff University, School of Engineering, 2017.

[23] OpenFOAM. *User Guide: nutUSpaldingWallFunction (Spalding Wall Function)*. `https://www.openfoam.com/documentation/guides/latest/doc/guide-bcs-wall-turbulence-nutUSpaldingWallFunction`. Accessed: 2026-02-02.

[24] P. R. Spalart et al. «Comments on the Feasibility of LES for Wings, and on a Hybrid RANS/LES Approach». In: *Advances in DNS/LES: Proceedings of the First AFOSR International Conference on DNS/LES, Louisiana Tech University, Ruston, Louisiana, USA, August 4–8, 1997*. Ed. by C. Liu, Z. Liu, and L. Sakell. Columbus, OH, USA: Greyden Press, 1997.

[25] P. R. Spalart et al. «A new version of detached-eddy simulation, resistant to ambiguous grid densities». In: *Theoretical and Computational Fluid Dynamics* 20 (2006), pp. 181–195.

[26] M. L. Shur et al. «A hybrid RANS-LES approach with delayed-DES and wall-modelled LES capabilities». In: *International Journal of Heat and Fluid Flow* 29.6 (Dec. 2008), pp. 1638–1649.

[27] *OpenFOAM Repositories*. Download page listing the official OpenFOAM code repositories. OpenCFD Ltd (Keysight). n.d. URL: `https://www.openfoam.com/download/openfoam-repositories` (visited on 01/27/2026).

[28] *blockMesh*. Wiki page (OpenFOAM meshing utility documentation). OpenFOAMWiki. n.d. URL: `https://openfoamwiki.net/index.php/BlockMesh` (visited on 01/27/2026).

[29] *snappyHexMesh*. Wiki page (OpenFOAM meshing utility documentation). OpenFOAMWiki. n.d. URL: `https://openfoamwiki.net/index.php/SnappyHexMesh` (visited on 01/27/2026).

[30] *simpleFoam*. Wiki page (OpenFOAM user guide). OpenFOAMWiki. n.d. URL: `https://openfoamwiki.net/index.php/SimpleFoam` (visited on 01/27/2026).

[31] *The PIMPLE algorithm in OpenFOAM*. Wiki page (OpenFOAM guide). OpenFOAMWiki. n.d. URL: `https://openfoamwiki.net/index.php/OpenFOAM_guide/The_PIMPLE_algorithm_in_OpenFOAM` (visited on 01/27/2026).

[32] F. Coletti et al. «Optimization of a U-Bend for Minimal Pressure Loss in Internal Cooling Channels—Part II: Experimental Validation». In: *Journal of Turbomachinery* 135 (Sept. 2013), pp. 051016-1–051016-10.

[33] K. C. Giannakoglou. *Μέθοδοι Βελτιστοποίησης στην Αεροδυναμική*. 4th ed. Lecture notes (4th edition, with exercises). Athens, Greece: National Technical University of Athens (NTUA), School of Mechanical Engineering, 2006.

[34] E. M. Papoutsis–Kiachagias. «Adjoint Methods for Turbulent Flows, Applied to Shape or Topology Optimization and Robust Design». Supervisor: K. C. Giannakoglou. PhD Thesis. Athens, Greece: National Technical University of Athens (NTUA), School of Mechanical Engineering, Fluids Section, Laboratory of Thermal Turbomachines, Parallel CFD & Optimization Unit, 2013.

[35] G. K. Karpouzas. «A Hybrid Method for Shape and Topology Optimization in Fluid Mechanics». Academic Advisor: Prof. K. C. Giannakoglou. Industrial Advisor: Dr. E. De Villiers (Engys Ltd.). PhD Thesis. Athens, Greece: National Technical University of Athens (NTUA), School of Mechanical Engineering, Fluids Section, Parallel CFD & Optimization Unit, 2019.

[36] N. Galanos K.C. Giannakoglou E.M. Papoutsis-Kiachagias. *AdjointOptimisationFoam, an OpenFOAM-based optimisation tool*. Version 2.3.12. Parallel CFD Optimization Unit, School of Mechanical Engineering, National Technical University of Athens. 2023. URL: `https://www.ntua.gr`.

[37] E. M. Papoutsis-Kiachagias. «Adjoint methods for turbulent flows, applied to shape and topology optimization and robust design». PhD thesis, Lab. of Thermal Turbomachines. PhD thesis. N.T.U.A., Athens, 2013.

[38] E. M. Papoutsis-Kiachagias and K. C. Giannakoglou. *Continuous adjoint methods for turbulent flows, applied to shape and topology optimization: Industrial applications*. Springer, 2014.

Εκτενής Περίληψη Διπλωματικής Εργασίας

Εθνικό Μετσόβιο Πολυτεχνείο
Σχολή Μηχανολόγων Μηχανικών
Τομέας Ρευστών
Μονάδα Παράλληλης Υπολογιστικής Ρευστοδυναμικής &
Βελτιστοποίησης

Προσαρμογή Τυρβώδους συνεκτικότητας με τη Συνεχή Συζυγή Μέθοδο με Εφαρμογή στην Αεροδυναμική Βελτιστοποίηση Μορφής

Διπλωματική Εργασία

Χαράλαμπος Τσολάκος

Ακαδημαϊκός Επιβλέπων: Κυριάκος Χ. Γιαννακόγλου, Καθηγητής ΕΜΠ

Βιομηχανικός Επιβλέπων: Antoine Delacroix, Manager TME

Αθήνα, 2026

Εισαγωγή

Τα τελευταία χρόνια, λόγω της κλιματικής αλλαγής, η βιομηχανία, και ιδιαίτερα ο τομέας της αυτοκίνησης, επηρεάζεται από αυστηρότερους κανονισμούς όσον αφορά τις εκπομπές CO_2 και την κατανάλωση καυσίμου. Η αγορά στρέφεται σε λύσεις χαμηλών ή μηδενικών εκπομπών, ενώ το ευρωπαϊκό πλαίσιο επιταχύνει αυτή τη μετάβαση. Οι αυστηρότεροι κανονισμοί επιβάλλουν τακτικούς ελέγχους και απαιτούν ακριβή υπολογισμό μεγεθών που συνδέονται άμεσα με τον αεροδυναμικό σχεδιασμό του οχήματος. Αν και οι πειραματικές δοκιμές παραμένουν η πιο αξιόπιστη μέθοδος αξιολόγησης, απαιτούν χρόνο και κόστος, γεγονός που καθιστά τις προσομοιώσεις CFD ένα κρίσιμο εργαλείο για την αξιολόγηση. Ωστόσο, για να θεωρηθούν αξιόπιστες οι προσομοιώσεις πρέπει να πληρούν ένα όριο ακρίβειας, το οποίο καθορίζεται από τα πρότυπα του WLTP. Η αύξηση της ακρίβειας των προσομοιώσεων απαιτεί την επιλογή αντίστοιχων μοντέλων τύρβης υψηλής πιστότητας, τα οποία όμως συνεπάγονται υψηλές υπολογιστικές απαιτήσεις. Αυτό καθιστά αναγκαία τη χρήση μεθόδων που συνδυάζουν χαμηλότερο κόστος με αξιόπιστες προβλέψεις. Μία τέτοια μέθοδος είναι η αξιοποίηση δεδομένων υψηλής πιστότητας για τη βελτίωση των προβλέψεων, μειώνοντας παράλληλα το υπολογιστικό κόστος. Η μέθοδος βασίζεται στην υποκατάσταση μοντέλων τύρβης σε χρονικά μόνιμους κώδικες, σε έναν βρόχο βελτιστοποίησης. Αυτή η προσέγγιση βελτιώνει τη διαδικασία σχεδιασμού και εξοικονομεί σημαντικούς πόρους που απαιτούνται για την ανάπτυξη ενός προϊόντος.

Σύγκριση RANS και DES (Θεωρητικά)

Η επιλογή του μοντέλου τύρβης είναι πάντα ένας συμβιβασμός ακρίβειας και υπολογιστικού κόστους. Στη βιβλιογραφία, αυτή η σχέση συχνά απεικονίζεται με τη μορφή μιας πυραμίδας, όπου στη βάση βρίσκονται τα πιο οικονομικά υπολογιστικά μοντέλα, τα οποία συνοδεύονται από απλοποιήσεις και παραδοχές, με αποτέλεσμα χαμηλότερη ακρίβεια.

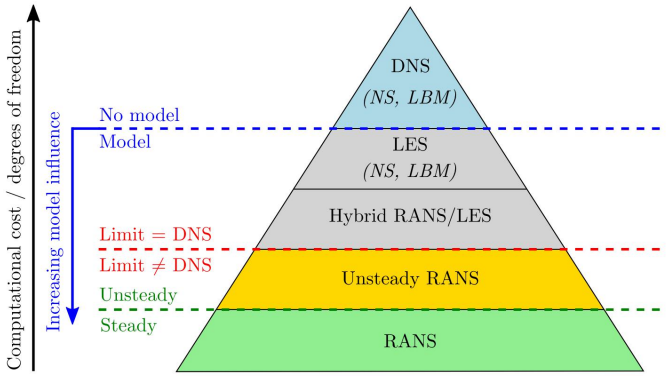

Σχήμα 1: Η ιεράρχιση των μοντέλων τύρβης, απεικονίζοντας τον συμβιβασμό μεταξύ υπολογιστικού κόστους και ακρίβειας πρόβλεψης, από [13].

Η επίδραση του μοντέλου τύρβης σε μια προσομοίωση αποτυπώνεται στο Σχήμα 2, η οποία δείχνει τη ροή γύρω από μια σφαίρα και τον βαθμό λεπτομέρειας στην περιγραφή της τύρβης, ανάλογα με το μοντέλο που επιλέγεται.

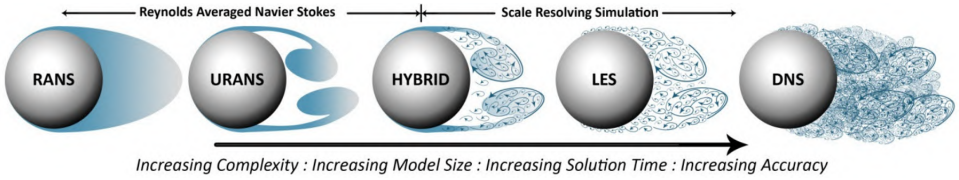

Σχήμα 2: Αντιπροσωπευτικές δομές του ομόρου πίσω από μία σφαίρα, όπως προβλέπονται από τα διάφορα μοντέλα τύρβης, από [4].

Στη διπλωματική αυτή εργασία θα χρησιμοποιηθούν οι μόνιμες εξισώσεις Reynolds-Averaged Navier–Stokes (RANS), οι οποίες αποτελούν ένα αποδεκτό μοντέλο στη μοντελοποίηση τυρβωδών ροών. Η βασική ιδέα πίσω από την προσέγγιση RANS είναι ότι σε τυρβώδεις ροές όλα τα στιγμιαία μεγέθη $f(x,t)$ μπορούν να αναλυθούν ως το άθροισμα δύο χρονικών συνιστωσών, μιας μέσης χρονικής τιμής και μιας διακύμανσης. Από την άλλη, η βασική ιδέα πίσω από το DES (Detached Eddy Simulation) είναι η χρήση ενός ενιαίου μοντέλου τύρβης, το οποίο λειτουργεί ως μοντέλο RANS στις περιοχές κοντά στο τοίχωμα και ως μοντέλο LES στο εσωτερικό του ρεύματος, ανάλογα και με την τοπική χωρική διακριτοποίηση του χωρίου. Η κύρια διαφορά τους έγκειται στο γεγονός ότι το RANS επιδέχεται χρονικά μόνιμες επιλύσεις πεδίων ροής, ενώ το DES υποχρεωτικά επιλύεται με τις μη-μόνιμες εξισώσεις ροής.

Διόρθωση του Μοντέλου Τύρβης

Όπως θα διαπιστωθεί και από τα παραδείγματα, το υπολογιστικό κόστος του DES είναι κατά μία τάξη μεγέθους μεγαλύτερο από το αντίστοιχο του RANS. Όπως συχνά συμβαίνει σε αυτές τις συγκρίσεις, τα αποτελέσματα του RANS συχνά δεν επιτυγχάνουν την απαιτούμενη ακρίβεια. Για το λόγο αυτό, τα τελευταία χρόνια παρατηρείται μια αυξανόμενη ανάγκη για νέα μοντέλα τύρβης ή για υποκατάστατα τους, τα οποία να γεφυρώνουν το χάσμα μεταξύ ακρίβειας και υπολογιστικού κόστους. Στο πλαίσιο αυτό, οι data-driven προσεγγίσεις αναδεικνύονται ως μια ιδιαίτερα υποσχόμενη στρατηγική, καθώς επιτρέπουν τη προσαρμογή ή την υποκατάσταση των μοντέλων τύρβης μέσω της αξιοποίησης DES δεδομένων.

Στον βιομηχανικό τομέα, όπου συχνά είναι διαθέσιμα δεδομένα υψηλής πιστότητας από χρόνια ανάπτυξης (όπως LES/DES προσομοιώσεις ή πειραματικές μετρήσεις), υπάρχει η δυνατότητα να αξιοποιηθεί αυτή η συσσωρευμένη πληροφορία για την έξυπνη υποκατάσταση των υπαρχόντων μοντέλων τύρβης. Ιδιαίτερο ενδιαφέρον παρουσιάζουν οι προσεγγίσεις που δεν περιορίζονται στην απλή αναπροσαρμογή των σταθερών ενός ήδη καθορισμένου μοντέλου, αλλά επιδιώκουν να εντοπίσουν και να διορθώσουν ελλείψεις στη λειτουργική του μορφή. Μία από τις πιο δημοφιλείς τεχνικές που έχει αρχίσει να εμφανίζεται στη βιβλιογραφία είναι η αντιστροφή πεδίου (Field Inversion), η οποία ανήκει στην ευρύτερη διαδικασία προσαρμογής της υπολογιζόμενης τυρβώδους συνεκτικότητας (Eddy Viscosity Adaptation, EVA).

Η διαδικασία EVA, στην ουσία, χρειάζεται να επιλύσει ένα πρόβλημα ελαχιστοποίησης, με σκοπό την εύρεση του πεδίου ν_t στο μοντέλο RANS, έτσι ώστε το πεδίο ταχυτήτων v_i να προσεγγίζει όσο το δυνατόν καλύτερα το μέσο πεδίο αναφοράς $\bar{v_i}$, το οποίο έχει εξαχθεί από προσομοιώσεις υψηλής ακρίβειας, όπως το DES. Η διαδικασία αυτή διατυπώνεται ως πρόβλημα ελαχιστοποίησης, με αντικειμενική συνάρτηση:

$$J = \frac{1}{2}\int_{\Omega} \left(v_{\text{RANS}} - \overline{v}_{DES}\right)^2 \, d\Omega \tag{1}$$

Αυτή η διαδικασία βασίζεται στις εξισώσεις της ορμής (στη μορφή που συμπεριλαμβάνεται η επίδραση της τυρβώδους συνεκτικότητας) και της συνέχειας, οι οποίες εκφράζονται ως εξής:

$$R^p = -\frac{\partial v_j}{\partial x_j} = 0 \tag{2}$$

$$R_i^v = v_j \frac{\partial v_i}{\partial x_j} - \frac{\partial}{\partial x_j}\left[(\nu + \nu_t)\left(\frac{\partial v_i}{\partial x_j} + \frac{\partial v_j}{\partial x_i}\right)\right] + \frac{\partial p}{\partial x_i} = 0 \tag{3}$$

Αφετηρία για τη διατύπωση του συζυγούς προβλήματος είναι η εισαγωγή της επαυξημένης συνάρτησης F_{aug}, η οποία ορίζεται ως εξής:

$$F_{\text{aug}} = J + \int_{\Omega} u_i R_i^v \, d\Omega + \int_{\Omega} q R^p \, d\Omega \tag{4}$$

όπου R_i^u είναι οι εξισώσεις ορμής, R^p είναι η εξίσωση συνέχειας, u_i η συζυγής ταχύτητα, q η συζυγής πίεση και Ω το υπολογιστικό πεδίο.

Η επαυξημένη συνάρτηση διαφορίζεται ως προς το πεδίο τυρβώδους συνεκτικότητας ν_t, άρα παίρνουμε:

$$\frac{\delta F_{\text{aug}}}{\delta \nu_t} = \frac{\delta J}{\delta \nu_t} + \int_{\Omega} u_i \frac{\delta R_i^v}{\delta \nu_t} \, d\Omega + \int_{\Omega} q \frac{\delta R^p}{\delta \nu_t} \, d\Omega \tag{5}$$

Τελικά, η μορφή που καταλήγει είναι η εξής:

$$\begin{aligned}
\frac{\delta F_{\text{aug}}}{\delta \nu_t} = & \int_{\Omega} \left[\frac{\partial j}{\partial v_i} + \frac{\partial q}{\partial x_i} + u_j \frac{\partial v_j}{\partial x_i} - \frac{\partial \left(u_i v_j\right)}{\partial x_j} - (\nu + \nu_t)\frac{\partial}{\partial x_j}\left[\frac{\partial u_i}{\partial x_j} + \frac{\partial u_j}{\partial x_i}\right]\right] \frac{\partial v_i}{\partial \nu_t} d\Omega \\
& + \int_{\Omega} \left[\frac{\partial j}{\partial p} - \frac{\partial u_i}{\partial x_i}\right] \frac{\partial p}{\partial \nu_t} d\Omega \\
& + \int_{\Omega} \frac{\partial u_i}{\partial x_j} \frac{\delta \nu_t}{\delta \nu_{t,P}} \left(\frac{\partial v_i}{\partial x_j} + \frac{\partial v_j}{\partial x_i}\right) d\Omega \\
& + \int_{S} \left[-q n_i \; + u_i v_j n_j + (\nu + \nu_t)\left(\frac{\partial u_i}{\partial x_j} + \frac{\partial u_j}{\partial x_i}\right) n_{\;j}\right] \frac{\partial v_i}{\partial \nu_t} dS \\
& + \int_{S} u_i n_i \frac{\partial p}{\partial \nu_t} dS - \int_{S} u_i n_j \left[\frac{\partial}{\partial \nu_t}\left((\nu + \nu_t)\left(\frac{\partial v_i}{\partial x_j} + \frac{\partial v_j}{\partial x_i}\right)\right)\right] dS
\end{aligned} \tag{6}$$

Λαμβάνοντας υπόψη την εξίσωση (6) και θέτοντας τους πολλαπλασιαστές των παραγώγων των ροϊκών ποσοτήτων ως προς τις μεταβλητές σχεδιασμού, μέσα στα χωρικά ολοκληρώματα ίσους με το μηδέν, προκύπτουν οι συζυγείς πεδιακές εξισώσεις:

$$R^p = \frac{\partial j}{\partial p} - \frac{\partial u_i}{\partial x_i} = 0 \tag{7}$$

$$R_i^u = \frac{\partial j}{\partial v_i} + \frac{\partial q}{\partial x_i} + u_j \frac{\partial v_j}{\partial x_i} - \frac{\partial \left(u_i v_j\right)}{\partial x_j} - \left(\nu + \nu_t\right) \frac{\partial}{\partial x_j} \left[\frac{\partial u_i}{\partial x_j} + \frac{\partial u_j}{\partial x_i}\right] = 0 \tag{8}$$

όπου:

$$\frac{\partial j}{\partial p} = 0 \quad \& \quad \frac{\partial j}{\partial v_i} = v_i - \overline{v}_i \tag{9}$$

Οι οριακές συνθήκες των συζυγών εξισώσεων δίνονται αναλυτικά στο αγγλικό κείμενο. Μετά την εξαγωγή των συζυγών εξισώσεων και των συζυγών οριακών συνθηκών, η τελική έκφραση των παραγώγων ευαισθησίας, που θα χρησιμοποιηθούν σε ένα πρόβλημα εύρεσης του βέλτιστου πεδίου της τυρβώδους συνεκτικότητας, δίνεται από:

$$\frac{\delta F_{\text{aug}}}{\delta \nu_t} = \frac{\partial u_i}{\partial x_j} \left(\frac{\partial v_i}{\partial x_j} + \frac{\partial v_j}{\partial x_i}\right) \Delta\Omega \tag{10}$$

Συγκριση Μοντέλων RANS-DES και Αποτελέσματα με την Εφαρμογή της EVA

Ακολουθούν αποτελέσματα για τρεις διαφορετικές περιπτώσεις, προκειμένου να ελεγχθεί η εγκυρότητα του κώδικα: ροή στον αγωγό U-bend, ροή γύρω από αεροτομή NACA0012 και τη γεωμετρία του Toyota Aygo X.

Περίπτωση A: U–Bend

Για την περίπτωση του U-bend, για την προσομοίωση RANS χρησιμοποιείται ο simpleFOAM του OpenFOAM, σε συνδυασμό με το μοντέλο τύρβης Spalart–Allmaras. Για την προσομοίωση DES, χρησιμοποιείται ο μη-μόνιμος (unsteady) επιλύτης pimpleFOAM για ασυμπίεστα ρευστά. Η προσομοίωση διήρκεσε συνολικά 4 δευτερόλεπτα, με χρονικό βήμα $\Delta t = 1 \times 10^{-4}\,\text{s}$. Το μοντέλο τύρβης που εφαρμόστηκε ήταν το DES Spalart–Allmaras. Η διαδικασία λήψης μέσων τιμών ξεκίνησε μετά τη μεταβατική φάση προσαρμογής, δηλαδή από $t = 2\,\text{s}$ έως το τέλος της προσομοίωσης.

Η διαδικασία ελαχιστοποίησης για την εύρεση του υποκατάστατου μοντέλου πραγματοποιήθηκε σε 20 επαναλήψεις, και τα τελικά αποτελέσματα των πεδίων ταχυτήτων εμφανίζονται στο Σχήμα 3. Η διαδικασία βελτιστοποίησης οδήγησε σε μείωση της αντικειμενικής συνάρτησης κατά 40%, με εμφανείς βελτιώσεις σε σχέση με το τι θα υπολόγιζε η αριθμητική επίλυση των χρονικά μη μόνιμων εξισώσεων RANS με μοντέλο τύρβης των Spalart–Allmaras.

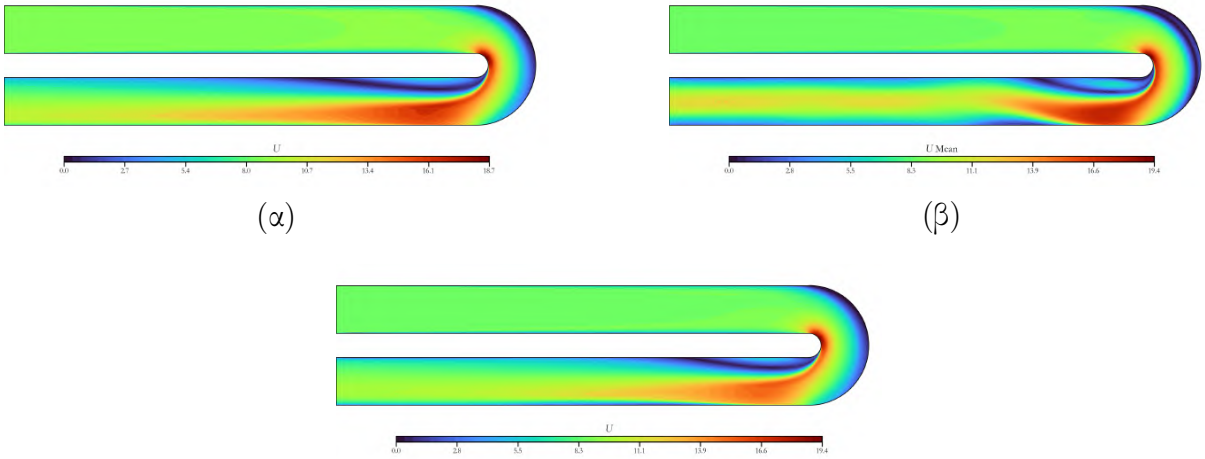

(α) (β)

(γ)

Σχήμα 3: Περίπτωση Α: Πεδίο μέτρου ταχύτητων για (α) RANS, (β) Χρονικά μέσο DES, και (γ) υποκατάστατο μοντέλο με την τεχνική EVA.

Αρχικά αξίζει να παρατηρηθεί πως το υπολογιστικό κόστος του DES είναι μεγαλύτερο από το αντίστοιχο του RANS. Τα αποτελέσματα για την περίπτωση του U-bend αναδεικνύουν ουσιαστικές διαφορές μεταξύ DES (SA) και RANS (SA). Η πιο χαρακτηριστική διαφοροποίηση στη γεωμετρία του U-bend εντοπίζεται στην αποκόλληση στην εσωτερική καμπή και στη δημιουργία φυσαλίδας ανακυκλοφορίας. Συγκεκριμένα, το μοντέλο RANS προβλέπει μια μεγαλύτερη φυσαλίδα αποκόλλησης (σε ένταση και μήκος). Επιπλέον, το μοντέλο RANS αδυνατεί να αναπαράγει επαρκώς μια δευτερεύουσα περιοχή ανακυκλοφορίας κοντά στο κάτω τοίχωμα του U-bend, η οποία αναδεικνύεται στο DES. Μετά τη διαδικασία ελαχιστοποίησης, στο υποκατάστατο μονέλο ροής η συγκεκριμένη ζώνη συρρικνώνεται και η κατανομή της ταχύτητας γίνεται μορφολογικά πιο κοντά στο v_{mean} (DES). Παράλληλα, παρατηρείται ανάπτυξη της δευτερεύουσας περιοχής ανακυκλοφορίας στο κάτω τοίχωμα του αγωγού,σε αντίθεση με τη λύση RANS (SA).

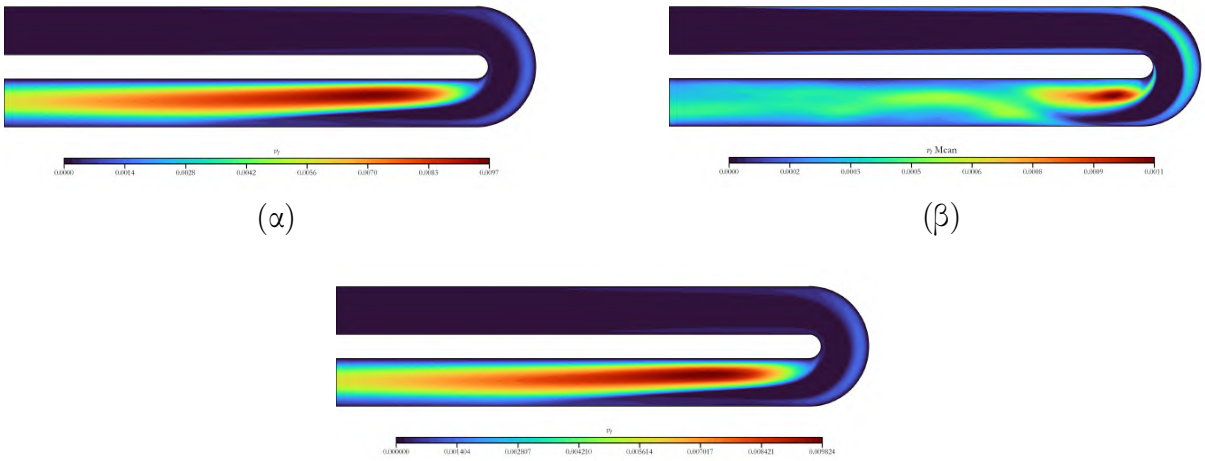

(α) (β)

(γ)

Σχήμα 4: Περίπτωση Α:Πεδίο ν_t για (α) RANS (SA), (β) Χρονικά μέσο DES (SA), και (γ) υποκατάστατο/προσαρμοσμένο μοντέλο ροής με την τεχνική EVA.

Τα πεδία (ν_t) στο DES και το RANS διαφέρουν σημαντικά, τόσο στη μορφή του πεδίου όσο και στις τιμές τους, καθώς οι κλίμακες και οι τάξεις μεγέθους τους είναι διαφορετικές. Το υποκατάστατο/προσαρμοσμένο μοντέλο ροής που προκύπτει από τη ελαχιστοποίηση παρουσιάζει μεγάλη ομοιότητα με τη μορφή του RANS, αντιστοιχεί σε πεδίο τυρβώδους συνεκτικότητας το οποίο οι τιμές του έχουν τροποποιηθεί κατάλληλα για να μειωθεί η αντικειμενική συνάρτηση, ενώ η μορφή του παραμένει φυσική.

Περίπτωση B: NACA0012

Αντίστοιχα, στην περίπτωση της αεροτομής NACA0012, τα τρεξίματα με RANS (SA) και DES (SA) πραγματοποιήθηκαν με τον ίδιο τρόπο. Για τη διαδικασία της ελαχιστοποίησης, χρησιμοποιήθηκαν 20 κύκλοι, με αποτέλεσμα τη μείωση της αντικειμενικής συνάρτησης κατά 30%. Η προσομοίωση εκτελέστηκε για γωνία προσβολής $\alpha = 12°$.

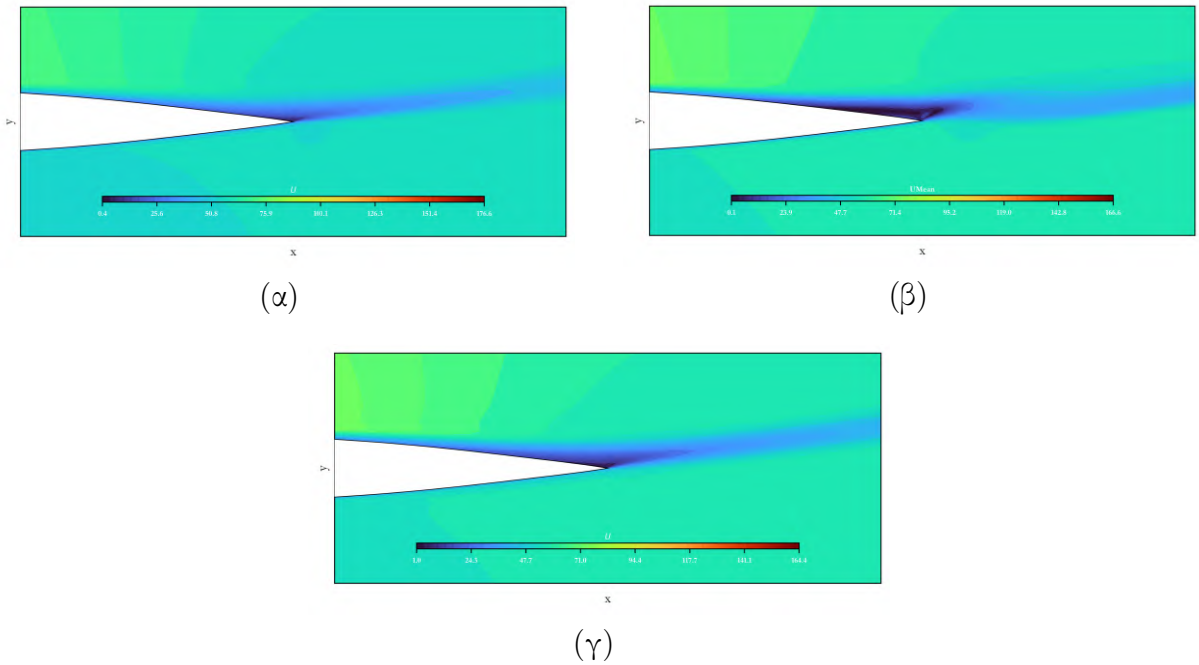

(α) (β)

(γ)

Σχήμα 5: Περίπτωση B: Πεδίο μέτρου ταχύτητων για (α) RANS (SA), (β) Χρονικά μέσο DES (SA), και (γ) υποκατάστατο/προσαρμοσμένο μοντέλο ροής με την τεχνική EVA.

Από τα αποτελέσματα προκύπτει ότι, για $\alpha = 12°$, η αποκόλληση είναι σαφέστερα ενισχυμένη στην ακμή εκφυγής στο DES. Μία από τις βασικές αλλαγές που παρατηρούνται μετά την επίλυση του προβλήματος EVA είναι ότι η ροή αναπαράγει πλέον τη ζώνη ανακυκλοφορίας-αποκόλλησης, η οποία αποτελούσε την κύρια απόκλιση μεταξύ RANS και DES. Η μεταβολή στην έκταση και ένταση της αποκόλλησης επηρεάζει τους αεροδυναμικούς συντελεστές, όπως οι C_L και C_D. Αν και το C_L βελτιώνεται, λαμβάνοντας πολύ καλύτερη τιμή σε σχέση με την αρχική, το C_D δεν βελτιώνεται και εμφανίζει ακόμη και χειρότερη τιμή. Αυτή η συμπεριφορά δεν είναι αντιφατική, καθώς η αντικειμενική συνάρτηση του προβλήματος EVA έχει οριστεί ώστε να μειώνει το μέτρο διαφοράς ταχυτήτων, και συνεπώς δεν εγγυάται ότι όλες οι ολοκληρωματικές ποσότητες (δυνάμεις/συντελεστές) βελτιώνονται επίσης. Εάν επιδιώκεται ταυτόχρονη ευθυγράμμιση πολλών μεγεθών (π.χ. ταχύτητα, πίεση, C_L, C_D),

τότε απαιτείται πολυκριτηριακή ελαχιστοποίση.

	C_L	C_D
RANS	1.21932	2.2395×10^{-2}
DES	1.12985	2.4018×10^{-2}
EVA Model	1.16049	2.7967×10^{-2}

Πίνακας 1: Περίπτωση B: Σύγκριση των RANS (SA), DES (SA) και του υποκατάστατο/προσαρμοσμένο μοντέλο ροής μοντέλου με την τεχνική EVA ως προς τους συντελεστές C_L και C_D.

Οι παραπάνω διαφορές αποτυπώνονται καθαρά και στα διαγράμματα του συντελεστή πίεσης C_p. Πλέον, η καμπύλη του διορθωμένου πεδίου τείνει να προσεγγίσει τη DES σε όλο το μήκος της, υποδηλώνοντας βελτιωμένη κατανομή πίεσης και, συνεπώς, πιο συνεπή αναπαράσταση της ροής.

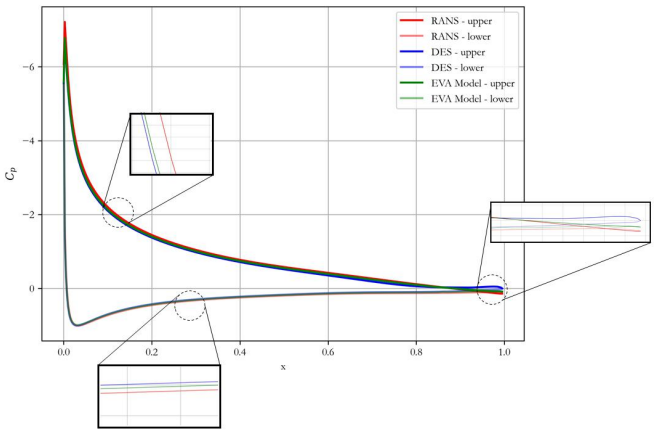

Σχήμα 6: Περίπτωση B: Σύγκριση των κατανομών του συντελεστή πίεσης (C_p) για την αεροτομή NACA0012 που προέκυψαν από τα μοντέλα DES (SA), RANS (SA) και το υποκατάστατο/προσαρμοσμένο μοντέλο ροής με την τεχνική EVA.

Περίπτωση C: Toyota AYGO X

Για το μοντέλο αυτοκινήτου Toyota AYGO X στην προσομοίωση RANS, χρησιμοποιήθηκε ο simpleFOAM του OpenFOAM, σε συνδυασμό με το μοντέλο τύρβης Spalart–Allmaras, για 7.000 επαναλήψεις. Για την προσομοίωση DES, χρησιμοποιήθηκε το αποτέλεσμα της προσομοίωσης RANS ως αρχικοποίηση και στη συνέχεια εφαρμόστηκε, μη-μόνιμος επιλυτής pimpleFOAM. Η προσομοίωση διήρκεσε συνολικά 5 δευτερόλεπτα, με χρονικό βήμα $\Delta t = 1.4 \times 10^{-4}\,\mathrm{s}$. Η διαδικασία λήψης μέσων χρονικά τιμών ξεκίνησε μετά τη μεταβατική φάση προσαρμογής, δηλαδή από $t = 2\,\mathrm{s}$ και συνεχίστηκε έως το τέλος της προσομοίωσης. Για τη διαδικασία ελαχιστοποίησης, εκτελούνται 3 επαναλήψεις. Στην περίπτωση αυτή η πρόβλεψη του RANS (SA) αποτυγχάνει να πετύχει την ακρίβεια που θέτει ο κανονισμός WLTP και προβλέπει εντελώς διαφορετικά πεδία, σε αντίθεση με το DES (SA), το οποίο περνά τα απαιτούμενα τεστ.

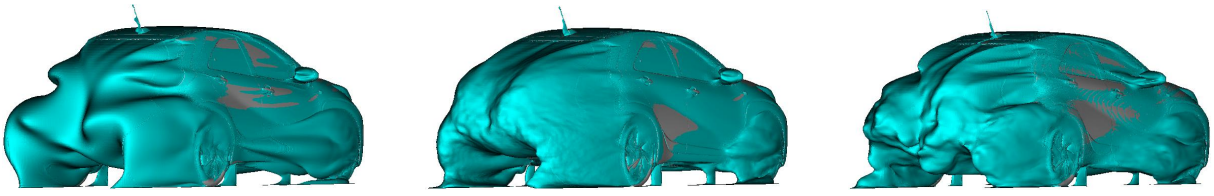

(α) (β) (γ)

Σχήμα 7: Περίπτωση C: Κατανομή του C_{pt} που εμφανίζεται από διαφορετικές γωνίες θέασης: (α) RANS (SA), (β) DES (SA), και (γ) υποκατάστατο/προσαρμοσμένο μοντέλο ροής με την τεχνική EVA.

Αυτό γίνεται εμφανές από τα διαγράμματα του συντελεστή ολικής πίεσης C_{pt}, ξεκινώντας από την περιοχή των εμπρόσθιων τροχών και προχωρώντας προς το πίσω μέρος του οχήματος. Οι διαφορές μεταξύ RANS και DES είναι σαφείς ως προς το σχήμα και το μέγεθος της ζώνης ανακυκλοφορίας. Κοντά στους εμπρόσθιους τροχούς, το RANS προβλέπει μεγαλύτερη περιοχή ανακυκλοφορίας σε σχέση με το DES, ενώ το DES εμφανίζει μικρότερης κλίμακας δομές με πιο τοπική κατανομή ανακυκλοφορίας. Η μεγαλύτερη διαφορά εντοπίζεται κοντά στα πίσω φώτα, όπου το RANS προβλέπει τη ροή να παραμένει προσκολλημένη στο πίσω μέρος του αμαξώματος, ενώ στο DES η ροή αποκολλάται νωρίτερα, δημιουργώντας διαφορετική ζώνη ανακυκλοφορίας και διαφορετική κατανομή απωλειών πίεσης.

Με τη διαδικασία ελαχιστοποίησης, παρατηρείται σημαντική βελτίωση στη ροή, καθώς τα υπολογιζόμενα πεδία προσεγγίζουν περισσότερο τη φυσική συμπεριφορά της ροής, όπως την προβλέπει το DES. Η αναπαράσταση της αποκόλλησης και ανακυκλοφορίας είναι πιο ρεαλιστική και η κατανομή πίεσης και ταχυτήτων είναι ακριβέστερη, υποδεικνύοντας ότι η ελαχιστοποίηση προσέφερε μια πιο ρεαλιστική αναπαράσταση σε σχέση με το αρχικό μοντέλο RANS.

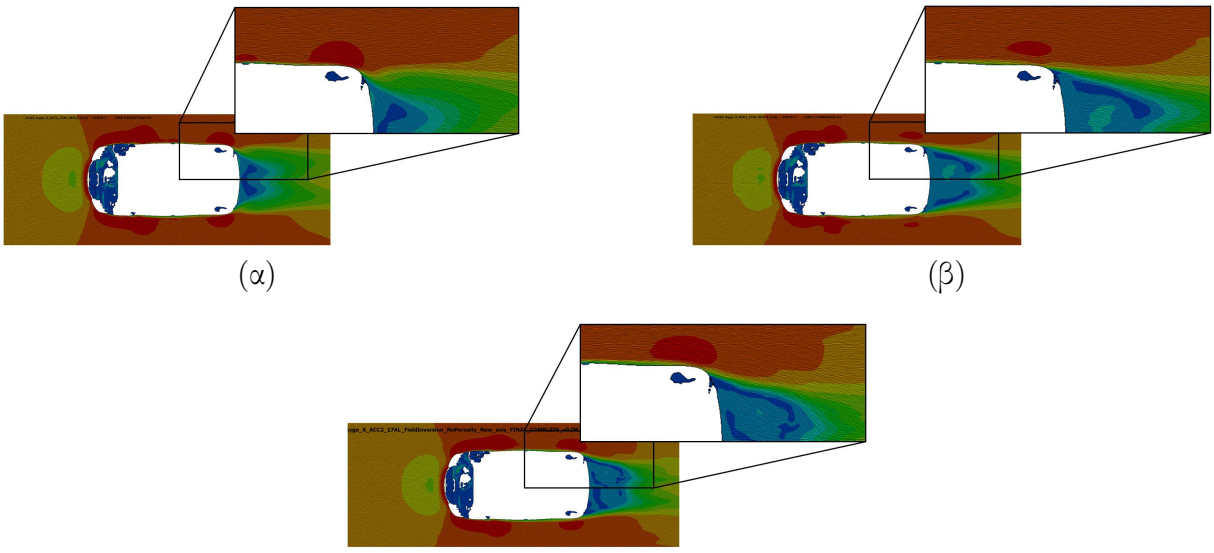

(α) (β)

(γ)

Σχήμα 8: Περίπτωση C: Πεδίο ταχυτήτων για (α) RANS (SA), (β) χρονικά μέσο DES (SA), και (γ) υποκατάστατο/προσαρμοσμένο μοντέλο ροής με την τεχνική EVA.

Οι παραπάνω διαφορές και βελτιώσεις γίνονται εμφανείς και στα αντίστοιχα πεδία ταχυτήτων στο επίπεδο XY, όπου παρατηρείται διαφορά μεταξύ προσκολλημένης και αποκολλημένης ροής. Το πεδίο από την διαδικασία EVA παρουσιάζει αποκόλληση, ενώ προβλέπει επίσης το κέντρο του στροβιλισμού της ανακυκλοφορίας με τρόπο πολύ παρόμοιο με το DES.

Βελτιστοποίηση Μορφής με τα Διορθωμένα Πεδία και FEV

Η βελτιστοποίηση μορφής με βάση το DES είναι υπολογιστικά ιδιαίτερα δαπανηρή. Ειδικότερα, η φύση των μη-μόνιμων συζυγών εξισώσεων προσθέτει επιπλέον δυσκολίες, καθώς απαιτεί αποθήκευση ή επαναϋπολογισμό δεδομένων, κάτι που αυξάνει το υπολογιστικό κόστος. Επιπλέον, η υβριδική φύση του DES (RANS-LES) εισάγει μη-ομαλές εξαρτήσεις από το πλέγμα, δυσκολεύοντας τη διαδικασία βελτιστοποίησης. Μια ενδιάμεση λύση είναι η τεχνική της "παγωμένης τύρβης" η οποία υποθέτει ότι το πεδίο τύρβης (ν_t) παραμένει αμετάβλητο όταν οι γεωμετρικές παραμορφώσεις είναι αρκετά μικρές, επιτρέποντας την υπολογιστική βελτιστοποίηση με χαμηλότερο κόστος. Συνδυάζοντας αυτή την τεχνική με τη διαδικασία εύρεσης υποκατάστων (EVA) πεδίων τύρβης που περιγράφηκε προηγουμένως, προκύπτουν αποτελέσματα κοντά σε αυτά του DES, χωρίς τις υψηλές υπολογιστικές απαιτήσεις του πλήρους DES. Ωστόσο, η παραδοχή της "παγωμένης τυρβώδους συνεκτικότητας" (Frozen Eddy Turbulence ή FEV), λόγω του περιορισμού της, απαιτεί προσεκτική αξιολόγηση για να θεωρηθεί κάποια λύση αξιόπιστη. Για την ολοκληρωμένη βελτιστοποίηση μέσω πολλών κύκλων, θεωρητικά θα έπρεπε να γίνεται υπολογισμός διόρθωσης των πεδίων τύρβης με την ίδια διαδικασία που περιγράφηκε.

Στη μελέτη αυτή, ολοκληρώθηκε μια διαδικασία βελτιστοποίησης μορφής, με στόχο τη μείωση του οπισθέλκουσας. Δοκιμάστηκαν τόσο η βελτιστοποίηση με βάση το μοντέλο RANS, όσο και η βελτιστοποίηση μέσω της διαδικασίας FEV. Μετά τη διαδικασία βελτιστοποίησης, εκτελέστηκε μια προσομοίωση DES (SA) και συγκρίθηκαν τα αποτελέσματα για να αξιολογηθεί η μείωση των δεδομένων. Οι δύο διαδικασίες βελτιστοποίησης πραγματοποιήθηκαν σε 3 επαναλήψεις, με την παραδοχή ότι η γεωμετρία δεν θα παραμορφωθεί αρκετά ώστε να αναιρεθεί η υπόθεση FEV.

Η προσομοίωση επαλήθευσης DES (SA) διήρκεσε συνολικά 4 δευτερόλεπτα, με χρονικό βήμα $\Delta t = 1 \times 10^{-4}$ s. Η διαδικασία λήψης μέσων τιμών ξεκίνησε μετά τη μεταβατική φάση από $t = 2$ s έως το τέλος της προσομοίωσης.

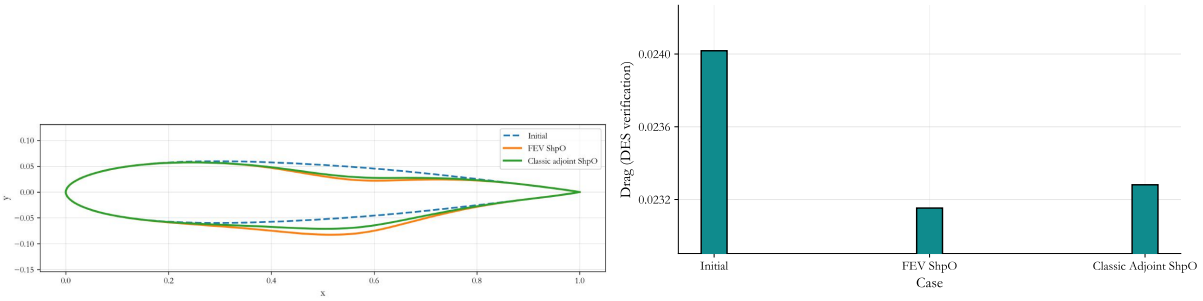

(α) (β)

Σχήμα 9: Περίπτωση B (ShpO) (α) Σχήμα της βασικής αεροτομής και των βελτιστοποιημένων γεωμετριών που προέκυψαν μέσω της βελτιστοποίησης μορφής με βάση τη συνεχή συζυγή μέθοδο και την υπόθεση FEV (β) Επιβεβαίωση της μείωσης του συντελεστή οπισθέλκουσας για τις βελτιστοποιημένες γεωμετρίες μέσω DES.

Η βελτιστοποίηση με FEV παρουσίασε μείωση της οπισθέλκουσας κατά -3.60%, ενώ η κλασική βελτιστοποίηση μορφής είχε μείωση -3.07%. Παρά τη μικρή διαφορά, η υπεροχή του DES υποδεικνύει ότι η μέθοδος αυτή οδηγεί σε βελτιωμένες γεωμετρίες, κάτι που σε άλλες περιπτώσεις μπορεί να αποτελεί μονόδρομο, ειδικά όταν το RANS αποτυγχάνει να προσεγγίσει με ακρίβεια τη ροή που αναπτύσσεται. Η προσέγγιση είναι υπολογιστικά πιο αποδοτική και κατάλληλη για σενάρια όπου τα πεδία RANS και DES είναι ήδη διαθέσιμα. Τα αποτελέσματα δείχνουν ότι η μέθοδος αυτή είναι υποσχόμενη για μελλοντική εφαρμογή και ανάπτυξη.

Συμπεράσματα και Προτάσεις για Μελλοντική Έρευνα

Η μέθοδος υποκατάσταση (EVA) μοντέλου τύρβης αποδείχθηκε ιδιαίτερα υποσχόμενη, βελτιώνοντας σημαντικά τα πεδία σε όλες τις περιπτώσεις που μελετήθηκαν. Μπορεί να χρησιμοποιηθεί ως ένα πολύτιμο υπολογιστικό εργαλείο για τη δημιουργία δεδομένων που θα αξιοποιηθούν ακόμα και στην ανάπτυξη νέων μοντέλων τύρβης (που ήταν εκτός των στόχων αύτης της εργασίας). Παρόλα αυτά, υπάρχει περιθώριο για περαιτέρω βελτίωση, ώστε ο συντελεστής ν_t να έχει ακόμη καλύτερη επίδραση ταυτόχρονα και σε άλλες παραμέτρους της ροής. Για να επιτευχθεί αυτό, η μέθοδος πρέπει να μελετηθεί ως πρόβλημα πολυκριτηριακής ελαχιστοποίησης, όπως η μείωση του συντελεστή C_D ή η ελαχιστοποίηση των απωλειών πίεσης. Περαιτέρω, αξιοποιώντας τα δεδομένα αυτής της τεχνικής και συνδυάζοντας τεχνικές όπως τα νευρωνικά δίκτυα και η Deep Symbolic Regression (DSR), μπορεί να δημιουργηθούν μοντέλα με υπολογιστικό κόστος αντίστοιχο του RANS, ενώ η ακρίβεια μπορεί να βελτιωθεί ανάλογα με τους στόχους που τίθενται. Η τεχνική αυτή είναι ιδιαίτερα χρήσιμη αν διατίθενται πειραματικά δεδομένα και υψηλής πιστότητας προσομοιώσεις, προσφέροντας σημαντικά οφέλη με τη σημαντική εξοικονόμηση κόστους και χρόνου.